Master Thesis

Setup and commission of a magnetic field test stand and studies on the influence of magnetic fields on the perfomance of the Hamamatsu R12199-02

Supervisor:
Prof. Dr. Alexander Kappes

Second examiner:
Dr. Volker Hannen

A thesis submitted in fulfilment of the requirements for the degree of

Master of Science *at* Westfälische Wilhelms-Universität Münster

by

Ken Lukas Ueberholz

Arbeitsgruppe Prof. Dr. Kappes.
Institut für Kernphysik

Münster, February 2020

Declaration of Academic Integrity

I hereby confirm that this thesis on "Setup and commission of a magnetic field test stand and studies on the influence of magnetic fields on the perfomance of the Hamamatsu R12199-02" is solely my own work and that I have used no sources or aids other than the ones stated. All passages in my thesis, for which other sources, including electronic media, have been used, be it direct quotes or content references, have been acknowledged as such and the sources cited.

Münster, 17. February 2020 _____

I agree to have my thesis checked in order to rule out potential similarities with other works and to have my thesis stored in a database for this purpose.

Münster, 17. February 2020 _____

Contents

1 Introduction

Astronomy is one of the oldest natural sciences with the first examples dating back thousands of years. With the invention of the telescope in the 17th century, a leap towards better understanding of the cosmos was possible, leading to more and more ambitious projects. The historic balloon flight of Victor Hess on the 7^{th} August 1912 was the awakening of a new era of astronomy, by not looking at optical light but information carried by other particles.

Cosmic rays of energies impossible to produce with current human technologies, reach the Earth without ever being noticed. Energies of up to $10^{20}\,\text{eV}$ were detected, far exceeding energies produced in the most ambitious experiments like CERN. Where their origins lie and how they could ever reach such tremendous energies is mostly unknown. Until now, it has been the topic of speculations and models ranging from supernovae to black holes. The reason and main aggravation for this lies in the nature of the cosmic rays themselves. Having a high interaction cross section results in the interception of most of them before reaching Earth. Those who manage to avoid all obstacles on their flight get deflected by the countless magnetic fields of space, leaving no information about their roots behind. Beside cosmic rays photons and neutrinos are subsequently created reaching similar energies. High energetic photons, being uncharged, point towards their source but interact easily with matter or the background radiation on their way to earth. To be able to get information about the origin of those particles something chargeless with a small interaction cross section is needed.

Neutrinos, first postulated on 4^{th} of December 1930 by Wolfgang Pauli, are chargeless, nearly non interactive particles, making them ideal candidates to point directly at their source while containing their original energy. The standard model of particle physics first theorised them to be massless, which was disproved by the observed neutrino oscillation, breaking the lepton flavour conversation.

With the discovery of neutrinos, a whole new range of experiments were brought to life, which had to follow entirely new concepts and overcome so far unknown obstacles. The biggest advantages of neutrinos are also their greatest weakness, the small cross section of the neutrinos leaves only a fraction to interact with the Earth at all. Therefore, to have a realistic chance of using neutrinos for astronomy, the detector volume has to be sufficiently large. When one of the neutrinos finally interacts with the nucleon of an atom, a range of charged particles is produced, which can be observed by their radiated Cherenkov light if emitted in a transparent volume. Only a few places on Earth satisfy the requirements, to be big enough to house the detector, transparent for light and, if possible, be shielded against particles other than neutrinos. One of them is the ice plate of the South Pole, home of the IceCube neutrino observatory.

IceCube mainly consists of one cubic kilometre of ice, 1450 m beneath the surface in complete darkness. In this giant ice cube, 5160 Digital Optical Modules, short DOMs, are aligned on long strings. Each module contains a Photo Multiplier Tube, short PMT, secured in a pressure vessel, able to detect even single photons of the Cherenkov radiation left from the charged particles of neutrino interactions. While IceCube is currently the largest of various neutrino telescopes, it was neither the first nor will it be the last.

Currently in planing is IceCube Upgrade and later the next generation: IceCube *Gen2*, increasing the covered volume by a factor of 10 and by this also the frequency of detected and successfully reconstructed events. IceCube Upgrade will decrease the distance of the modules and the energy threshold. Additionally, it introduces a new set of detector modules to be tested for *Gen2*, with one of them being the multi Digital Optical Module, short mDOM. The mDOM, currently under development in the University of Münster and other cities, will use 24 smaller PMTs arranged spherically in the pressure vessel to achieve a homogeneous 4π coverage.

PMTs use the photoelectric effect to convert single photons to electrons, which get multiplied over a dynode system to create an electric signal. All charged moving particles, like electrons, get deflected according to the Lorentz force if a magnetic field is present. The signal generated by the PMTs is therefore dependent on the form and strength of the surrounding magnetic field. Luckily for us humans, the Earth molten iron core generates a magnetic field, shielding us from the solar winds. Less luckily for the people evaluating the signals of PMTs, the magnetic field has a strength ranging from 20 to 60 μT, enough to deflect the path of the electrons and to contaminate the measurements of large PMTs like the on in the DOM, which therefore had to be shielded against magnetic fields. What dimension this effect has on the smaller PMTs of the mDOM has already been analysed and it was determined that further, more complex investigations are necessary.

This thesis covers the set up and commission of a 3-dimensional Helmholtz coil cube as well as the first measurements of the influence of the magnetic field at the South Pole on the PMTs of the mDOM. In chapter 1, a detailed description of the underlying theory is given. Chapter 2 is concerned with the planing, analytically simulation and construction of the coil cube. Subsequently the characterisation of the magnetic field in the laboratory and of the setup are covered. In chapter 3, first measurements are discussed to show the reproducibility of previous investigations and to evaluate the output signal of the PMT, regarding a field of arbitrary orientation and a strength similar to the field at IceCube. Finally, a summary and an outlook on further research are given.

2 Theory

In the following chapter the theoretical foundation for this thesis is covered, beginning with the basic questions: What are neutrinos? How can they be observed and used for astronomy? In which way does the magnetic field of the Earth influence these observations?

2.1 Neutrino astronomy

Neutrinos are one part of the multiplicity of particles bombarding the Earth. How they are different to the other particles and how those special properties can be used for new astronomy will be explained in this section.

2.1.1 Cosmic rays

The Earth's atmosphere is a target of a continuous flux of cosmic rays with a broad range of energies, from a few MeV to as much as 10^{20} eV. Around 1000 particles per square meter per second enter the Earths atmosphere with energies of GeV, decreasing to less than 1 per year per square meter for PeV and going down to less than 1 per square kilometre per century at highest energies. 90 % of cosmic rays are protons, 9 % alpha particles and 1 % heavy nuclei. How those particles are accelerated to those enormous energies, is a current field of research with a number of speculations and models as well as promising cosmic accelerator candidates. Sources of such high energetic particles are accordingly highly interesting [1].

Upon entering the Earth's atmosphere interactions with air particles are inevitable. When a cosmic ray interacts with a nucleon of a particle in the atmosphere, a number of secondary particles are created. These interact again, creating a cascade of particles, reaching all the way down to the surface of the Earth for energies of the primary particles larger than 10^{14} eV [2].

Those cascades are called air showers and a number of observatories, for example the Pierre Auger Observatory [3], around the globe are constantly observing the sky for high energy particles and their sources. Cosmic rays most often interact before reaching earth but when an air shower of a cosmic ray is detected, it is almost impossible to reconstruct its source. Cosmic rays are likely to have been redirected by the numerous cosmic magnetic fields and the strong magnetic fields during their acceleration. This makes it necessary to look at the neutral particles created in such cosmic accelerators.

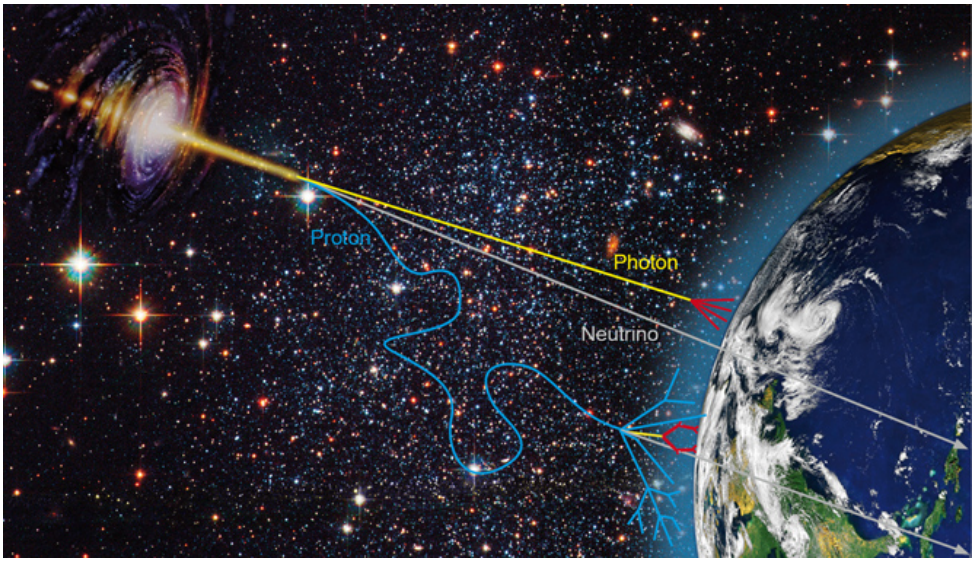

Figure 2.1: Illustration of the paths different particles and cosmic rays travel before reaching the Earth [4].

Beside cosmic rays, high energetic γ-rays from cosmic accelerators have the chance to reach the Earth. In contrast and as great advantage to the cosmic rays, γ-rays are chargeless and point directly to their source, as shown in figure 2.1. One problem is that γ-rays can still easily interact with matter on their way to Earth and might never reach a detector. Additionally, photons can interact with other photons of the background radiation via pair production limiting their mean free path length [5].

When interacting with the atmosphere, the γ-rays behave very similarly to cosmic rays and create a cascade of secondary particles.

Intergalactic sources of cosmic rays are also sources of high energetic neutrinos, giving a third chance for the observation and investigation of cosmic accelerators.

2.1.2 Neutrinos, sources and properties

Neutrinos are part of the elementary particles of our universe and belong to the lepton family of the Standard Model of particle physics illustrated in figure 2.2. They are uncharged and mostly interact through the weak force. Three kinds of neutrino flavours exist: electron, muon, and tau neutrinos corresponding to the three charged leptons.

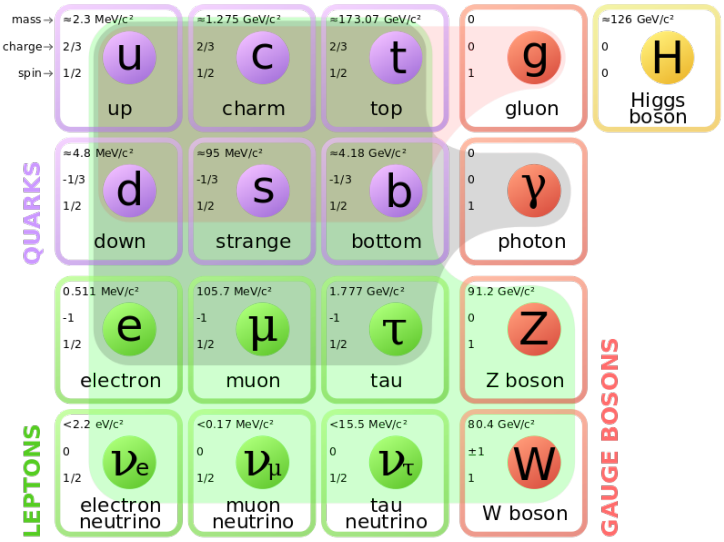

Figure 2.2: Particles and force quanta of the Standard Model divided into fermions and bosons. The former are further divided into leptons and quarks and the latter are divided into gauge and scalar bosons [6].

The lepton flavour of neutrinos is not conserved. It was experimentally proven that the flavour can change through an oscillation mechanism, which can only be explained by neutrinos have a mass (different for the 3 flavours), contrary to what was previously assumed [8].
On the one hand, due to neutrinos being chargeless and nearly none interactive, their direct detection is impossible. Instead, secondary charged particles, after an interaction, are necessary for detection and a reconstruction has to be done. On the other hand, these properties grant the neutrino a comparable long free mean path through any matter, making them ideal candidates to reach all the way from cosmic accelerators to Earth in a straight line without interaction. The minimal cross section then becomes the problem. Conventional detectors were to small and new kinds of detectors of huge volumes were necessary to increase the detection probability of high energetic neutrinos.

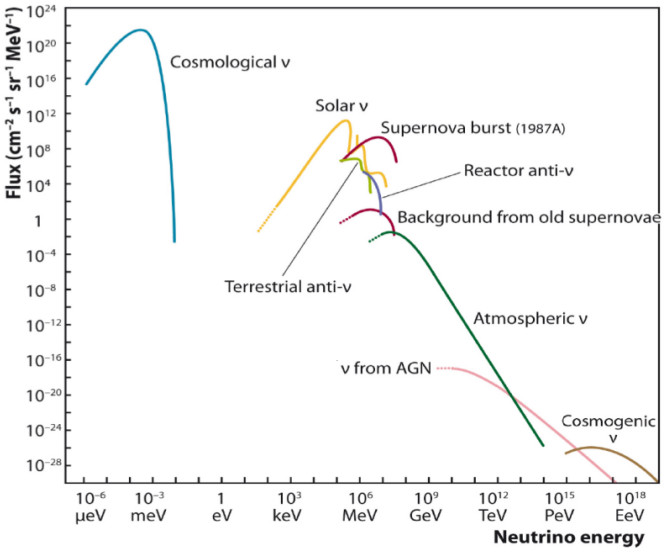

Figure 2.3: Flux of neutrinos regarding their energies, with corresponding sources [7].

Besides the high energetic, comparably rare cosmic neutrinos, there are numerous other neutrinos from different sources like radioactive decays, the sun, supernovae or even air showers, as shown in figure 2.3. To illustrate the magnitude of the neutrino flux, one can imagine billions of billions of neutrinos flying through every single human during each heartbeat.

2.1.3 Neutrino detection

Neutrinos above 10 GeV interact mostly through deep inelastic scattering with nucleons. These interactions are either carried out via a neutral current (NC) of a Z^0-Boson, creating a cascade of hadrons or through a charged current (CC) of a $W^{\pm}$-Boson. In the second case a lepton with the associated flavour of the neutrino is created along with a hadron shower, see eq. 2.1 and figure 2.4.

$$\overset{(-)}{\nu}_l + N \rightarrow \overset{(-)}{\nu}'_l + X \;\; (NC) \qquad \text{or} \qquad \overset{(-)}{\nu}_l + N \rightarrow l^{\pm} + X \;\; (CC), \tag{2.1}$$

where $l \in \{e, \mu, \tau\}$ regarding the lepton flavour, N is a proton or neutron and X is a cascade of hadronic particles [9]. In both cases, NC and CC interaction, charged particles are produced, which can be observed via Cherenkov light.

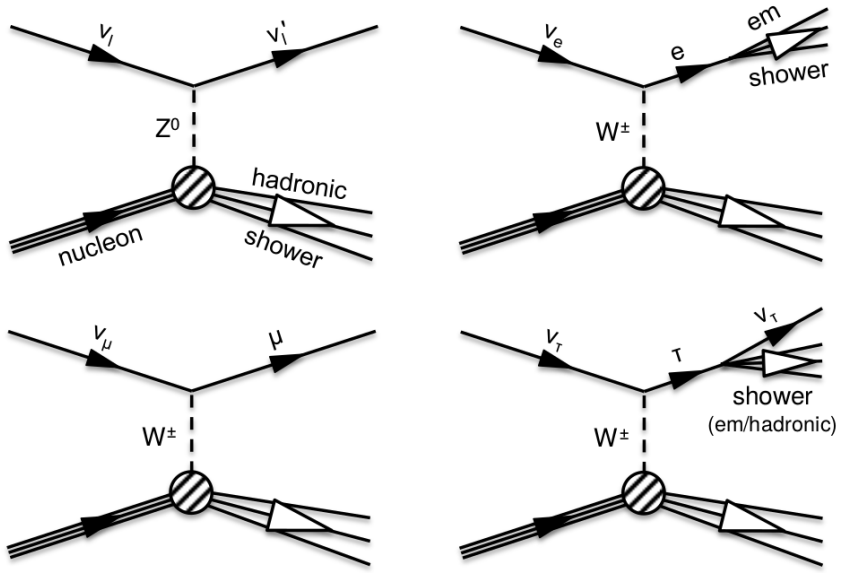

Figure 2.4: Deep inelastic scattering of a neutrino on a nucleon at GeV energies illustrated by Feynman-diagrams. **Top left:** Neutral current exchange via a Z^0-Boson. Others: Charged current of different neutrinos. **Top right:** Production of an electron and a resulting electromagnetic shower. **Bottom left:** Production of a muon. **Bottom right:** Production of an ephemeral tau and its subsequent decay [10].

Cherenkov light

While charged particles travel through a dielectric medium, they influence the electric field of the surrounding atoms. The atoms become temporal dipoles, sending out electromagnetic pulses when falling back to their original state. In most cases, these pulses interfere destructively with each other, preventing any emission of electromagnetic signals. This behaviour changes as soon as the particle moves faster than the speed of light in the medium

$$v > c = \frac{c_0}{n}, \tag{2.2}$$

where c_0 is the speed of light in vacuum, c the speed of light in the medium, v the speed of the particle and n the refraction index.

This can be written in terms of the necessary kinetic energy of the particle

$$E_{\text{kin}} > m_0 c^2 \left(\sqrt{\frac{n^2}{n^2 - 1}} - 1 \right), \tag{2.3}$$

with m_0 as the mass of the particle.

If the kinetic energy is high enough, the particle starts polarising new atoms before the previous ones shift back into their original state. The emitted electromagnetic pulses no longer interfere destructively but constructively [12], as shown in figure 2.5. The pulses form a coherent wave front similarly to a sonic boom of sound waves.
The opening angle of the wave θ is determined by

$$cos(\theta) = \frac{1}{\beta \cdot n} \tag{2.4}$$

and is approximately 40° in ice with $n_{\text{ice}} = 1.3$ and $\beta = \frac{v}{c} \approx 1$.

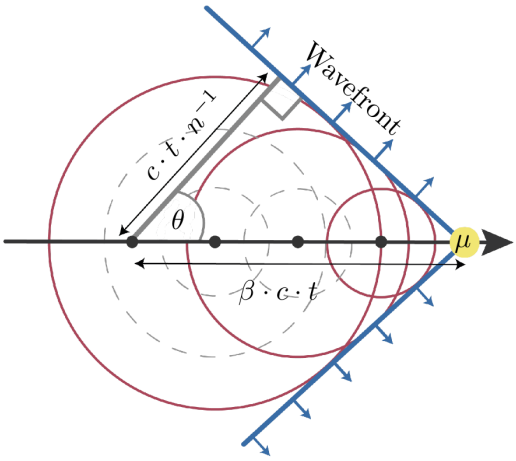

Figure 2.5: Illustration of the production of Cherenkov radiation. In this case a muon moving with the speed $\beta \cdot c$ produces a wavefront under the angle θ [11].

Using this cone of light, the original particle trajectory and source can be reconstructed to gather information about the neutrino.
Using the Frank-Tamm formula [13], the number of photons radiated per unit of length can be determined using

$$\frac{d^2 N_\lambda}{dx d\lambda} = \frac{2\pi\alpha}{\lambda^2} \cdot \left(1 - \frac{1}{\beta^2 n(\lambda)^2} \right), \tag{2.5}$$

where N_λ is the number of photons, $\alpha \approx \frac{1}{137}$ is the fine structure constant and λ is the wavelength of the emitted light. This number of photons provide information on the original energy of the charged particle and by this on the neutrino itself.

Neutrino signatures

Depending on the secondary particles created in a neutrino interaction, the resulting detector signature is different.

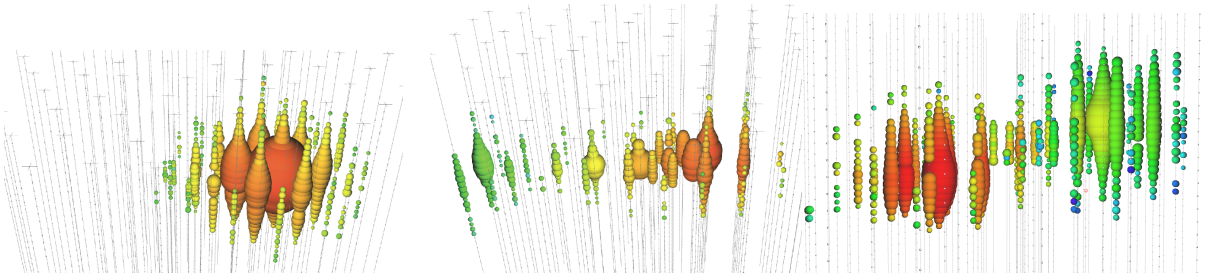

Figure 2.6: Display of light detected from neutrino interactions. **Left:** Electromagnetic or hadronic shower coming from a NC or ν_e. **Middle:** Track of a muon. **Right:** Double Bang of a tau. The size of the spheres indicates the amount of photons detected while the colour represents the arrival time of the photons from early (red) to late (green) [14].

The three cases are:

- **Showers:** Hadronic showers created by the neutrino give away all of their energy in a small sphere around the event origin. Electrons created by an ν_e do the same via Bremsstrahlung, scattering, and pair production. Showers are localised in the detector giving good information about the energy of the neutrino but barely reveal anything about the trajectory of the neutrino (see figure 2.6 left).
- **Tracks:** When a muon is created by a ν_μ and exceeds the energy threshold for Cherenkov radiation, it travels a long time releasing a constant stream of photons along its path. In its creation centre a small cluster of hadrons create further particles in a cloud around its origin. The path is easily reconstructable but might leave the detection area, making precise energy measurements complicated (see figure 2.6 middle).
- **Double-bang:** A τ created by a ν_τ travels only a short distance before decaying via the weak interaction into either an electron, muon or mesons. Those create another cascade forming another cloud of photons next to the hadronic shower of its origin creating the so called double-bang (see figure 2.6 right).

2.2 The IceCube neutrino observatory

Concluding from the behaviour of neutrinos some key elements for successful neutrino detection are necessary for a working detector:

1. A huge detection volume is needed to compensate for the low neutrino-matter interaction cross section.
2. This detector medium has to be transparent for Cherenkov light and shielded from other particles.

There are only a few places on Earth, which satisfy these requirements. One of them is the giant ice plate of Antarctica, home of the Amundsen-Scott-Station and the IceCube neutrino observatory next to the geographic South Pole.

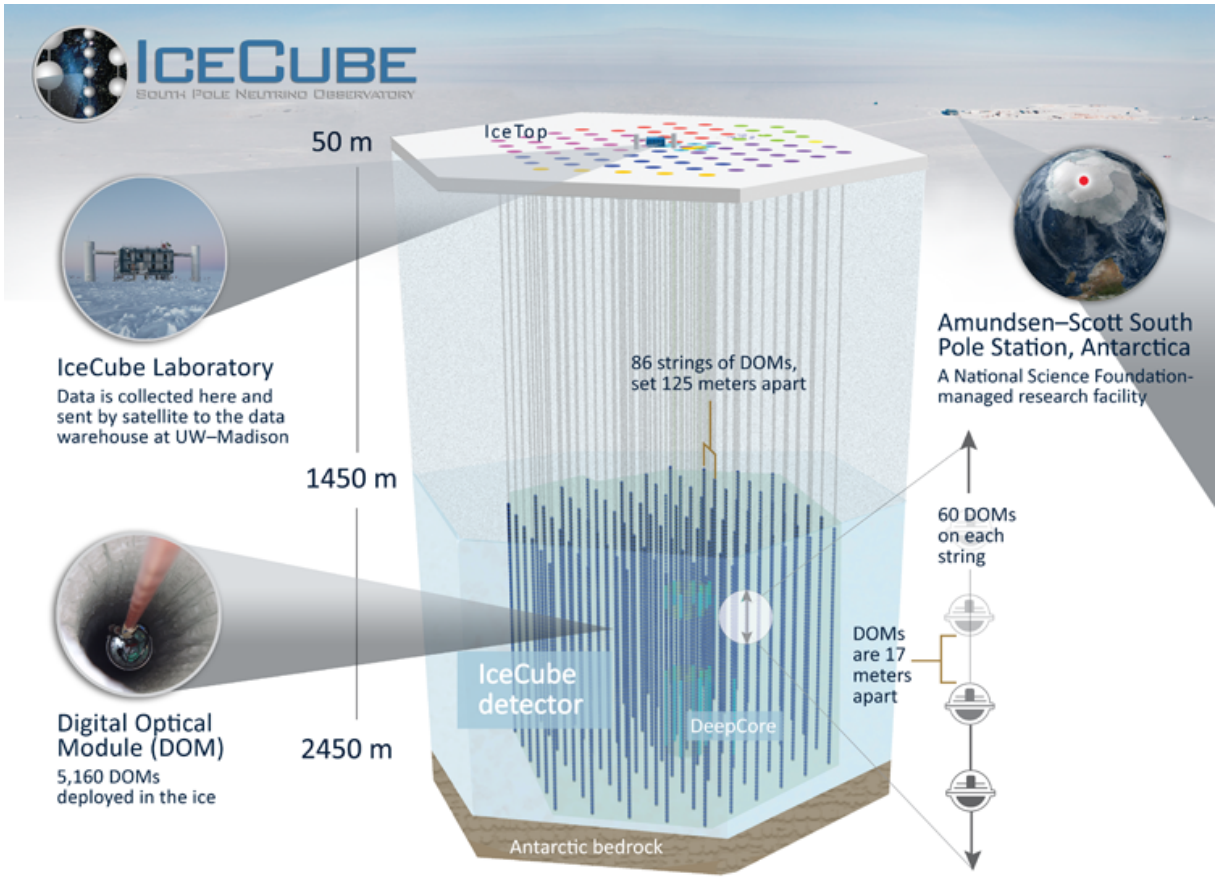

Figure 2.7: Schematic of IceCube. Courtesy of the IceCube Collaboration.

2.2.1 Detection principle

IceCube consists of one cubic kilometre of ice filled with lines of detectors deep under the surface of the ice together with some surface detectors and a laboratory. 5160 modules, called DOMs (Digital Optical Module) are vertically lined up on 86 strings with 60 detectors each. These strings are deposited in 2450 m deep, ice filled bore holes with detectors in depth of between 1450 to 2450 m, as shown in figure 2.7 The strings are organised in a hexagon grid with a distance of 125 m between each string. In the centre of the complex lies a denser detection area, the DeepCore sub detector consisting of eight strings with an average separation of 70 m. The modules along the strings have a spacing of 17 m in general and 7 m in the DeepCore [15].

IceCube has been optimised for the detection of neutrinos with energies in the TeV region and has a threshold of approximately 100 GeV. Lower energy events in the optical modules from, for example galactic neutrino sources, WIMPS or Gamma ray bursts, are rarer and the reconstruction capabilities are limited. To access these energies, the DeepCore was build, lowering the energy threshold to about 10 GeV [16].

IceCube Upgrade

To lower the energy threshold even further to 1 GeV, IceCube Upgrade is planed [17], consisting of 7 Strings inside of the DeepCore with a vertical spacing of 3 m between the modules totalling 100 modules per string, as shown in figure 2.8. Besides creating a denser detector grid, new kinds of modules will be deployed: the multi-PMT digital optical module (mDOM) and the Dual optical sensors (D-Egg), which will further increase the detection capabilities of IceCube Upgrade. Additionally, IceCube Upgrade also serves as a module testbed for the coming IceCube-Gen2, which is currently in planning. Gen2 will increase the size of the detector to about 10 km^3 with new detectors and modules increasing both, the number of events detected and the energy and trail reconstruction by increasing the probability of particles depositing their full energy before reaching the edge of the detector area[18].

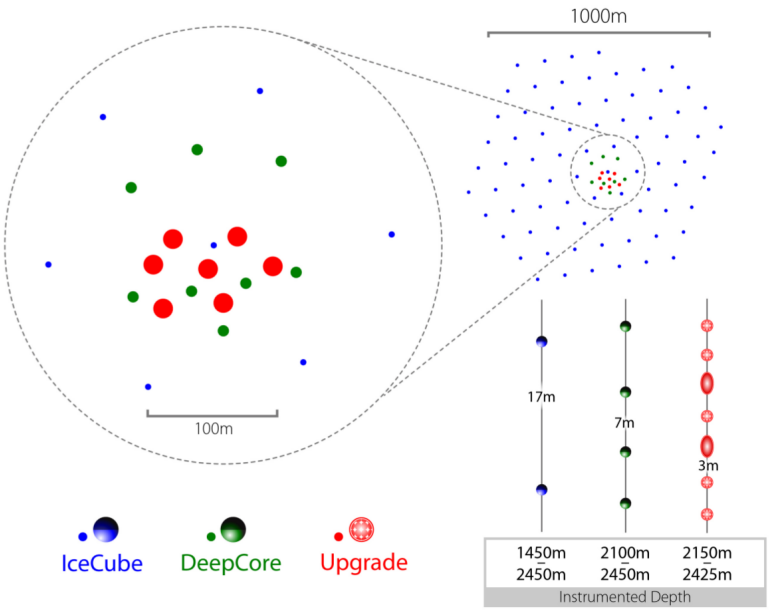

Figure 2.8: Plans for IceCube Upgrade. 7 New Strings in the area of the Deepcore with smaller spacing between modules as well as calibration devices [17].

Located on the surface of the ice are 81 surface detectors consisting of two tanks of ice with two downward facing DOMs. These detectors are used as calibration and veto devices and can detect air showers from 300 TeV to 1 EeV. The brain of IceCube is the Counting House on the surface gathering the information of all detectors.

The IceCube detector modules

The IceCube detector modules are the DOMs [15]. They are used to detect the Cherenkov photons and thus mainly consist of a large **P**hoto **M**ultiplier **T**ube (PMT) as depicted in figure 2.9. This PMT is shielded against magnetic fields and is secured with the main board and the base of the PMT inside of a pressure sphere. This pressure sphere is made out of glass to be transparent for Cherenkov photons and can withstand the enormous pressure of up to 690 bar from the surrounding ice.

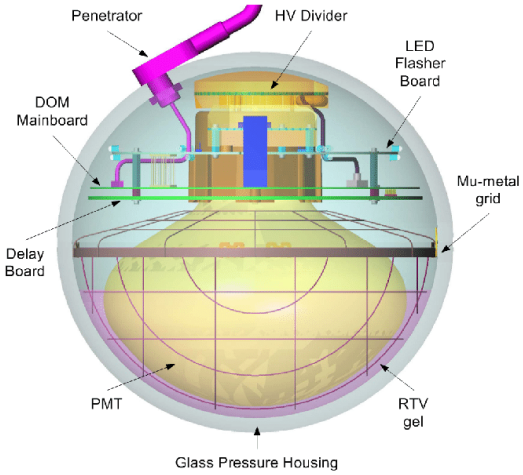

Figure 2.9: Schematics of the DOM currently used in IceCube with one large 10-inch PMT and shielding. Courtesy of the IceCube Collaboration.

The mDOM shown in figure 2.10 follows a similar yet different approach [10]. Similar to the DOM, a nearly round glass pressure vessel is used to protect the hardware. In contrast to the one big 10-inch PMT of the DOM, the mDOM uses 24 3-inch PMTs distributed nearly equally over the whole sphere. No shielding is wrapped around the PMTs but reflector rings are used to increase the effective detection area. Both DOM and mDOM use a silicon based gel between the glass vessel and the PMTs to minimise refraction.

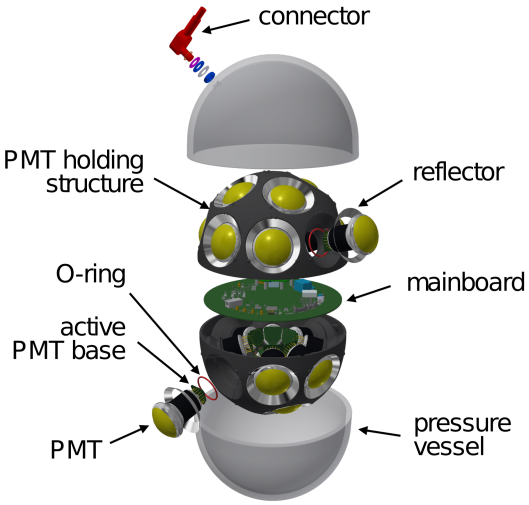

Figure 2.10: Schematic of the planned mDOM currently under testing with 24 3-inch PMTs covering all directions. Courtesy of the IceCube Collaboration.

These specifications have several advantages in comparison to the DOM:

- **Better angular acceptance**: nearly $4\,\pi$ homogeneous area coverage and acceptance.
- **Larger effective area**: 24 3-inch PMTs have a larger effective area than one 10 inch PMT.

- **Improved photon counting**: a larger number of smaller PMTs lead to a more precise derivation of the number of photons detected.
- **Possibility to use coincidences**: Background signals like the dark rate can be suppressed by using signals from different PMTs.

While bringing a lot of benefits there are comparably few disadvantages. One of them is the discarded *mu-metal* shield. The shield was discarded due to a number of factors: It blocks incoming photons, takes up space in the pressure vessel and costs money. Due to the smaller diameter of the PMTs of the mDOM, compared to the DOM PMTs, the effect of the magnetic field was expected to be neglectable and a shielding not necessary.

Mu-metal is an alloy of around 80% nickel, 15% iron and 5% copper and molybdenum or traces of other components. The magnetic permeability of this alloy is in the order of $10^{-5} \frac{\mathrm{N}}{\mathrm{A}^2}$ [19]. There are other similar metals with small variations in composition and permeability. Magnetic fields get redirected around the *mu-metal*, effectively shielding the inside of any object covered in *mu-metal*.

2.3 Photo multiplier tubes

The PMT of the mDOM is able to detect single photons and convert them into electric signals. How this is done and what the parameters of these signals are is focus of this section.

2.3.1 Basic functionality

The thin photosensitive part of a PMT is called the photocathode. When an incoming photon hits the cathode of the PMT, as shown in figure 2.11, the photon can get absorbed with a certain probability and the cathode emits an electron via the photoelectric effect.

The electron is accelerated towards the first dynode, passing the focusing electrodes. On impact, it frees more electrons from the dynode, thus multiplying the number of electrons, which get accelerated to the next dynode, where the process is repeated. This happens several times, producing a cascade of electrons before hitting the final anode, creating an electric signal. Each dynode is set to a different high voltage compared to the previous with a total voltage between cathode and anode of a few $\sim$kV, creating a constant acceleration towards the anode [20].

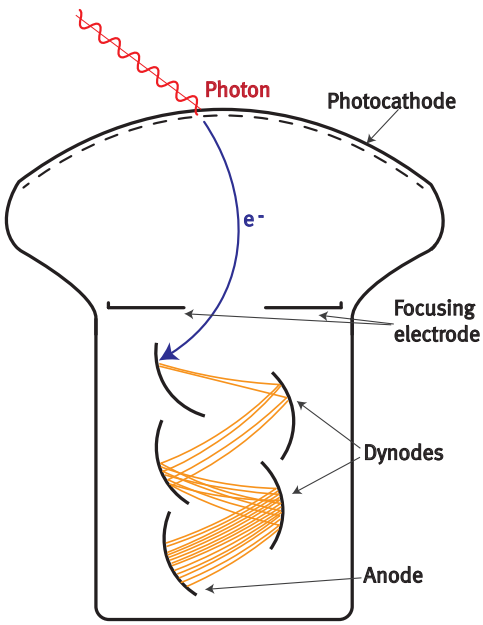

Figure 2.11: Basic illustration of the functionality of a PMT [11].

When such a cascade hits the anode it carries a certain charge and creates a signal. This signal can be read out in different modes, either directly as current or as voltage signal over a resistor. The

use of the generated current is called current mode and used when information of individual pulses is not necessary. Over a certain time interval the total current is integrated and all information on single events are erased. This makes the method useful for example, when the number of photons detected exceeds the resolution of a single signal anyway.

The usage of the voltage of the induced signal is called pulse mode and will be the primary mode of this thesis. The voltage pulses can be analysed to gain information about single events while measuring light of low intensity.

2.3.2 PMT properties

Depending on the materials and structure of the PMT, as well as on the environmental conditions, signals and performance may differ. Some key factors will be discussed in this section. A detailed description can be found in [20].

Quantum efficiency

The probability of an incoming photon to produce an electron output in the photocathode is called the quantum efficiency. It is highly dependent on the semiconductor material used for the photocathode and the wavelength of the incoming photon. Good photocathodes have a maximal quantum efficiency of approximately 40 % [21].

Transit Time

Each electron cascade needs a certain time to reach the anode based on their given path and starting velocity. This time is called the transit time. Small variations in transit time between electrons create a Gaussian shaped signal at the anode as displayed in figure 2.12. The measured transit times can be written in a histogram forming another distribution with a near Gaussian like shape. The width of this Gaussian is called the transit time spread (TTS) and is usually defined, as in this thesis, as the full width at half maximum (FWHM) of the signal. The TTS is the time resolution of the PMT, while the transit time itself influences the time response of the PMT. The rise time of the PMT is the time difference between 10% and 90% of the PMT peak height. Ideally the TTS should be small to maximise the time resolution [22].

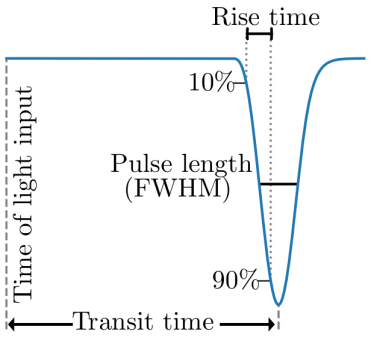

Figure 2.12: Sketch of the timing parameters the PMT signal pulse [11].

Gain

The number of electrons multiplies with each dynode. The gain g is the factor, by which an electron emitted by the photocathode gets multiplied by the whole dynode structure. It depends heavily on the applied voltage as well as the structure and materials of the

PMT.
A high gain has the advantage of giving a better signal to noise ratio, as well as a better reconstruction of the number of photon detected, by lowering the variance of the output charge.
The number of electrons emitted at dynode i per incoming electron is called the secondary emission coefficient δ_i. This coefficient is proportional to the applied voltage and the energy of the primary incoming electron. Depending on the structure and factors like the magnetic field, not all electrons emitted by a dynode reach the next one. The fraction between the number of electrons leaving dynode d_{i-1} and the number of electrons hitting the next dynode d_i is called the inter-dynode collection efficiency $c_i = d_i/d_{i-1}$. The total gain after N dynodes can therefore be described as

$$g = \prod_{i=1}^{N} \delta_i c_i. \tag{2.6}$$

Ideally $c_i = 1$, resulting in a maximal gain $g_{\max}$ when no losses occur in the PMT. The factor between the actual gain and the ideal gain is called global collection efficiency $CE = g/g_{\max}$ [22].

Dark rate
Not every PMT signal originates from a detected photon. Even without any input, signals can be measured at the anode. These signals are called the dark rate of the PMT, when operated in pulse mode. In current mode the signal measured without light source is called dark current. Main sources are thermionic emission of photoelectrons at the photocathode, scintillation of the surrounding glass or leaking currents inside the PMT. The dark rate changes heavily with the temperature and applied voltage.

Correlated Background
While the dark current is a major part of the background of each measurement, there are also background sources correlated to events:
Late pulses are created by back scattered electrons on the first dynode, which create a second signal when hitting the dynode again.
While a PMT is generally evacuated, the vacuum is not necessary ideal. When an electron ionises a gas atom on its way to a dynode, this ion will be accelerated towards the photocathode. Upon hitting the cathode, it releases secondary photoelectrons, which give a second **after pulse**.
If a photon crosses the photocathode and hits the first dynode, it creates an electron and thus an **early pulse** with less amplitude than an ordinary signal because it has not been multiplied at the first dynode.

2.3.3 PMT gain evaluation

To use a PMT efficiently, it is necessary to know the signal parameters regarding the number of photons hitting the cathode. To clarify this, a theoretical experimental setup is needed.

A pulsed light source, for example a LED (light-emitting diode), is pointed at the PMT. When the LED is activated, it creates a trigger signal for the PMT. This causes the PMT to integrate all incoming charges over a set integration gate as seen in figure 2.13. The total charge of the integration is written in a histogram. Most of the time the photons of the LED do not trigger a chain reaction in the PMT, either due to the quantum efficiency or the low intensity of the LED. If this is the case, the trigger still activates the integration, which is only done over the PMT background and the histogram has a peak at a certain background charge. This peak is called pedestal and is marked as the charge created by 0 photoelectrons (phe). When one or more photons create a signal in the PMT, their charges are written to the histogram and form the 1 phe, 2 phe, ... peaks in the charge histogram creating a charge spectrum.

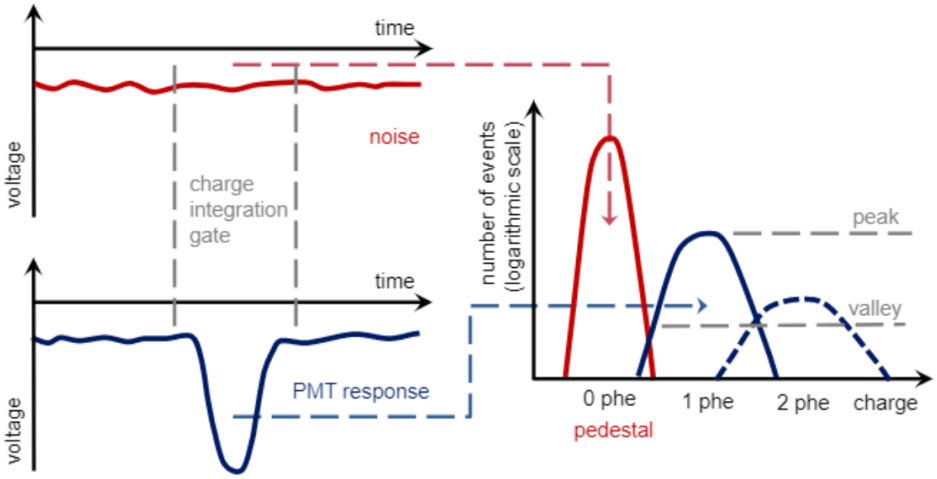

Figure 2.13: Illustration of the evaluation of the signal and the resulting charge spectrum [10].

To calculate the gain g analogue to [23], both the position of the pedestal Q_0 and of the one photoelectron (phe) peak Q_1 are required

$$\frac{Q_1 - Q_0}{e} = g, \tag{2.7}$$

where e is the elementary charge.

A precise description of the PMT response function $S_{\text{real}}(q)$ depending on the charge is necessary to calculate the gain. As first step, the background can be discarded and the ideal PMT response function $S_{\text{ideal}}(q)$ can be written as convolution of the response function of the dynode system $G_n(q)$ with the distribution of the number of photoelectrons emitted with a light pulse $P(n, \mu)$.
The first one can be described as a Gaussian distribution

$$G_n(q) = \frac{1}{\sigma_1 \sqrt{2\pi n}} exp\left(-\frac{(q - nQ_1)^2}{2n\sigma_1^2}\right), \tag{2.8}$$

where n is the number of initial photoelectrons, Q_1 is the average charge for one initial photoelectron at the anode and σ_1 is the standard deviation of the charge distribution. The mean of the Gaussian is therefore nQ_1 and its standard deviation is $\sqrt{n}\sigma_1$.

The second one is described by a Poisson distribution around μ, depending on the collection efficiency and the intensity of the light source

$$P(n,\mu) = \frac{\mu^n e^{-\mu}}{n!}. \tag{2.9}$$

This means $S_{\text{ideal}} = P(n,\mu) \otimes Gn(q)$ is given by

$$S_{\text{ideal}} = \sum_{n=0}^{\infty} \frac{\mu^n e^{-\mu}}{n!} \frac{1}{\sigma_1\sqrt{2\pi n}} exp\left(-\frac{(q-nQ_1)^2}{2n\sigma_1^2}\right). \tag{2.10}$$

$S_{\text{real}}(q)$ can be written as a convolution of an ideal charge distribution $S_{ideal}(q)$ and a background $B(q)$

$$S_{\text{real}}(q) = \int S_{ideal}(q') \cdot B(q-q')\mathrm{d}q'. \tag{2.11}$$

The background function $B(q)$ can be divided into two groups. The first one is made of low charge processes, like leaking currents, causing the width of the pedestal, which is described by a Gaussian distribution with standard deviation σ_0. The second group, described by an exponential function, is formed by discrete processes accompanying the measured signal like early pulses and noise, initiated by the light

$$B(q) = \frac{(1-\omega)}{\sigma_0\sqrt{2\pi}} exp\left(\frac{-q^2}{2\sigma_0^2}\right) + \omega \cdot \theta(q) \cdot \alpha \cdot exp(-\alpha q). \tag{2.12}$$

While ω is the probability of the occurrence of a discrete process, α is the coefficient of the exponential decrease. θ is a Heaviside function, which is 0 for $q < 0$ and 1 otherwise. To efficiently use equation 2.12 as fit function, some assumptions can be made to simplify it. Assuming the background intensity of the discrete background is low, it can be approximated as effective additional charge $Q_{sh} = \omega\alpha^{-1}$, reducing $B(q)$ aside the pedestal $n \geq 1$ to

$$B(q)|_{n\geq 1} = \frac{1}{\sigma_0\sqrt{2\pi}} exp\left(\frac{-(q-Q_0-Q_{sh})^2}{2\sigma_0^2}\right), \tag{2.13}$$

where Q_0 is the mean charge of the pedestal.
Applying this to equation 2.11, the real response description function produces

$$S_{\text{real}} = B(q-Q_0) \cdot exp(-\mu) + S_{\text{ideal}}(q-Q_0-Q_{sh})|_{n\geq=1}. \tag{2.14}$$

Here $exp(-\mu)$ is the probability of measuring 0 photoelectrons, describing the pedestal together with the ideal PMT-response S_{ideal}, which is shifted by the charge distribution of the background of discrete processes Q_{sh} and the pedestal position Q_0.

2.3.4 Influence of magnetic fields on PMTs

A moving charge q, like an electron, with the velocity $\vec{v}$ inside of a magnetic field $\vec{B}$, is subject to a force $\vec{F}$, induced by the magnetic field. This force was first described by James Clerk Maxwell in 1861 and described to its fullness by Oliver Heaviside (1889) and Hendrik Antoon Lorentz (1895).

The force, called Lorentz force, can be calculated by

$$\vec{F} = q \cdot \vec{v} \times \vec{B} \tag{2.15}$$

resulting in the acceleration of the particle due to the Lorentz force being always perpendicular to the field and the direction of movement.

As discussed in section 2.3, electrons in PMTs travel from the cathode over several dynodes to the anode. During this trip they are normally unshielded against external magnetic fields, which influence their path and by this the output signal. The gain depends on the number of electrons arriving at the anode. This number might vary, for example, depending on how many electrons get redirected by the Lorentz force and do not make it to a dynode or the final anode. Depending on the path of the electrons, the transit time changes and with it the transit time spread.

2.4 Magnetic fields

In this thesis, the influence of the magnetic field at the South Pole on the mDOM and its PMTs is investigated. The Earth magnetic field in Münster differs in strength and orientation from the field at the South Pole. How the magnetic field of the Earth looks like, how artificial fields can be created and how these fields influence the PMTs is described in this section.

2.4.1 Magnetic field of the Earth

The magnetic field of the Earth has roughly the shape of a dipole and is fundamental for life on Earth in its current form by shielding us from all kinds of charged particles. The strength of this field varies between approximately 22 and 67 µT and is weaker at the equator compared to the poles [25]. The major part of the field is generated by the geodynamo of the molten Earth core, where currents in the conductive iron generate electromagnetic fields. This process is highly complex and object of current studies and simulations [26]. Besides the effect of the geodynamo, electric currents in the ionosphere generate additional fields, which vary on daily basis by approximately 25 nT [27].

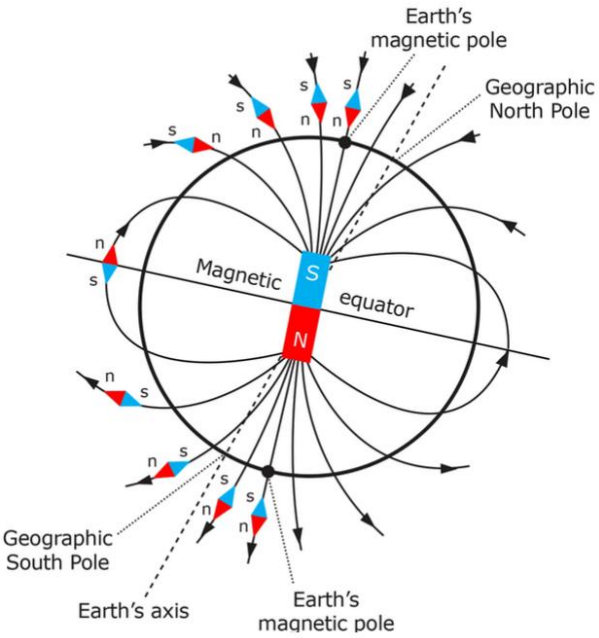

Figure 2.14: Schematic description of the magnetic field direction regarding the rotational axis of the Earth [24].

The poles of the magnetic field of the Earth nearly align with the geographic poles but are slightly shifted. Every few hundred thousand years, the last time about 770.000 years ago [28], these poles switch sides. Currently the magnetic South Pole is moving northwards, as seen in figure

2.15.

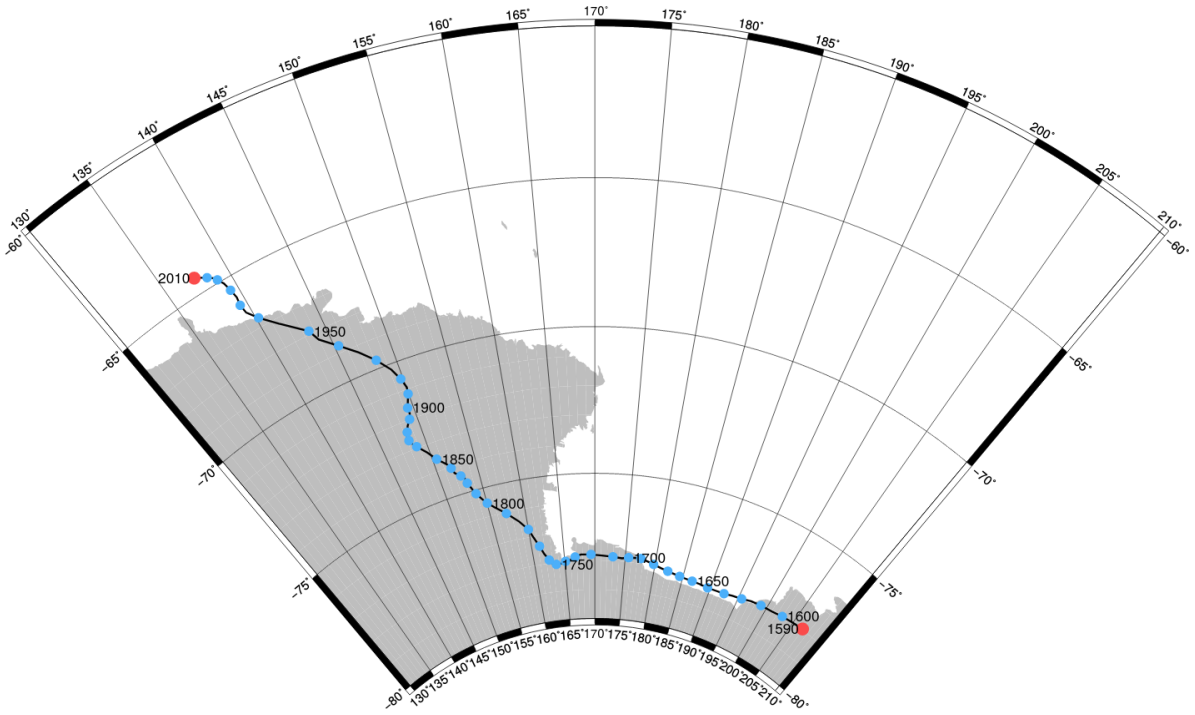

Figure 2.15: Movement of the magnetic South Pole between 1590 and 2010 [29].

The form and strength of the magnetic field greatly varies in orientation and strength, depending on the position on the surface, as shown in figure 2.16. The field in Münster has a strength of 49,3 µT, while the field at the IceCube detector has a strength of 54,7 µT [30]. The field in Münster is orientated less vertically compared to the field at the South Pole. Even though IceCube has a volume of roughly 1 km^2, it can be assumed to have the roughly same strength and orientation across the full volume.

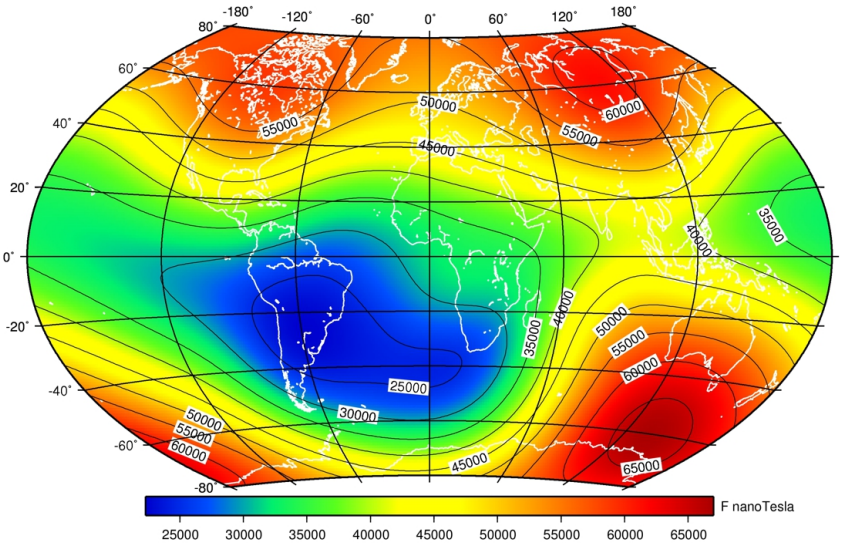

Figure 2.16: Colour map of the strength of the Earth magnetic field depending on the latitude and longitude [31].

2.4.2 Helmholtz coils

Electrons travelling in a straight wire generate constant magnetic fields around the wire. This effect was described 1820 by the Biot-Savart-Law, named after two French physicists, Jean Baptiste Biot and Felix Savart, who derived the magnetic flux density at a point due to a nearby current carrying conductor.
For a current along a straight wire of the length L, the Biot-Savart-Law is

$$\vec{B}(\vec{r}) = \frac{\mu_0 I}{4\pi} \int \frac{\mathrm{d}S_{r'} \times (\vec{r} - \vec{r}')}{|\vec{r} - \vec{r}'|^3}, \tag{2.16}$$

where $\mu_0 \approx 4\pi \cdot 10^{-7} \frac{\mathrm{H}}{\mathrm{m}}$ is the vacuum permeability, I is the current, $\vec{r}$ is a vector to any given point P and $\mathrm{d}S_{r'}$ is the path of the wire. The assumption that the wire is orientated along the Z axis, as shown in figure 2.17, gives $\mathrm{d}S_{r'} = \vec{e}_z \mathrm{d}z'$, $\vec{r}$ can be written as $\vec{r} = \rho\vec{e}_\rho + z\vec{e}_z$ and $\vec{r}' = z'\vec{e}_z$.

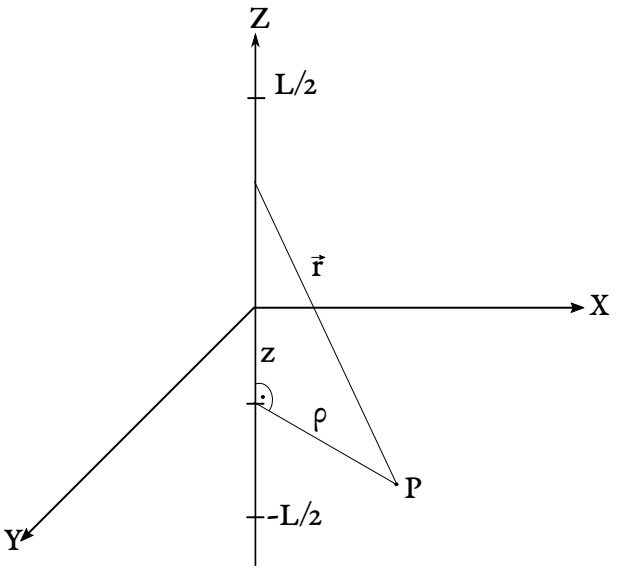

Figure 2.17: Illustration of the calculation approach for the magnetic field generated by a constant current in a finite straight wire for any given point.

This changes the formula to

$$\vec{B}(r) = \frac{\mu_0 I}{4\pi} \int_{-\frac{L}{2}}^{\frac{L}{2}} \frac{\vec{e}_z \mathrm{d}z' \times (\rho\vec{e}_\rho + z\vec{e}_z - z'\vec{e}_z)}{|\rho\vec{e}_\rho + z\vec{e}_z - z'\vec{e}_z|^3}. \tag{2.17}$$

Solving the vector product results in

$$\vec{B}(r) = \frac{\mu_0 I}{4\pi} \int_{-\frac{L}{2}}^{\frac{L}{2}} \frac{\vec{e}_z \mathrm{d}z' \times \rho\vec{e}_\rho}{(\rho^2 + (z - z')^2)^{\frac{3}{2}}} = \frac{\mu_0 I \rho \vec{e}_\phi}{4\pi} \int_{-\frac{L}{2}}^{\frac{L}{2}} \frac{\mathrm{d}z'}{(\rho^2 + (z - z')^2))^{\frac{3}{2}}}. \tag{2.18}$$

and finally the integral leads to

$$\vec{B}(r) = \frac{\mu_0 I}{4\pi\rho^2} \cdot \left(\frac{z - \frac{L}{2}}{\sqrt{\rho^2 + \left(z - \frac{L}{2}\right)^2}} - \frac{z + \frac{L}{2}}{\sqrt{\rho^2 + \left(z + \frac{L}{2}\right)^2}} \right) \cdot \begin{pmatrix} -y \\ x \\ 0 \end{pmatrix}, \tag{2.19}$$

where $\rho = \sqrt{x^2 + y^2}$. As expected, the magnetic field winds around the wire, with the field strength proportionally to the applied current.

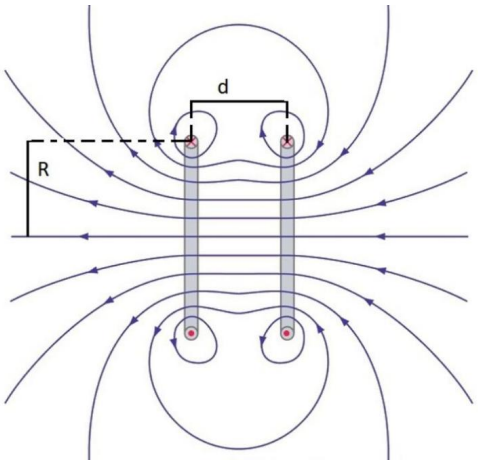

Figure 2.18: Sketch of the field generated by a pair of Helmholtz coils. Taken from [32] and edited.

Helmholtz coils, named after the German physicist Hermann von Helmholtz, consist of two coils with radius R, separated by the ideal distance $d = R$, which produce a nearly homogeneous field in their centre, as shown in figure 2.18.

Normally, these coils are circular and the field strength in the centre corresponds to the Biot-Savart-law and obeys

$$B(0) = \left(\frac{8}{5\sqrt{5}}\right) \frac{\mu_0 N I}{R}, \tag{2.20}$$

where N is the number of windings.

Besides circular coils any other coil type is possible and produces more or less homogeneous fields. Square Helmholtz coils produce very similar fields with a slightly larger homogeneous area with small changes in the shape of the field. For square Helmholtz coils [33] of the length $L = 2 \cdot R$, the ideal distance between the coils changes to $d = 0.5445 \cdot L$ and the field in the centre of the coils can be calculated by

$$B(0) = \left(\frac{4}{1.2965\pi \cdot \sqrt{2.2965}}\right) \frac{\mu_0 N I}{R}. \tag{2.21}$$

2.5 Previous investigations on the influence of magnetic fields on PMTs

Every experiment using PMTs, like IceCube, KM3NeT, Super-Kamiokande and others, face the problem of the Earth magnetic field influencing the output of their PMTs. If and what counter measurements are necessary is different from case to case. The results of the investigation for the DOM and what tests were already done on the Hamamatsu R12119-02 used in the mDOM, are summarised in the next sections.

2.5.1 Magnetic field influence measurements on the 10-inch PMTs of the DOM

The core of the DOM is a Hamamatsu R7081-02 (shown in figure 2.19) photo multiplier tube with a spherical photocathode, 10 dynodes and a diameter of 10-inch [34]. Tests on the gain and TTS dependency were made by rotating the PMT horizontally in the Earths magnetic field. Both gain and TTS were measured once with and once without a *mu-metal* shield, as shown in figure 2.20 and 2.21 [35].

Figure 2.19: The Hamamatsu R7081-02 10-inch PMT used in the DOMs [34].

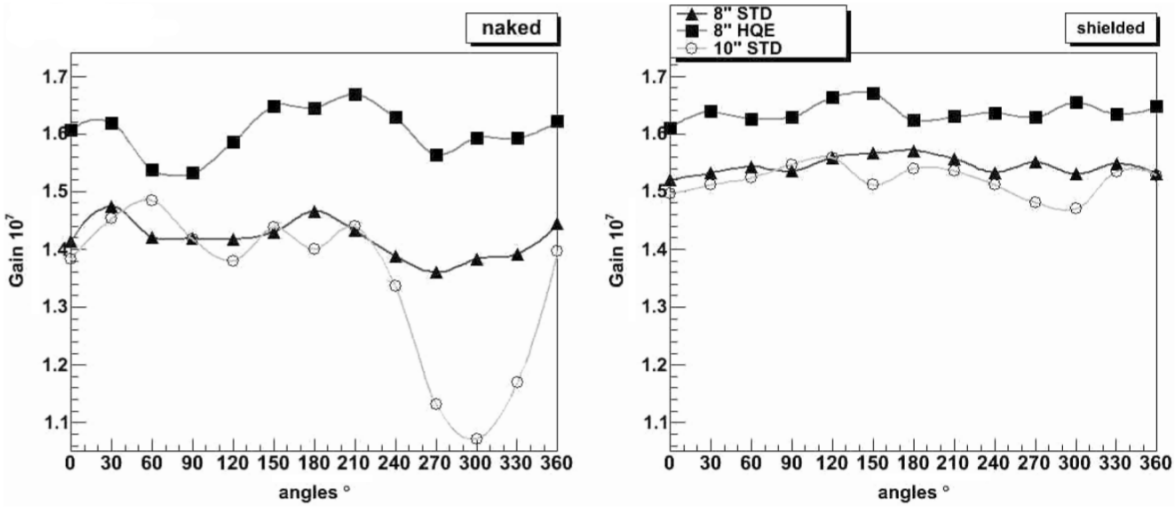

Figure 2.20: Influence of the Earth magnetic field orientation on the gain of two 8-inch PMT and one 10-inch PMT. **Left:** Without shielding. **Right:** With a *mu-metal* shield [35].

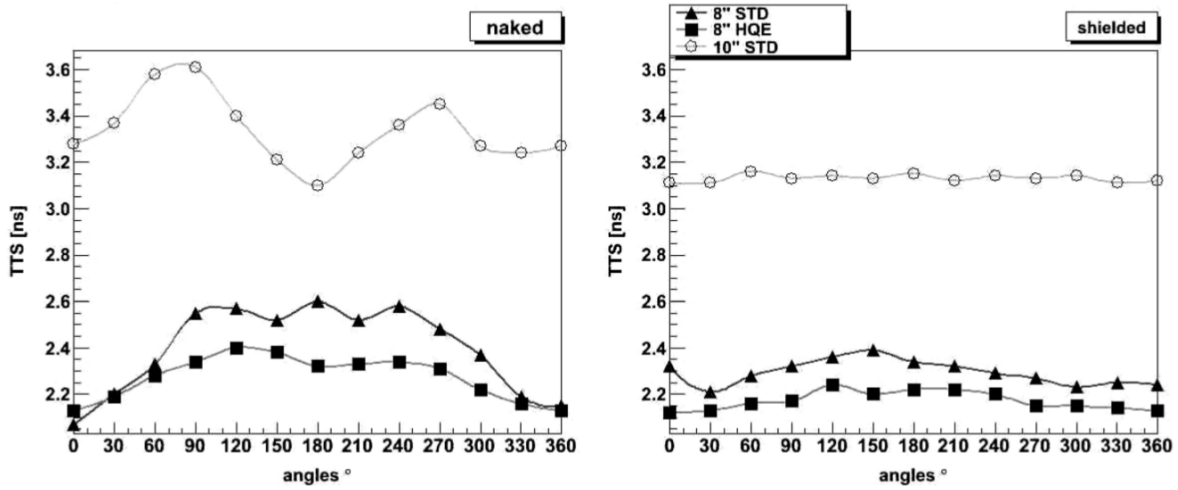

Figure 2.21: Influence of the Earth magnetic field orientation on the TTS of two 8-inch PMT and one 10-inch PMT. **Left:** Without shielding. **Right:** With a *mu-metal* shield [35].

Important in this case is the data for the 10-inch PMT. The unshielded PMT shows higher fluctuations around a gain of approximately $1.4 \cdot 10^7$ with a gain valley of about $1.1 \cdot 10^7$ at 300 °. The gain measured with shielding shows smaller fluctuations with a higher medium gain of approximately $1.5 \cdot 10^7$ and no significant deviations.

The TTS is sensitive to the orientation of the magnetic field as well and shows higher fluctuations around a TTS of $\approx 3.3\,\text{ns}$ with no shielding and smaller fluctuations with a smaller average TTS of $\approx 3.1\,\text{ns}$ with an applied shield.

To avoid those huge fluctuations all DOM modules have their PMT surrounded by such a *mu-metal* cage.

2.5.2 Previous magnetic field influence measurements on the 3-inch PMTs of the mDOM

The effect of the magnetic field on electrons increases with their velocity and the length of the path they travel. While the DOM uses one 10-inch PMT, the mDOM uses 24 far smaller 3-inch PMTs. Accordingly, the effect of the field on the signal parameters of the PMT is expected to be much smaller.
To investigate this, similar tests to the ones done on the DOM, were done by Lukas Kuballa at the University of Münster as part of his bachelor thesis [36].

A LED was placed in a light isolating dark Box in front of a diffuser to accomplish uniform illumination of a Hamamatsu R12119-02 PMT, which was placed on the opposite side of the box, as shown in figure 2.22. LED, diffuser, and PMT were placed on a rotatable plate, together with a magnetic field sensor next to the PMT. Analogous to figure 2.20 and 2.21 the gain and TTS were measured depending on the rotation of the PMT. The magnetic field had a vertical component of $(43.9 \pm 1.3)\,\mu\text{T}$ and a horizontal component of $(18.4 \pm 0.7)\,\mu\text{T}$. At 0 °, the symmetry axis of the PMT was aligned with the horizontal component of the B-field.

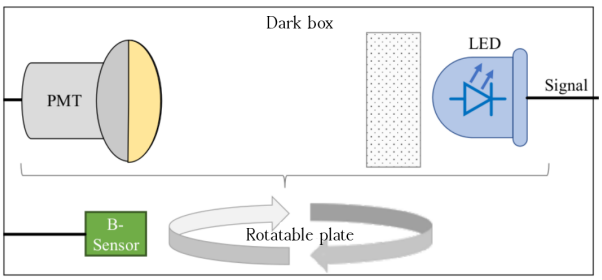

Figure 2.22: Schematic of the basic setup used by Lukas Kuballa. Taken from [36] and edited.

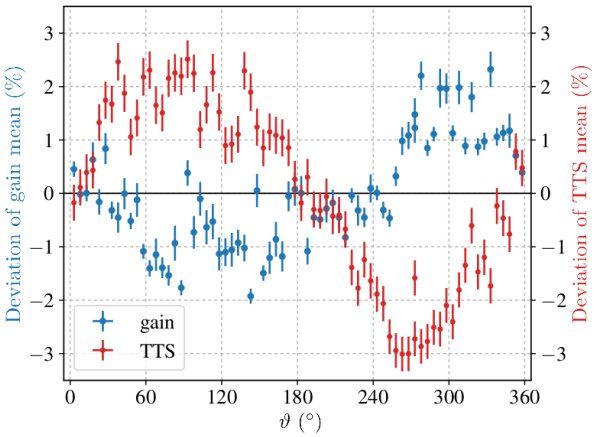

Figure 2.23: Mean deviation of the gain and TTS from the average of the R12119-02 PMT, depending on the horizontal orientation in the magnetic field in Münster. Taken from [36] and edited.

As shown in figure 2.23, the gain shows variations of approximately ±2% and the TTS of about ±3%, depending on the angle and thus the magnetic field orientation.

It was checked, whether the orientation of the first dynode has an influence on the PMT parameters.

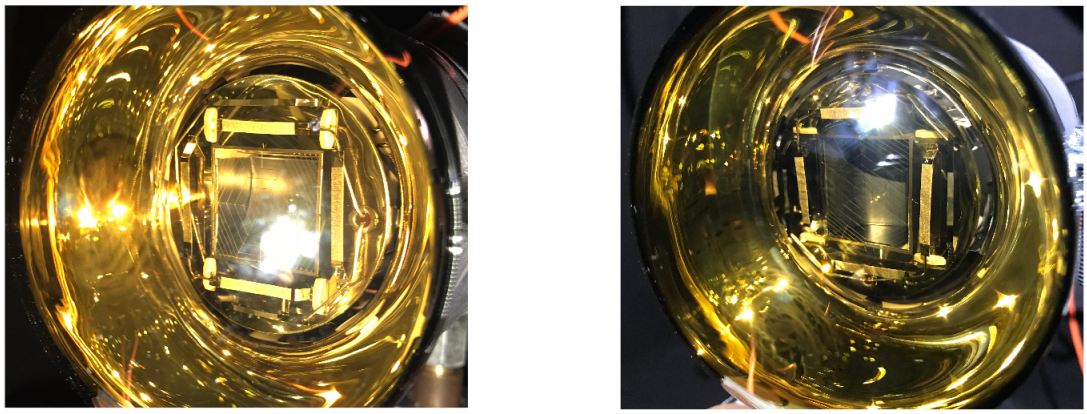

Figure 2.24: Photographs of the orientation of the first dynode of the PMT. **Left:** Bent upwards. **Right:** Bent to the right [36].

The PMT was rotated around its symmetry axis, until the first dynode was bent upwards in the first measurement and sideways in the second measurement, as presented in figure 2.24.

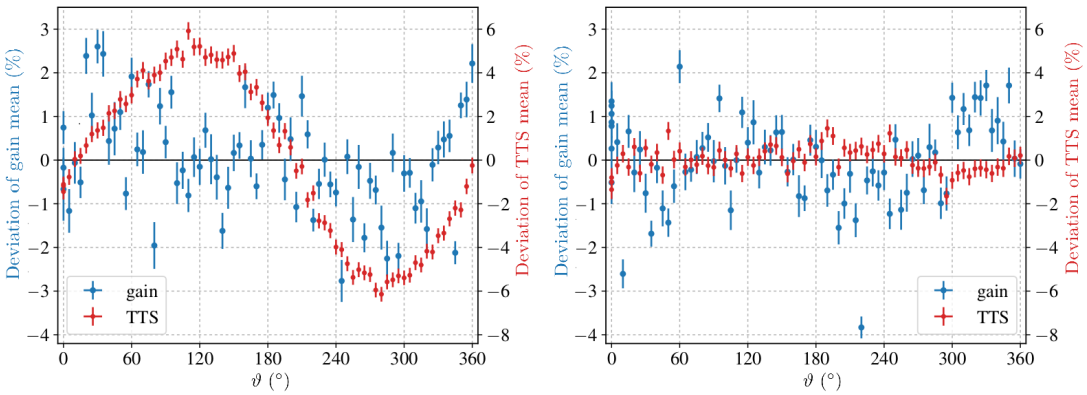

Figure 2.25: Mean deviation of the gain and TTS from the average of the R12119-02 PMT depending on the horizontal orientation in the magnetic field in Münster and explicit first dynode orientation. **Right:** With the first dynode bent upwards. **Left:** With the first dynode bent to the right. Taken from [36] and edited.

The results of the measurements are shown in figure 2.25. The TTS shows a completely different behaviour depending on the dynode orientation. With the first dynode bent upwards, the TTS data follows a sinus shape, similar to figure 2.23, whereas the TTS data for the dynode bent sideways does not show great deviations from the average at all. The thesis of Lukas Kuballa states that it is suspected that the gain measurements were not precise enough. This explains why the gain does not show any distinct shape and does not seem to be affected by the orientation of the first dynode.

It is evident that the magnetic field in Münster has an effect on the PMT, which is going to be used in the mDOM, making further investigations necessary. The PMTs of the mDOM will be orientated in all directions in a magnetic field stronger than the one in Münster.

Ideally, a test setup should be able to do both, orientate a magnetic field in all directions and vary the strength to match the field at the South Pole. These boundary conditions were the foundation for the setup introduced in the next chapter.

3 Set up of q magnetic field test stand

In the following section the planing, set up and commission of a square Helmholtz coil cube will be described. Subsequently, the field generated by the coils will be analysed and characterised.

3.1 Planing and simulation

Beside being able to create magnetic fields in all directions of different strengths, the setup should be large enough to house the entire mDOM and be nearly homogeneous in the relevant volume. Additionally, it has to be fairly simple to construct, to be done in the given time frame of a master thesis and easy to dismantle for movement and storage. Ideally it should be robust, light, and save to handle without too many precautions.

3.1.1 Basic setup considerations

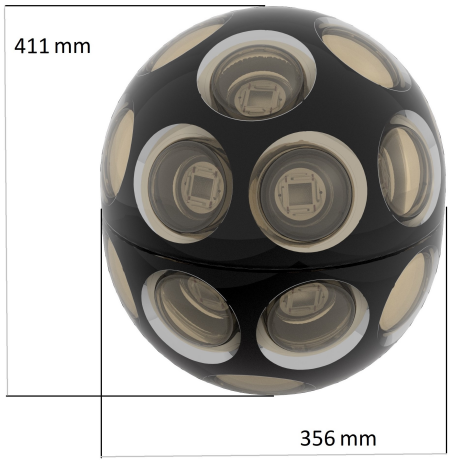

Figure 3.1: Dimensions of the mDOM module. Courtesy of the IceCube Collaboration.

Artificial magnetic fields are most easily generated by coils. To get a homogeneous field, Helmholtz coils discussed in section 2.4.2 are the obvious choice. The size of the mDOM, shown in figure 3.1, leads to a homogeneous field area of at least 411 mm in diameter. Because of construction complexities, square coils were given preference over round coils. Given these first considerations, a lot of specifications and adjustable parameters can be found:

- **Size of the coils:** The coils have to be wide enough for the mDOM and sufficiently homogeneous in the relevant volume.
- **Strength of the field:** As discussed in section 2.4.2, the strength of the field is proportional to $\frac{I \cdot N}{R}$. The coils should at least be able to compensate for the field in Münster and to generate simultaneously the field at the South Pole.

- **Number of windings N:** More windings increase the maximal reachable field strength but increase the construction complexity.
- **Strength of current I:** On the one hand, higher currents generate stronger fields. On the other hand, they are potentially dangerous and the heat development due to wire resistance increases.
- **Heat generation:** Depending on the temperature of the wires, the resistance changes. With the resistance, the current and the magnetic field changes, leading to fluctuations in the field. In the worst case, a possible structural failure could happen. Ideally the setup should be temperature constant.
- **Radius of the used wire:** An increasing wire radius lowers the resistance of the cable, the heat production and thus allows higher currents, but thicker wires are harder to handle as coil wires and take up more space.
- **Material and electronics availability:** Frame and coil construction materials, as well as electronics, should be easy to handle, be affordable, and available in a time frame suitable for a master thesis.

3.1.2 Analytic calculation of the magnetic field of a square Helmholtz cube

Based on square Helmholtz coils, the resulting magnetic field can be solved analytically depending on the size of the coils, the applied current and the number of windings. To achieve a homogeneous field in all directions, three sets of Helmholtz coils are necessary, as shown in figure 3.2.

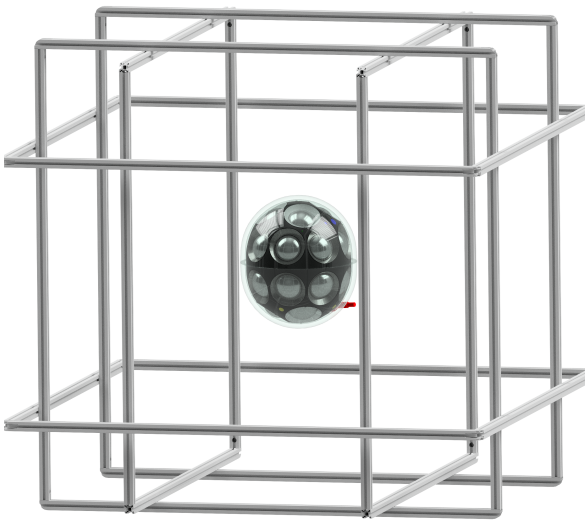

Figure 3.2: Schematic of the build Helmholtz cube with a mDOM as comparison.

To simplify the analytic solution, some assumptions were made:

- The wires of the coil have no radius,
- there is no frame or anything beside the wires,
- all wires take up the same space if more than 1 winding is given.

Without these assumptions, the complexity of the equations would have risen significantly. However these calculations are mainly done to get a parameter frame for the setup and the accuracy of the solution were still expected to be sufficient.

Magnetic fields can be added together using the superposition principle. Therefore it is possible to construct the field of a Helmholtz coil, using the field of 4 wires of the length l added together to form one winding of the coil. Additional windings just add a multiplicity N to the field B.

To simulate the field of the Helmholtz coils, the analytic solutions for straight wires of equation 2.19 was implemented in Python.

In the following figures, the length of the coil sides is $L = 1.38\,\mathrm{m}$, the number of windings is set to $N = 7$ and the used current is $I = 13\,\mathrm{A}$, corresponding to real parameters used for the smallest coil.

Initially, the B-field of a single wire was calculated while varying the size of the coils and applied current. The wire was placed in a coordinate system at $x = L/2$ and $y = -L/2 \cdot 0.5445$ (see section 2.4.2) ranging from $z = -L/2$ to $z = L/2$. Afterwards, a second wire shifted to the side at $x = L/2$ and $y = L/2 \cdot 0.5445$ was introduced, with opposite current direction. Subsequently the Ecoil was closed by adding two more wires at the end of the previous ones. To form the other coil of the Helmholtz coil, identical wires were added symmetrically to the other side of the z-y-plane forming two complete coils, as shown in figure 3.3.

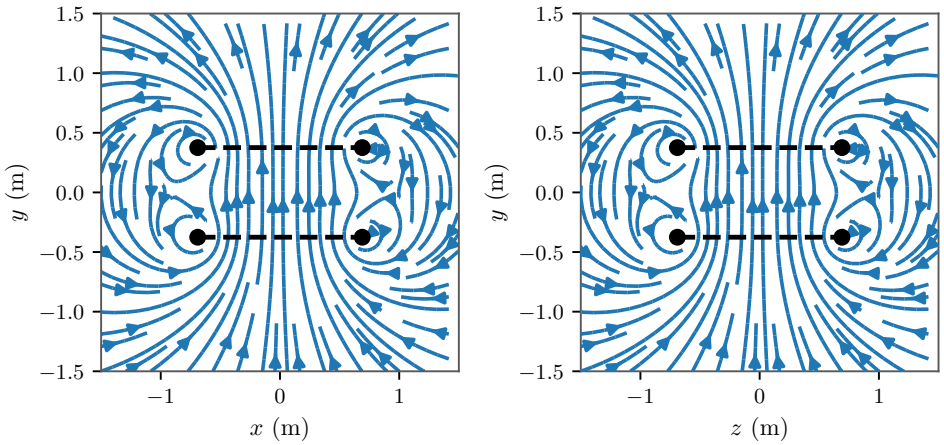

Figure 3.3: Orientation of the magnetic field of a Helmholtz coil pair, with dotted line as illustration of the coil positions. **Left:** Cut through the x-y-plane at $z = 0$. **Right:** Cut through the y-z-plane at $x = 0$.

Homogeneity of the Field

The size of coils L depends on the necessary homogeneous area for the whole mDOM (3.1.1). To estimate the homogeneity of the field, the deviation from the centre of the field B_0 was calculated for every position. In theory, the field between the coils is exactly aligned with the symmetry axis of the coils. The deviation of the field is thus shown by the deviation of the B_i-component, corresponding to the symmetry axis i. The deviation $(B_0 - B_y)B_0$ was used to determine an homogeneous area, where the field is homogeneous up to 1 %, as presented in figure 3.4.

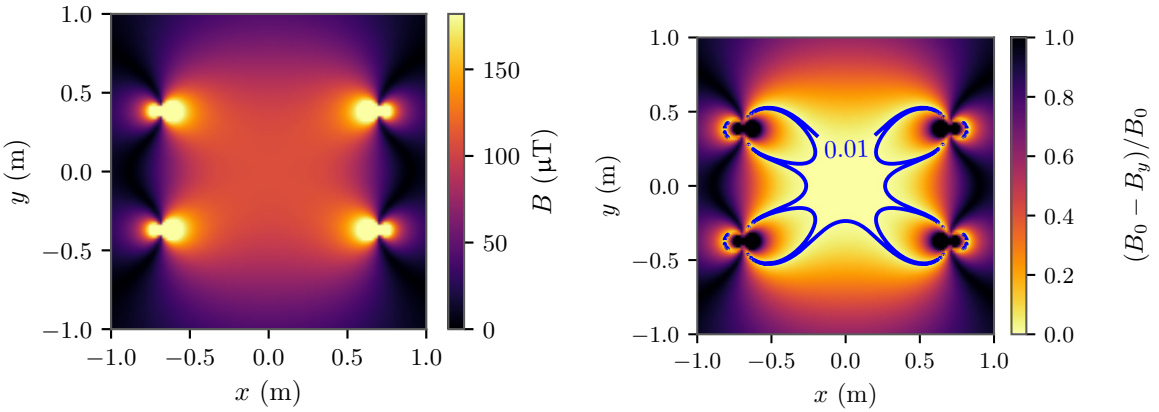

Figure 3.4: Left: Strength of the B_y-field. **Right** Outline of the area to 1 % homogeneous.

Because of the star shape of the homogeneous area and the volume respectively, three cuts along the axes of the coordinate system presented in figure 3.5 were made and the shape of the homogeneity taken as reference value.

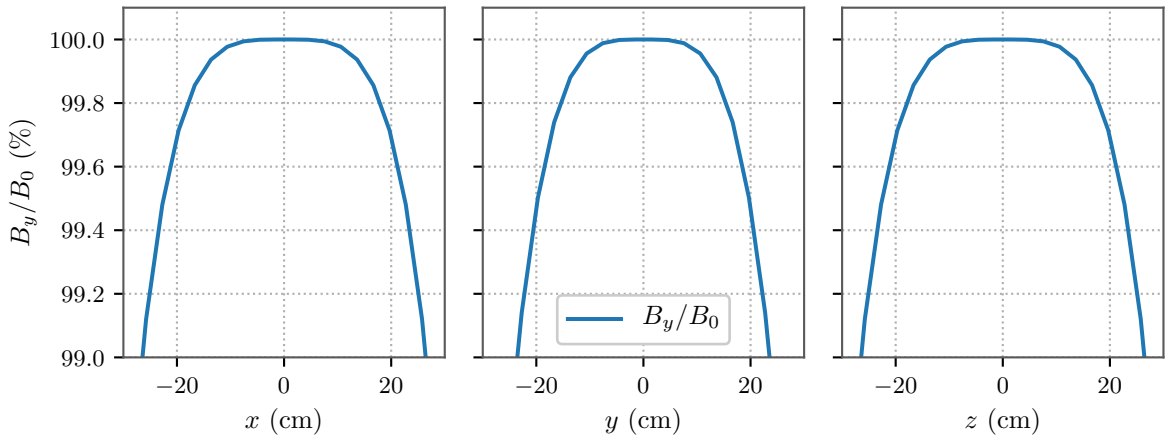

Figure 3.5: Cuts through B_y/B_0 along the y-z-, x-z- and x-y-plane.

Calculating the distance d_{homo} from the coils centre, when the field homogeneity falls below 99%, yields 22.7 cm for the y axis and 25.7 cm for the x and z axis. Setting this into proportion to the diameter of the coil d_{coil} yields a homogeneous range for y of

$$22.7 \cdot 2/138 \approx \frac{1}{3} \Rightarrow d_{\text{homo}} \approx d_{\text{coil}}/3. \tag{3.1}$$

The homogeneous area should cover at least the largest extension of the mDOM of 41.1 cm. The minimal size of the coils can therefore be determined to be 41.1 cm · 3 = 123.3 cm. 138 cm as used in previous calculations, are therefore sufficient for the mDOM.

Strength of the field and heat production

The strength of the field should be at least strong enough to compensate for the field in Münster (≈ 49.3 µT) and generate the field at the South Pole (≈ 54.7 µT) simultaneously.

This sets necessary maximal needed field strength to = 103.4 µT. An illustration of the strength of the magnetic field of one coil pair is plotted in figure 3.6.

figure 3.6.

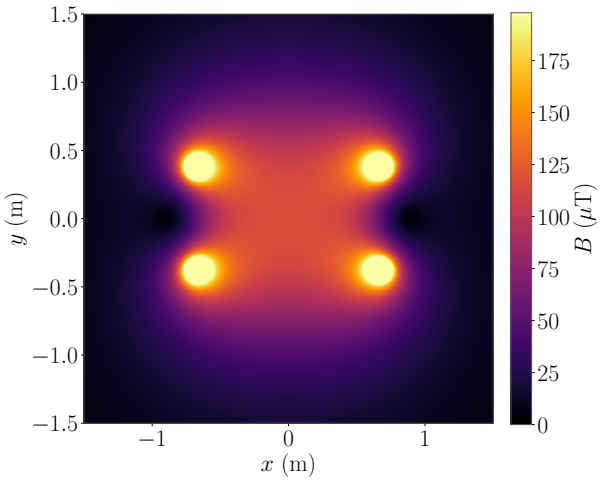

Figure 3.6: Illustration of the field strength of a Helmholtz coil pair.

The necessary product of the number of windings N and applied current I can be determined, by using the strength of the field in the centre of the coils. Calculating this field for a coil with a length of $L = 1.38\,\mathrm{m}$ yields

$$B = 1.18 \cdot N \cdot I, \tag{3.2}$$

which can be solved for $B = 103.4\,\mu\mathrm{T}$ to determine $N \cdot I \approx 87.63\,\mathrm{A}$.

To minimise the number of windings and thus simplify the construction process, the current has to rise respectively. The maximum current I in a wire, while keeping the temperature stable over longer times, can be approximated with

$$I = \sqrt{\frac{2\pi^2 \cdot \Delta T \cdot \alpha \cdot r^3 \cdot 10^{-9} \alpha}{\rho \cdot (1 + \alpha_T \cdot \Delta T)}}. \tag{3.3}$$

Here r is the radius of the wire, α the heat transition coefficient, α_T the temperature coefficient of copper at 20 °C, ρ the density of copper and ΔT is the maximal accepted temperature rise [37].
Alternatively, the maximum temperature rise can be calculated analogously using

$$\Delta T = \frac{-I^2 \cdot \rho}{I^2 \cdot \rho \cdot \alpha_T - 2\pi^2 \cdot \alpha \cdot r^3 \cdot 10^{-9}}. \tag{3.4}$$

Both can be plotted for visualisation as done in figure 3.7.

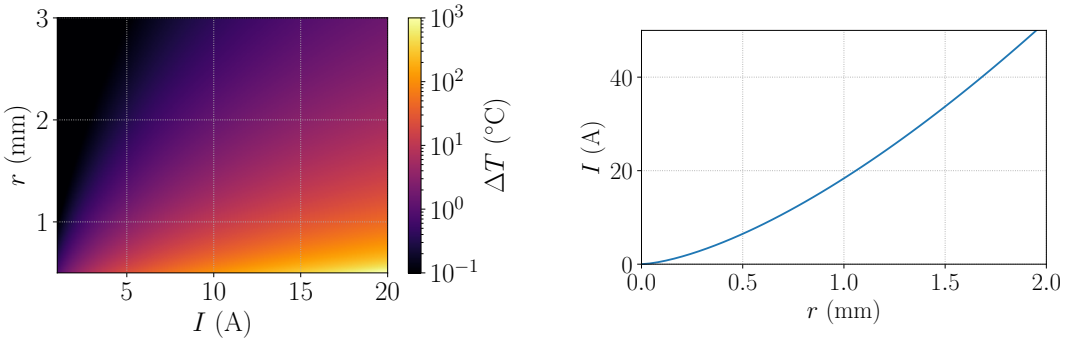

Figure 3.7: Left: Expected temperature rise in a wire in long term use depending on the wire radius and applied current. **Right:** Maximum possible applied current, depending on the wire radius for a maximum acceptable temperature rise of 20 °C.

As expected, the temperature rises for a smaller radius, as well as for higher currents. Therefore, a low current and high radius lead to smaller temperature changes, which is preferable for the coil setup to keep it stable. Choosing $\Delta T = 20\,°\mathrm{C}$, which should be sufficiently low, limits the range of the maximal applicable current I, depending on the used wire radius.

Orientation of the wires and coils

It can be assumed that the layers of wires are, in sum, parallel to the frame and thus only the frame orientation plays a critical role. To check how strong the orientation of the coils to each other affects the homogeneity of the field, some additional calculations were done analogously to the analytic research before. This time, the orientation of the coils were rotated by 3°, which yielded a decrease in the homogeneity of less than 1 %.

3.1.3 Specification of setup parameters and design

The calculations of the previous section were used to determine the boundaries of the setup parameters listed in table 3.8.
To keep the construction complexity low, a small number of 7 windings was chosen. This sets the minimum current to $87.63/7 = 12.52\,\mathrm{A}$. For a current of $I = 13\,\mathrm{A}$ and a maximum accepted temperature rise of 20 °, the radius of the wire has therefore to be at least $r \approx 0.8\,\mathrm{mm}$.
This matched the available equipment of insulated copper wire, with $r = 1\,\mathrm{mm}$ and power supplies supporting currents up to 40 A.

Parameter	Boundaries	Realisation
Minimal homogeneous area/distance d_{homo}	411 mm	460 mm
$\rightarrow$ Diameter of the smallest coil d_{coil}	$411 \cdot 3\,\text{mm} = 1233\,\text{mm}$	1380 mm
Number of windings N		7
Current I		13 A
$\rightarrow$ Field strength B	$N \cdot I \cdot 1.18 > 103.4\,\mu\text{T}$	107.28 µT
Minimal wire radius r	0.8 mm	1 mm

Figure 3.8: Calculated boundaries and chosen parameters for the coils of the square Helmholtz coil cube.

To cross check if the necessary voltage could be achieved by the power supplies, the total resistant of one coil was calculated. This can be done with the cross section area of the wire $A = \pi \cdot r^2 = 3.14\ \text{mm}^2$, the resistivity of copper $\rho_{copper} = 0.0171\,\frac{\Omega \cdot \text{mm}^2}{\text{m}}$ and length of the wire $l = 1.38\,\text{m} \cdot 7 \cdot 4 = 38.64\,\text{m}$ using

$$R_{\text{coil}} = \frac{\rho\, l}{A} \approx 0.22\,\Omega. \tag{3.5}$$

The minimum voltage can then be calculated to $U = R_{\text{coil}} \cdot I \approx 2.74\,\text{V}$. This has to be doubled to compensate for using two coils in series, which is sufficiently covered by the power supplies: *SM 1540-D* from *Delta Elektronika BV* supporting voltages of up to 15 V.

The frame was constructed using Aluminium profiles of the company *Kanya* [38]. A cross section of the profile is shown in Figure 3.9. Given that the coils can not take up the same space, have a thickness of 30 mm and the smallest coil has a diameter of 1380 mm the other two coil pairs need to have a diameter of 1440 mm and 1500 mm.

The profile system allows easy construction and modifications and is made from aluminium, which has a magnetic susceptibility of $0.62 \cdot 10^{-9}\,\text{m}^3/\text{kg}$ and therefore does not interfere much with the magnetic field. The cavities in the profile, used to connect them with others, were also used as wire canals for the coil to achieve a tight wire layout as illustrated in figure 3.9.

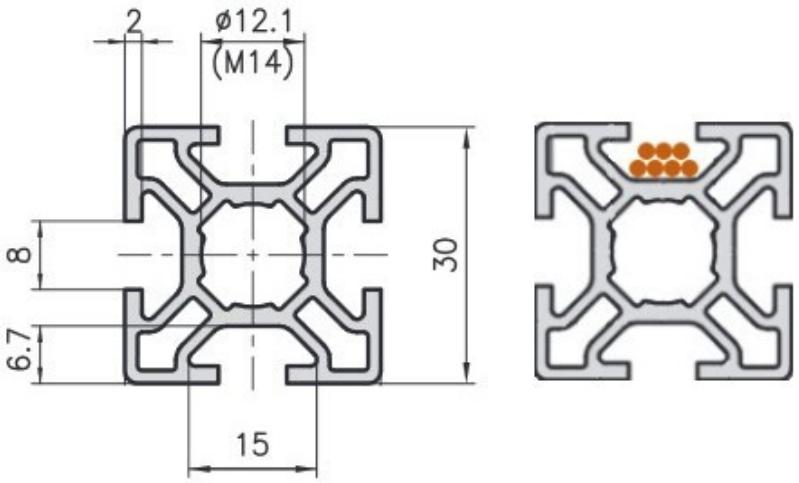

Figure 3.9: Sketch of the profiles used for the coil frames with dimensions in mm and illustration of the wire inlay. Taken from [38] and edited.

To check whether the coils would get too heavy, the maximal weight of the biggest coil with a diameter of $d = 1.5\,\mathrm{m}$ was calculated. The weight of the aluminium profiles of the biggest coil was calculated to be $0.9\,\frac{\mathrm{kg}}{\mathrm{m}} \cdot 4 \cdot 1.5\,\mathrm{m} = 5.4\,\mathrm{kg}$ [38]. The weight of the copper cables is roughly $8960\,\mathrm{kg/m^3} \cdot 4 \cdot 7 \cdot 1.5 \cdot \pi \cdot 0.001^2 \approx 1.18\,\mathrm{kg}$, making the total weight of a coil less than 7 kg, which should be sufficiently light to be handled by a single person.

3.2 Construction and commission of a square Helmholtz cube

The construction process will be explained in the following section, along with the description of the used hardware and electronics, with references to the associated Python scripts, whose documentations can be found in the appendix.

3.2.1 Construction process and implementation

To achieve an ideal field, every layer of wire should lay neatly next to each other, as shown in figure 3.9. In reality, this is close to impossible to achieve without special equipment, which was not accessible for this thesis.
Ideally, a machine would produce the coil, which straightens the wire enough to lie tightly together in the quadratic frame. For this setup, built without mechanical support, the frame of the coil was mounted on top of a table and the wire was rolled from the round coil directly into the cavities of the profile. To straighten the wire, tension was put onto it whenever reaching the corners of the coil.

In principle, the wires are insulated by a protective coating and the frame was insulated by an aluminium-oxide layer to eliminate short circuits. The corners of the frame shown in figure 3.10 were cut round to achieve a smooth connection between each side. This had the downside of destroying the protective insulation coating and left sharp edges from the structure of the profile. These edges teared the wire in several occasions before being removed sufficiently or covered with cushion.

Putting a lot of tension onto the wire to keep it neatly in the frame had the disadvantage of creating fractures in the coating of the wire, especially when scratching along the sharp edges of the profiles. Short circuits between the wires and the frame or the wires themselves were the result of these fissures, leaving the coils unusable.

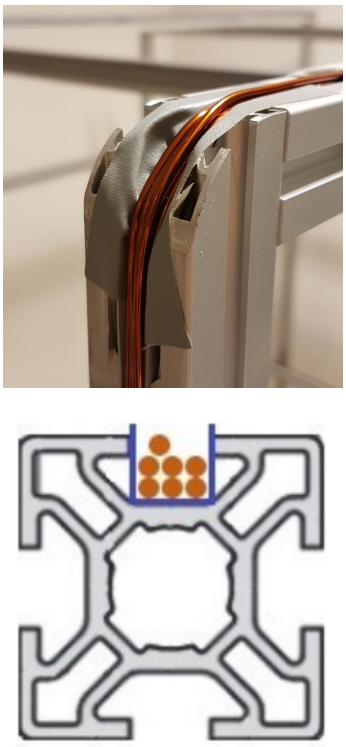

Figure 3.10: Top: Padded and insulated edges of the frame. **Bottom:** Added plastic insulation to the cavities of the profile.

After some initial struggles, the areas in question were covered with padding, further insulated with tape and varnished with insulating coating. Furthermore, plastic profiles, as seen in figure 3.10, were added to the cavities of the profiles to finally suppress short circuits.

To check whether short circuits were still problematic, the electric resistance between each wire and its corresponding coil frame and the electric resistance of the wires themselves was measured. The resistance between the wires and the frames of the coils was determined to be infinite by the multimeter and could therefore be regarded as sufficiently insulated. The electric resistance $R = 0.22\,\Omega$ (calculated in equation 3.5) of the wires of each coil was taken. While the resistance was slightly higher than calculated, with

$(0.28 \pm 0.02)\,\Omega$, it can be assumed that no critical short circuits between the wire layers had occurred. The higher resistance has a few possible sources like fractures, which appeared during the winding, not enough pressure applied with the probes during the measurement or the used measuring device, since it was used at the limits of its measuring range.

Even though a lot of tension was applied to the wire, a neat arrangement in the cavities was not achieved entirely. The wires lie in the cavities of the frame but cross and overlap each other.

Each coil is connected to a power supply unit with one end of the wire and connected to its partner coil with the other wire end in a series connection. This way, each set of coils is controlled and powered separately. The frame is connected with profile connectors from *Kanya*, making assembling and dissembling easy. The final setup is shown in figure 3.11.

In the following measurements, the symmetry axes of the cube will be called x, y and z. The x-axis is associated with the symmetry axis pointing towards the wall on the right, the y-axis point towards the wall in the back and the z-axis is facing upwards. (0,0,0) is defined as the centre of the coils cube.

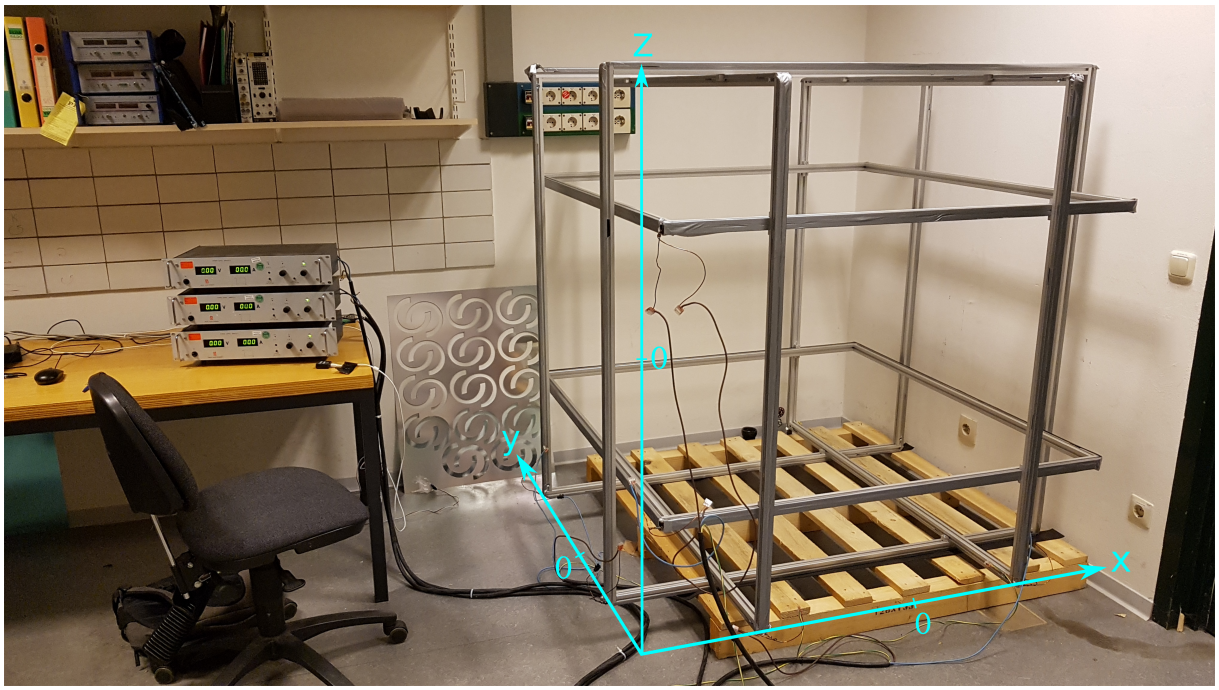

Figure 3.11: Full Helmholtz coil cube.

3.2.2 Operation and calibration

Besides the manual use of the power supplies, they offer the possibility for automation. The output current is set via an analogue input. This was done by using the *Phidget* card *PhidgetAnalog 4-Output ID: 1002_ 0B*.

To monitor temperature changes in the wire and have a fail switch to intervene before any structural damage can occur, the *Phidget* temperature sensor *Precision Temperature Sensor ID: 1124_ 0* [39] was placed at the wires of an edge of a coil. This temperature sensor returns an analogue voltage signal V_{in}, which is read out by *Phidget* card and

transformed into a temperature value[1]. The temperature can be read out regularly to check whether a critical temperature is reached.

To measure the magnetic field, a magnetometer *PhidgetSpatial 3/3/3 ID: 1056_ 0* [40] of the company *Phidgets* is used.

Calibration of the magnetometer

The *Phidget* magnetometer has to be calibrated against the earth field. This is done by using the field at the institute for nuclear physics in Münster[2]. This field is calculated by the magnetic field calculator of the *National centers for environmental information* [30] and yields a magnetic field strength of $|B_{\text{Münster}}| = (49.30 \pm 0.15)\,\mu\text{T}$. $B_{\text{Münster}}$ is subsequently entered in the *Phidget* calibration program [41], which measures the total field strength while the magnetometer gets rotated around until nearly all solid angles are evenly covered as illustrated in figure 3.12.

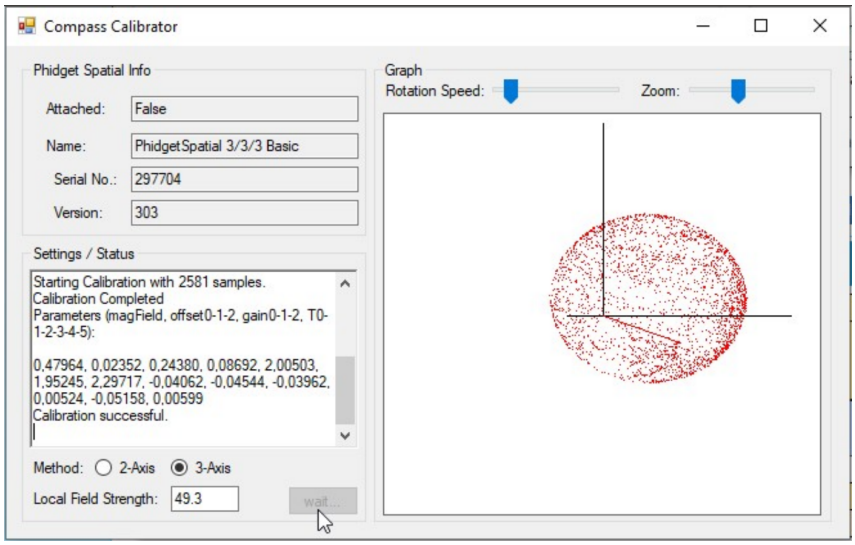

Figure 3.12: Calibration of the magnetometer in the dedicated software of the sensor [41].

To cross check if the calibration is correct, a second magnetometer of the same type was calibrated at the same position and the measured magnetic field of both magnetometers compared. Differences of up to 1 µT were found, which is most likely explained by differences in the orientation of the sensor chip, hardware differences or magnetometer uncertainties, which will be discussed later. The magnetometer uses the Hall effect, which is based on the Lorentz force. When the magnetometers are aligned based on their outer cases, there is no guarantee that the chips inside of the cases are also aligned. Depending on the orientation of the chip shown in figure 3.13 inside the case, the field might be detected differently by the magnetometers.

[1] using $T = 2.2 \cdot V_{\text{in}}$

[2] coordinates: 51° 58' 0" north and 7° 35' 59" east

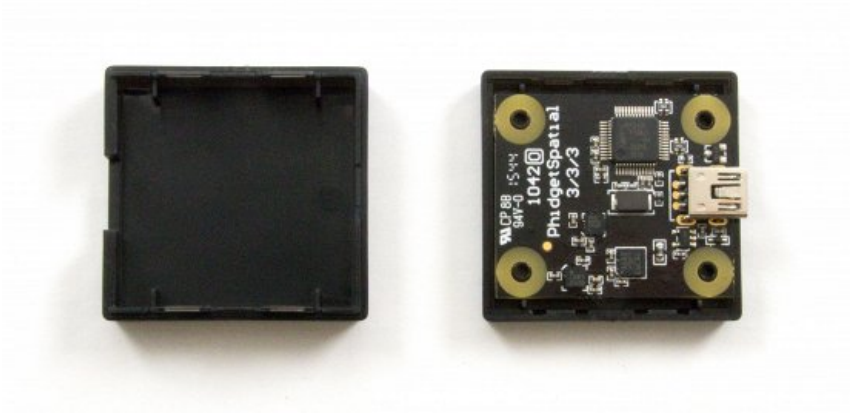

Figure 3.13: Electronics of the magnetometer [40].

The parameters of the magnetometer stated by the *Phidget* manual are a resolution of 0.3 µT, 0.12 µT white noise σ and a drift of 8.7 nT. The resolution is the minimal field change the magnetometer can detect and the minimum drift is a low frequency noise drift, which can be neglected for the short measurements done in this thesis. How the white noise and the resolution are exactly applied to the measurements is not completely known. Magnetic fields measured by the magnetometer are stated with a significance of 0.01 µT far exceeding the stated accuracy. It is possible, that the magnetometer averages the measured field between each data requests, before returning the field.

It has to be considered that the calibration of the magnetometer creates a deviation to the real magnetic field, if the real total field at the place and time of the calibration differs from the 49.30 µT used for the calibration. It has to be assumed that the field inside of a laboratory is not the same as the natural field calculated by the *National centers for environmental information* [30]. Consequentially all fields measured by the magnetometer differ from the real field. To minimize this effect, the calibration was done as far away from any electronic devices and metal as possible in the centre of the laboratory.

3.3 Characterisation of the magnetic field of the setup

Even though, following the analytical calculations, the coils should generate a sufficiently strong and homogeneous magnetic field, some aberrations from the analytical calculations are expected.

- For the theoretical calculations some simplifications, like the ignoring wire extent and their orientation, had to be done 3.1.2.
- As soon as any electronic device, like the magnetometer, which is not shielded, is introduced into the cube, it disturbs the magnetic field and its homogeneity, both, by being made of paramagnetic materials and by inducing a magnetic field due to currents in the device itself.
- Depending on the power supplies, the current might not be as stable as expected, leading to fluctuations and shifts in the field.
- Ideally, the cube should be shielded from exterior fields. This is not necessary, as long as the surrounding fields are homogeneous in time and space. Inhomogeneities in the background field can not be compensated by the coils.
  Changes in the exterior magnetic fields, due to external circumstances, can also change the behaviour of the field over time. For example it has been shown that

simple things, like opening the adjacent metal door of the laboratory, has a huge impact on the field. Additionally, any PCs or cables leading to the coil or the measurement setup generate their own measurable field.

Due to these aberrations, the field has to be characterized and tested as part of the commissioning.

3.3.1 Controlling the magnetic field

The steering voltage applied to a power supply causes an output current into the coil. The function between those parameters was determined by turning up the voltage and reading back the current generated by the power supply. The result is shown in figure 3.14.

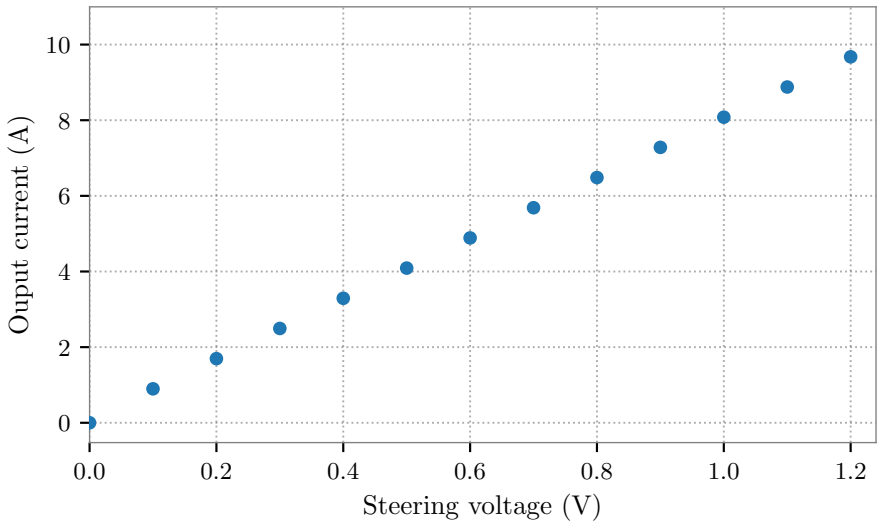

Figure 3.14: Output current of the power supplies as function of the steering voltage.

The output current rises linearly with the input voltage. While the steering voltage was set by a program, the current was read back over the display of the power supply with a resolution of 0.1 A. This was done for all three power supplies yielding identical results.

As shown in equation 2.18 the magnetic field B is expected to rise linearly with the current in the coils, which means a linear behaviour between input voltage and the magnetic field is expected. To verify this and to calculate calibration functions for the coils, B was measured in the centre of the cube while turning up the steering voltage to 1.24 V equalling a current in the coils of about 10 A. Subsequently $\Delta B = B - B_0$, where B_0 is the field without an artificial magnetic field, was calculated, plotted, and a linear fit $y = a \cdot x + b$ applied. This was done for all 3 coils successively and is shown in figures 3.15 to 3.17.

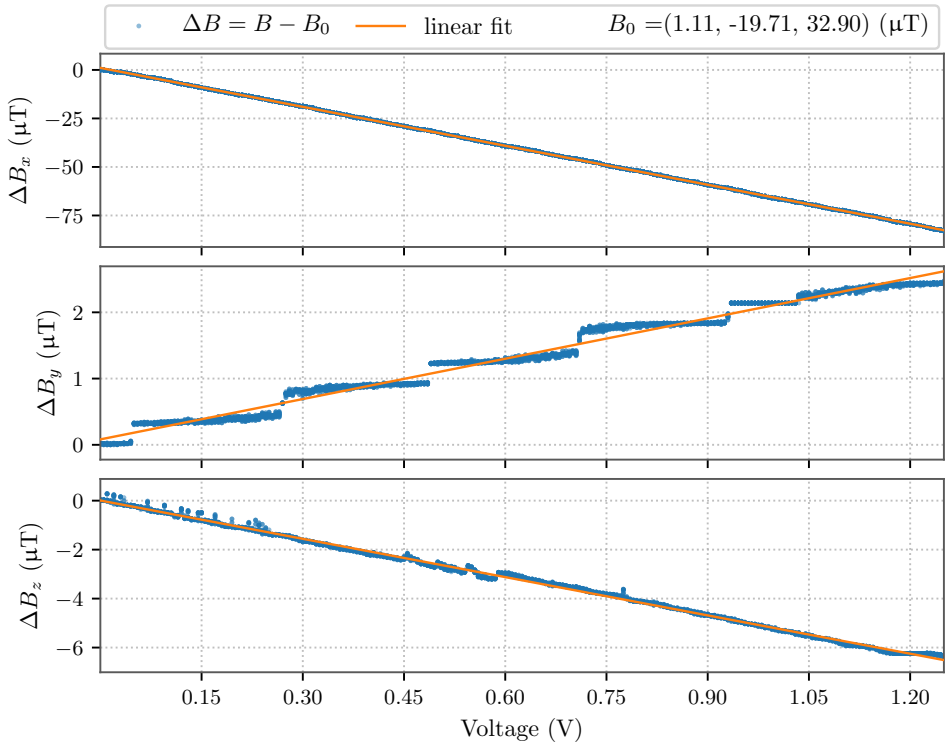

Figure 3.15: Increasing the current of the x-coil while measuring the field in the centre of the cube.

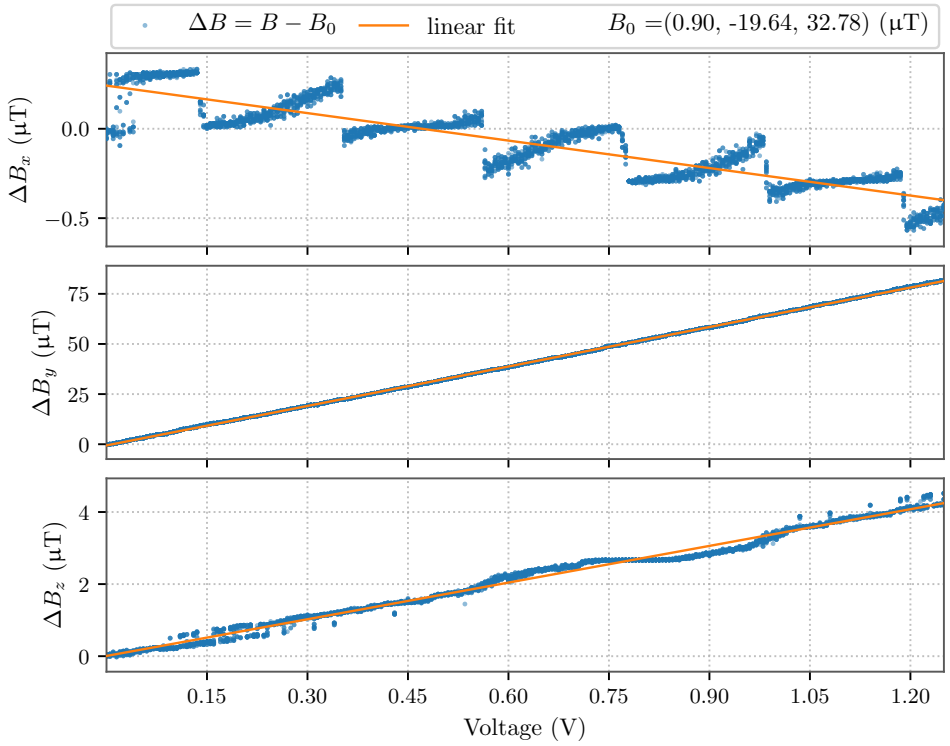

Figure 3.16: Increasing the current of the y-coil while measuring the field in the centre of the cube.

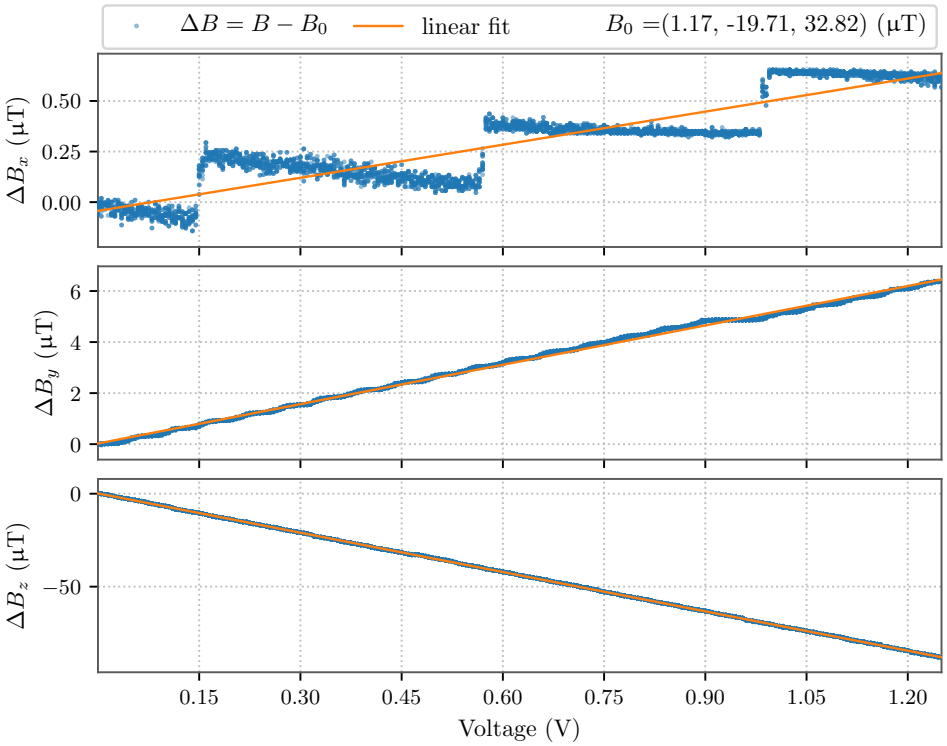

Figure 3.17: Increasing the current of the z-coil while measuring the field in the centre of the cube.

Each coil getting powered up changes the field component aligned with the coil pair axis by more than 80 µT. In theory, each coil set should only influence the corresponding magnetic field component, due to the field between two coils being aligned with their symmetry axis. In practice, on the one hand, the coils are not perfectly perpendicular to each other and on the other hand, the magnetic field sensor is not perfectly aligned with the coil axis. Therefore the other two components of the field show small variations as well. When activating the x-coil, B_y increases by $\approx 2\,\mu T$ and B_z decreases by $\approx 6\,\mu T$. Additionally, there is a step behaviour visible especially for smaller orders of magnitude. These steps cover $\approx 0.3\,\mu T$ and are most likely directly correlated to the resolution of the magnetometers of 0.3 µT and a feature of its hardware structure. This resolution seems to be less prominent for the z-component of the magnetometer, possibly due to hardware differences. The activation of the y- and z-coils yielded similar results in behaviour with changes of $\approx 0.5\,\mu T$ and $\approx 4\,\mu T$ for B_x and B_z for the y-coils and $\approx 0.6\,\mu T$ and $\approx 6\,\mu T$ for B_x and B_y for the z-coils. B_x shows smaller variations than B_y and B_z, possibly due to the x-component of the magnetometer being more precisely aligned with the symmetry axis of the x-coil. Because of the smaller scale, the steps are most visible for B_x and less visible for B_y.

To assure that no error in the magnetometers occurred, both sensors were placed directly on top of each other with the cases aligned but rotated by 90% in the y-x plane. To increase the clarity of the plots, the results of the second magnetometer can be found in appendix A.1 to A.3. It is noticeable that the sensors of the two magnetometers were not orientated equally in the cases as mentioned before. For example, the use of the y-coil seems to also generate a B_z field of up to 4 µT, measured by the first magnetometer and

up to 6 µT measured by the second.

The change of the secondary fields (fields not aligned with the symmetry axis of the coil pair) is much weaker than the change of the main fields but all components follow the expected linear behaviour, except for the step behaviour.

The linear functions fitted to the data were subsequently used as calibration to calculate functions for the necessary input voltage to generate any desired field by running a calibration program, developed in Python. From the 9 dependent functions, a 3 function system can be derived to determine the needed voltage of each power supply. This calibration should be done before the start of each new measurement set, in order to minimise the deviations from the desired field and to lower computation time. The bigger the time gap between calibration and measurement is, the larger the deviations from the calculated functions will be, whether by changes in the environment and background field or by small changes in the setup. In the following, this method will be used to set any wanted field while the magnetic field sensor is used to double check results and adjust the steering voltage accordingly if necessary. A short documentation of the programs used can be found in appendix A.1.2.

3.3.2 Background magnetic field of the Earth

To begin the characterisation of the magnetic field, a long time measurement of the field in the laboratory was done without an artificial B-field. To cross check the performance of the magnetometer, the second magnetometer was placed on top of the first magnetometer again, which verified the results, as illustrated in figure A.4. The magnetic field was taken for 10 minutes every 0.1 seconds. To focus on the deviation over time and increase the comparability, the values of the field B are subtracted by the first value taken B_0. Subsequently, a rebinning was done using the mean value of 100 points to visualise the overall behaviour. The results for the first magnetometer are shown in figure 3.18.

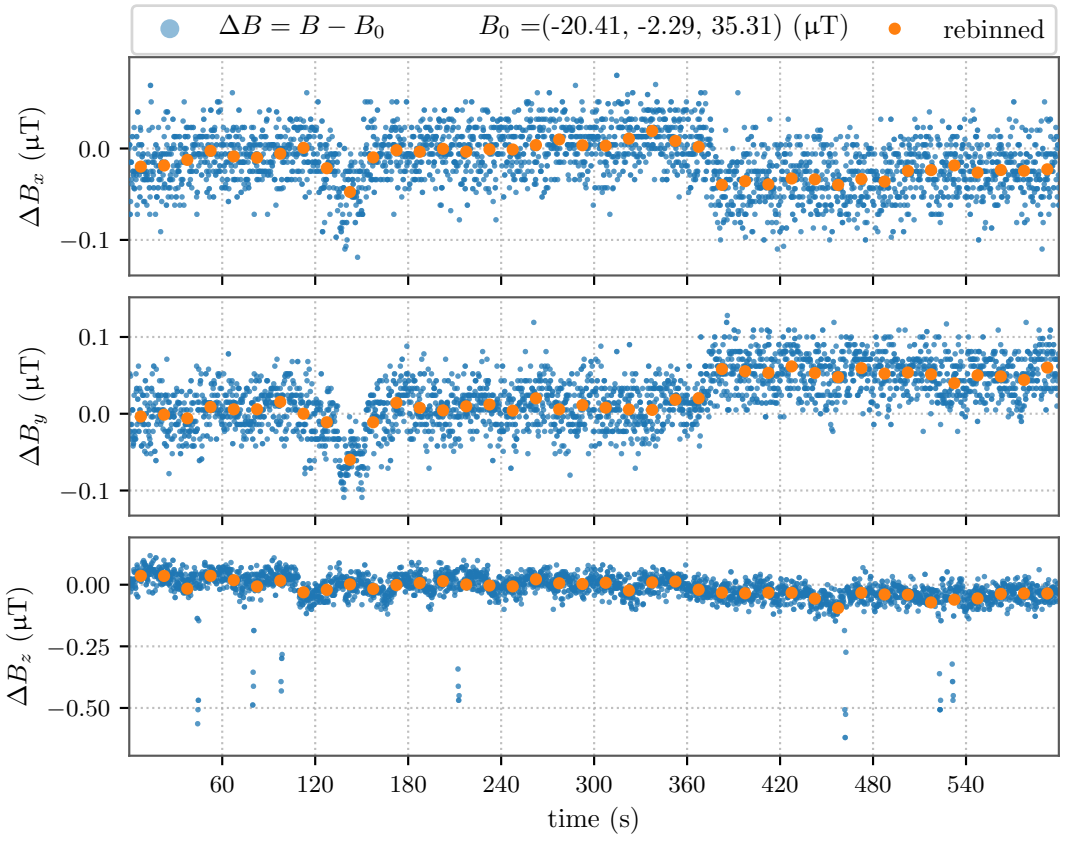

Figure 3.18: Behaviour of the background magnetic field in the laboratory over 10 minutes. Data taken every 0.1 s and additionally rebinned, merging 100 points to one to illustrate the overall behaviour.

While the overall field stayed relatively constant over time, there is a noise fluctuation of $\approx \pm 0.05\,\mu\text{T}$ for B_x and B_y and a few jumps of about $\pm 0.6\,\mu\text{T}$ in B_z. Additionally, there are lines in the data visible for magnetic fields of smaller magnitudes like for B_x. These lines are separated by $0.01\,\mu\text{T}$, corresponding to the smallest digit of the magnetometer output.

3.3.3 Constant artificial magnetic field

To cross check the long time behaviour of the artificial field, a constant current of 5 A was applied on each coil and the two magnetometers placed in the centre of the cube. The results of the measurement of the first magnetometer are plotted in figure 3.19, while the data of the second magnetometer confirms the data of the first magnetometer and is plotted in appendix again A.5.

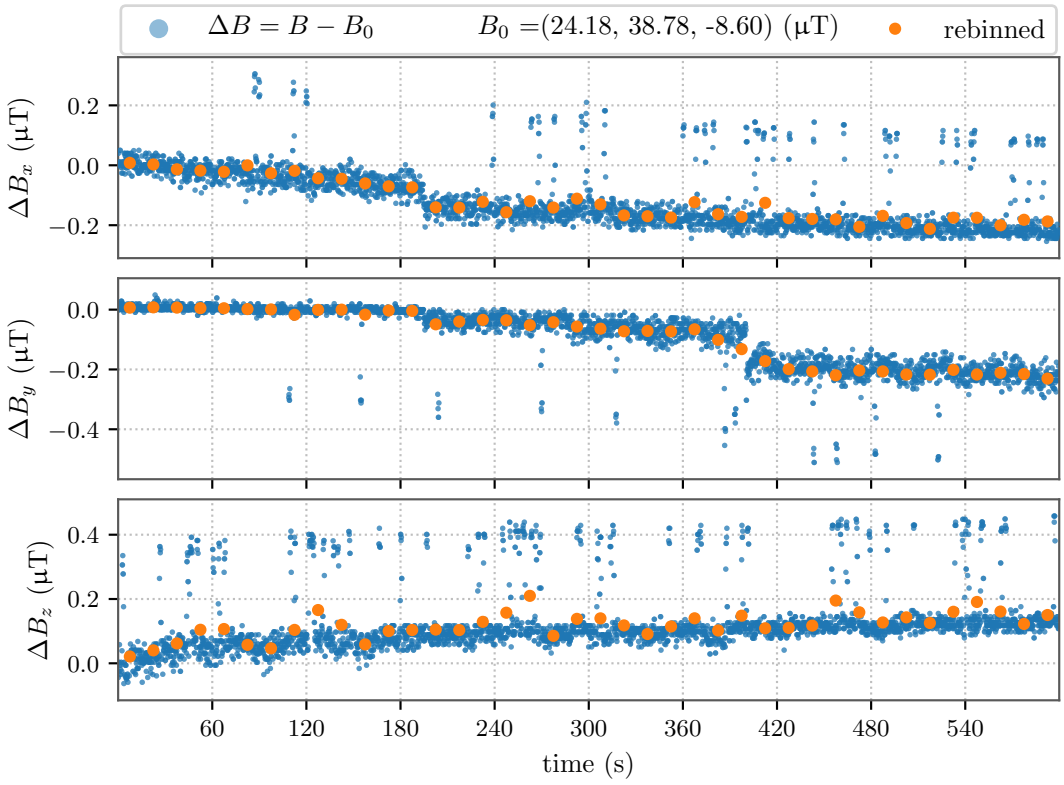

Figure 3.19: Behaviour of the total magnetic field after powering each coil with 5 A and measuring for 10 minutes.

Besides the fluctuations of the white noise, there are jumps of up to approximately 0.3 μT visible for all field components. These were not measured before the coils were activated and are therefore most likely generated by fluctuations in the artificial magnetic field. The jump like behaviour is an effect of the resolution of the magnetometer, whereas the fluctuations themselves could have various origins. Most probably, the current of the power supplies has small fluctuations. Additionally, the field shows a drift, over a time of 10 minutes, of approximately 0.2 μT. This drift was observed in both magnetometers and was reproducible, for measurements done right after the first start of the power supplies and therefore deserves further investigations.

If this drift is not only a feature of the magnetometer, the origin of the shift most likely lies in the warm-up time of the power supplies. This would match the description of the power supplies stating a low uncertainty of the current is only reached after 1 hour of warm-up time [42].

To check whether these results show changes for longer measurements, the setup was left running for 1 hour and the measurement was repeated. The results are plotted in figure 3.20 and in appendix A.6.

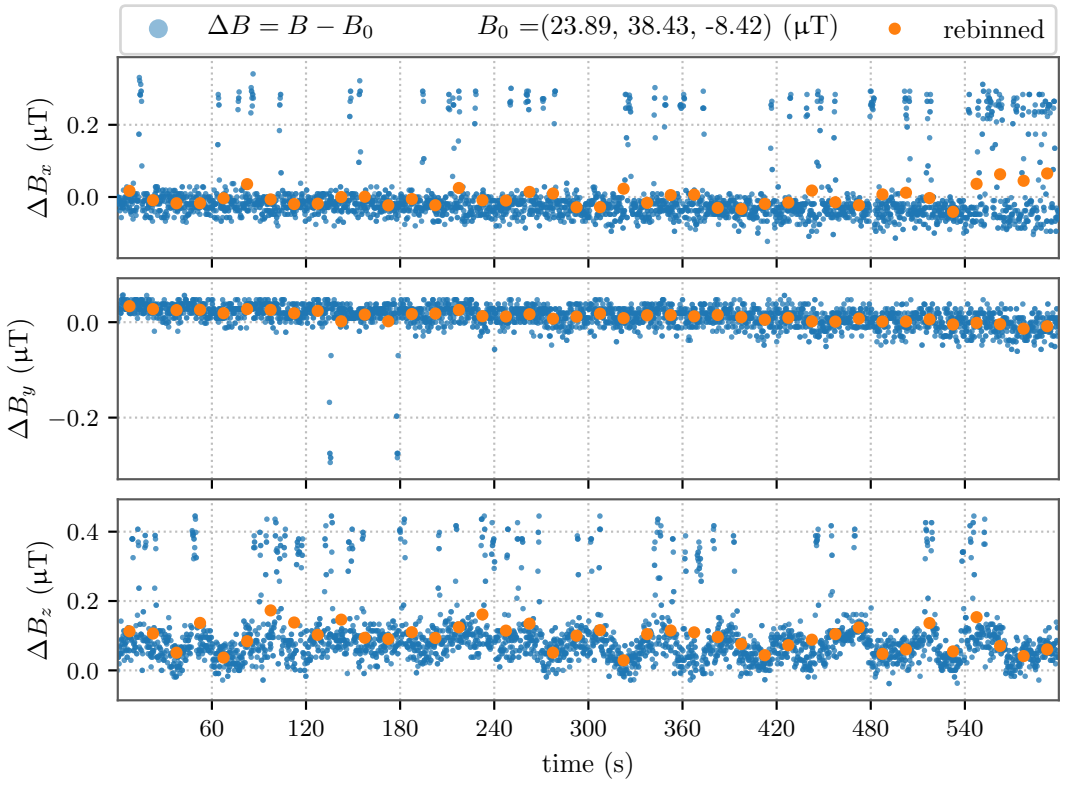

Figure 3.20: Behaviour of the total magnetic field over 10 minutes, after a waiting time of ≈ 1 hour, while applying a current of 5 A over the whole time.

The drift is no longer visible, either due to an equilibrium in heat production and loss in the power supplies or a more stable data taking by the magnetometers.

This behaviour has to be taken into consideration, especially for longer measurements, in order to achieve a constant field when a high precision is necessary. Later measurements done with the PMT are not greatly effected by this behaviour, due to shorter measurement times of less than 2 minutes before adjusting the field. For longer measurements, the steering program can be used regularly to reset the field to the desired strength.

3.3.4 Homogeneity of the field

In theory Helmholtz coils create a very homogeneous fields and the natural field of the Earth changes a lot on global scales but should be close to homogeneous in scales of a few meters. Even if the coils would produce a fully homogeneous field, a non homogeneous background field would corrupt the total homogeneity. Whether this is the case and how homogeneous the artificial field is, will be the focus of the following sections.

The field was taken by measuring 100 data points over 10 seconds and calculating their average. This gives the possibility to calculate a standard deviation σ of those points and to see the fluctuations of the field over 10 seconds and subsequently calculate the standard error $\Delta = \frac{\sigma}{\sqrt{n}}$. Invisible in the standard deviation of these measurements are changes of the field due to changes in the laboratory, lasting longer than 10 seconds. For example, the opening of the metal door next to the cage induced changes in the field of $\approx 0.3\,\mu T$ or slightly moving the power supply cables by accident generated deviations of up to $0.7\,\mu T$. Other aberration sources could not be directly determined but are most

likely due to external fields generated by the power lines in the walls and electric devices in the adjacent rooms. The Standard errors are therefore very small and have only a limited informative value.

These measurements were redone a few times to show that they are reproducible and crosschecked with the data of the second magnetometer, which agreed within in discussed uncertainties. The measurements done to show the reproducibility showed small variations of $< 0.5\,\mu\mathrm{T}$, possibly due to the reasons mentioned in the beginning of section 3.3.4 and the time difference between measurements.

Homogeneity of the background magnetic field

First, the homogeneity of the background field in the laboratory was investigated. The coil cube stood in a corner of a laboratory on ground level, as shown in figure 3.11. To quantify the homogeneity, a platform with both magnetometers mounted on top of each other was moved vertically and horizontally along the axes of each coil set, without any artificial field. Starting from the centre of the cube, 20 cm were measured in 1 cm steps. Due to the symmetry of the setup, only one direction was measured. This was done for all three axis of the cube and all three field components measured each time. The resulting field for each point B_{bg} was subtracted by the field in the centre of the coil $B_{\mathrm{bg},0} \approx (-20, -3, 35)\,\mu\mathrm{T}$ and the absolute value taken to simplify comparisons of the fields. To calculate the uncertainty of these measurements, the standard error was used in a quadratic error propagation $\Delta B_{\mathrm{bg}} = \sqrt{\Delta B_{\mathrm{bg}}^2 + \Delta B_{\mathrm{bg},0}^2}$.

Homogeneity of the total field

To quantify the homogeneity of the total field B_{total}, a current of 5 A was applied to each coil and the measurement was redone. Each axis scan with an applied artificial field was done right after the measurement of the same axis without artificial field. Again, the uncertainty was calculated by using the standard error of the 100 measurements of each step and then used in a quadratic error propagation $\Delta B_{\mathrm{total}} = \sqrt{\Delta B_{\mathrm{total}}^2 + \Delta B_{\mathrm{total},0}^2}$.

Homogeneity of the artificial field

The homogeneity of the artificial field B itself can be be investigated by subtracting the background field from the total field, leading to a new uncertainty of
$\Delta B = \sqrt{\Delta B_{\mathrm{total}}^2 + B_{\mathrm{bg}}}$.

The results for the background, the total and the artificial field are plotted in figure 3.21.

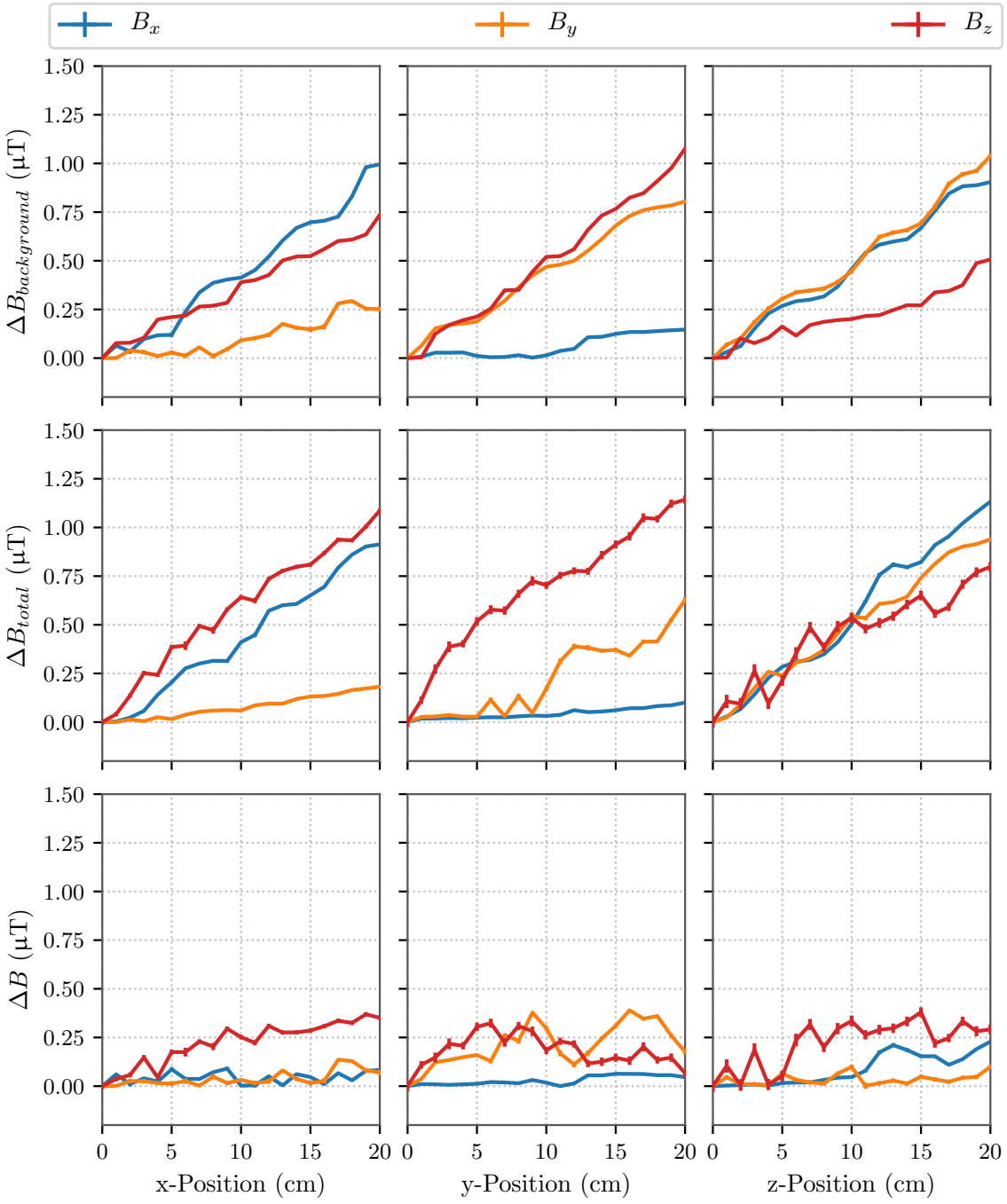

Figure 3.21: Measurements of the magnetic field while moving the magnetometer 20 cm in 1 cm steps subsequently along all axes. **Top row:** With no artificial field applied. **Middle row:** With applied artificial field. **Bottom row:** Effective artificial field. **First column:** Scan of the x-axis. **Second column:** Scan of the y-axis. **Third column:** Scan of the z-axis.

The background field B_{bg} varies by up to approximately 1.1 µT and behaves slightly differently in all directions. On each axis, one of the components increased less than the others: For the x-axis scan B_y increases only by 0.25 µT, on the y axis the same happens to the B_x component and on the z-axis B_z shows the smallest change with 0.5 µT.

The previously invisible uncertainty of B_z rises for the measurements of the total field

B_{total}. This increase of the noise with an applied artificial field could already be seen in the previous measurements in section 3.3.3 and most likely originates from small fluctuations in the artificial field. The homogeneity of the total magnetic field field B_{total} is dominated by the homogeneity of the background field and behaves very similar to it.

The homogeneity of the artificial field B is given by the deviation of the total field subtracted by the deviation of the background field $B = B_{\text{total}} - B_{\text{bg}}$ and does not exceed $0.5\,\mu\text{T}$.

To put this value in relation to the calculated homogeneity of section 3.1.2, the deviation of the field was calculated in percentage of the artificial field strength by using:

$$B_{\text{relative}} = \frac{\Delta B}{B_{\text{total},0} - B_{\text{bg},0}} \tag{3.6}$$

Additionally, the calculated curves of figure 3.5 were transferred to the plot for direct comparison, as shown in 3.22.

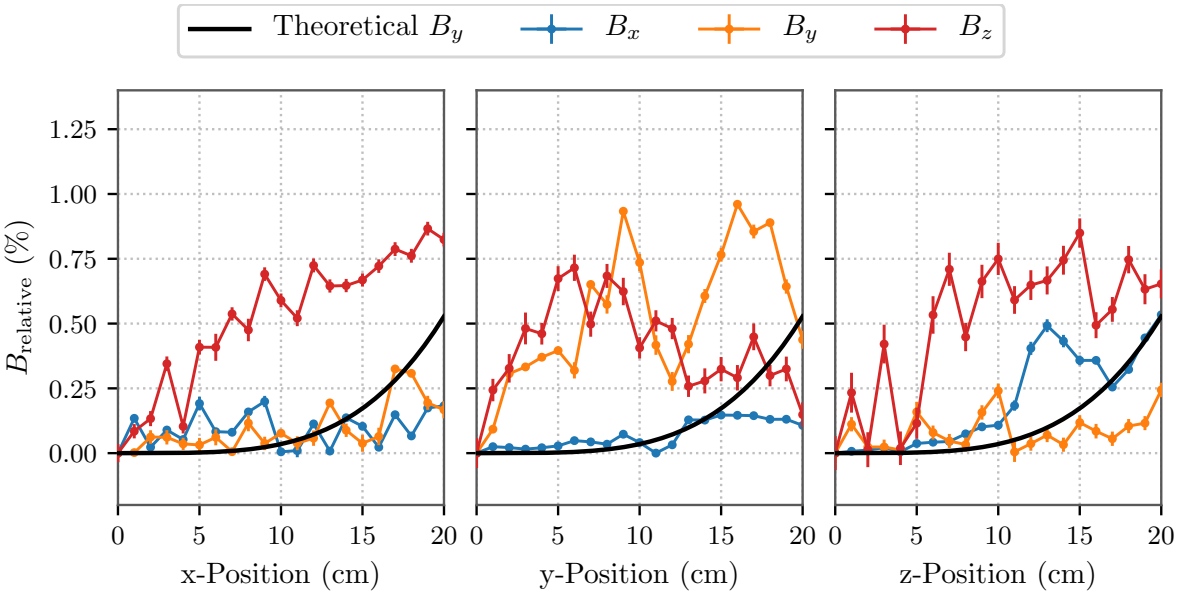

Figure 3.22: Deviation of the magnetic field from the field in the centre of the coils, depending on the distance to the centre along the 3 cube axes of the cube, with comparison to the theoretical deviation of B_y. **Left:** Scan of the x-axis. **Middle:** Scan of the y-axis. **Right:** Scan of the z-axis.

The homogeneity of the artificial field does not match the theoretical curves but does not show a great deviations either. The total homogeneity of the field is not as good as calculated theoretically, especially close to the center of the coils. However, it does not exceed 1 % deviation over 20 cm, which was one quality benchmark in the setup planing. The higher deviations during the first few cm distance from the centre can be explained by several additional error sources, beside the 1-σ standard deviation, which have to be taken into consideration:

- The field was expected to be less homogeneous, due to deviations in the realistic setup compared to the theoretical calculations, compare section 3.3.

- One measurement takes approximately 10 minutes. The corresponding second measurement is performed subsequently with a gap of approximately 5 minutes. During this time, a change in the background field cannot be ruled out.
- The time needed to measure one step takes 10 s. Errors, as discussed in section 3.3.4, are not represented in the standard deviation.
- The magnetic field might show a drift in strength, depending on the time passed due the activation of the power supplies, as discussed in section 3.3.3.
- Last but not least, the magnetometer has shown jumps of 0.3 µT and the orientation of the sensor chip might not be perfectly aligned with the axes of the cube.

These errors are not taken into account here and are most likely the reason for the shape and amplitude of the homogeneity of the field differing from the theoretical curve. Nevertheless, the artificial field is as close to homogeneous as expected and plays a minor role, compared to the homogeneity of the total field and the uncertainties of the set field B_0 in the centre of the cube.

The data talking process of the magnetometer and with it the origin of its uncertainties, could not be determined its fullness as discussed in the beginning of this section. However, the effects in question have a order of magnitude of about 0.3 µT, which was expected as the magnetometer resolution in the first place. Additionally the further field uncertainties coming from the homogeneity and the fluctuations in the background field were already shown to be just as high if not higher.

4 Influence of the magnetic field on a PMT of the mDOM

With the strength and homogeneity of the field sufficient enough, a first characterisation of a mDOM PMT, the Hamamatsu R12119-02, was done, starting with the reproduction of the results of Lukas Kuballa of section 2.5.2 and doing a full 4π field scan of the gain and transit time parameters with the strength of the magnetic field at the South Pole. To set the magnetic field to the desired strength, the Python program documented in A.1.3 was used.

4.1 Experimental setup

A dark box (light shielded box) is placed roughly in the centre of the cube. This box is painted back from the inside, has a cable maze to suppress light from the cable feed-trough and is tightly closed to prevent any light from entering. Inside of the box, the PMT is placed in the centre of the coils on an adjustable metal stand. Right next to the PMT in $\approx 3\,\text{cm}$ distance on the same height is the magnetometer placed. On the opposite side of the box, a light transmission fibre directs light of a LED[1] at a diffuser, which is pointed at the front of the PMT. Outside of the box is a pulse generator[2], used to create trigger signals for the LED driver[3] and an oscilloscope[4], which is connected to the PMT. The base of the PMT is supplied with negative high voltage by a HV-generator[5] outside of the box. The resulting charge of each trigger pulse gathered by the oscilloscope is sent to a PC for evaluation. The whole setup is illustrated in figure 4.1.

When the measurement is started, the PC activates the pulse generator. This generator generates two signals, one is sent to the LED-driver while the other one is sent to the oscilloscope. The signals are rectangular pulse, with a length of 30 ns and are generated with a frequency of 10 kHz. When the LED-driver gets the trigger signal, it sends a signal to the LED, starting its light emission. The generated light follows the optical fibre to the diffuser and is spread across the box evenly onto the PMT. Simultaneously, the second signal activates the measurement process in the oscilloscope, starting the read out of the PMT. The charges measured by the PMT are sent back to the oscilloscope, which reports its results to the computer.

[1] LED PLS-8-2-719
[2] Rigol LXI DG1032Z
[3] PicoQuant PDL 800-B
[4] PicoScope 6404C
[5] Iseg NHQ 224M

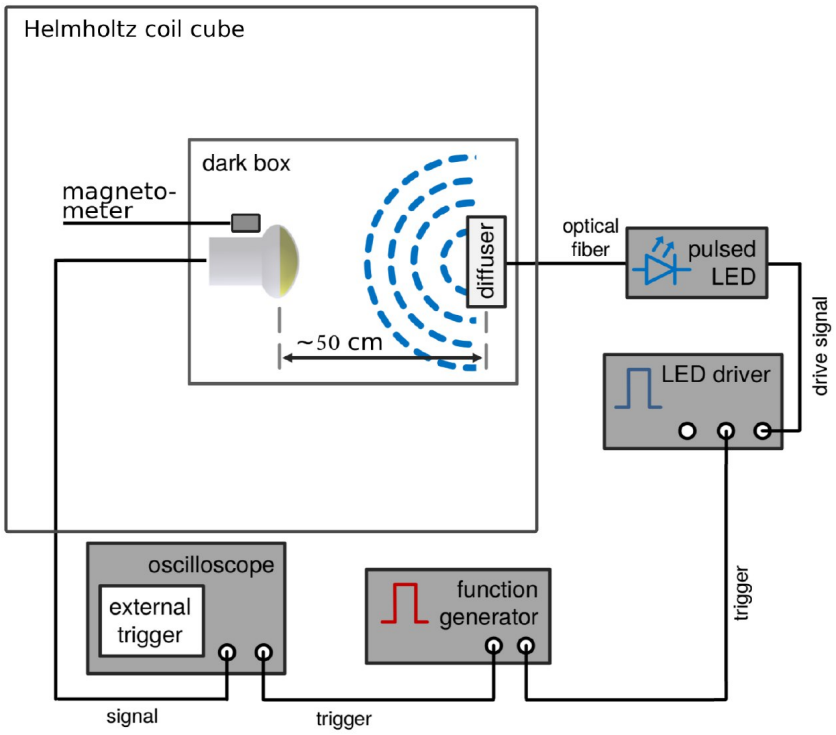

Figure 4.1: Schematic of the used setup. Taken from [10] and modified.

4.2 Measurement types

In this thesis, the effect of the magnetic field on the properties of the transit time and gain of the PMT will be investigated, continuing Lukas Kuballas work [36]. As mentioned in the theory in section 2.3.2 and shown in 2.5.2, both are expected to be influenced by the orientation of the magnetic field.

4.2.1 Gain measurement

To determine the gain of the PMT, about 100000 pulses, were measured by the oscilloscope. These signals were evaluated regarding different properties, like the charge of the resulting signal integrated over the sampling time, as explained in section 2.3.3. The results, plotted into histograms similar to the example of figure 4.2, were fitted by equation 2.14 and the gain calculated using equation 2.7.

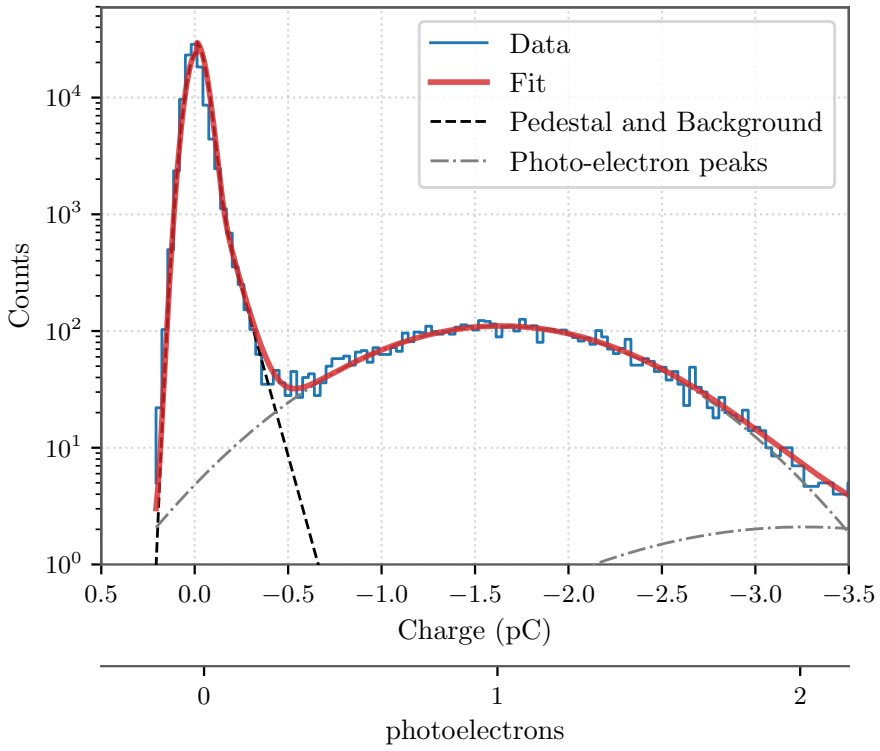

Figure 4.2: Logarithmic charge histogram with the pedestal and the first phe peak visible.

4.2.2 Transit time parameters

The data of the signals used for the gain also holds time information, which are evaluated when determining the transit time and its properties. Time differences between the start of the LED and the position of every pulse were taken and the resulting times were subsequently plotted into a histogram, forming a near Gaussian curve, as expected from section 2.3.2. Additionally, there was an amplitude filter applied to the signal. Each signal under a set limit gets thrown out of the data set, effectively cutting out the background, as visible in figure 4.3.

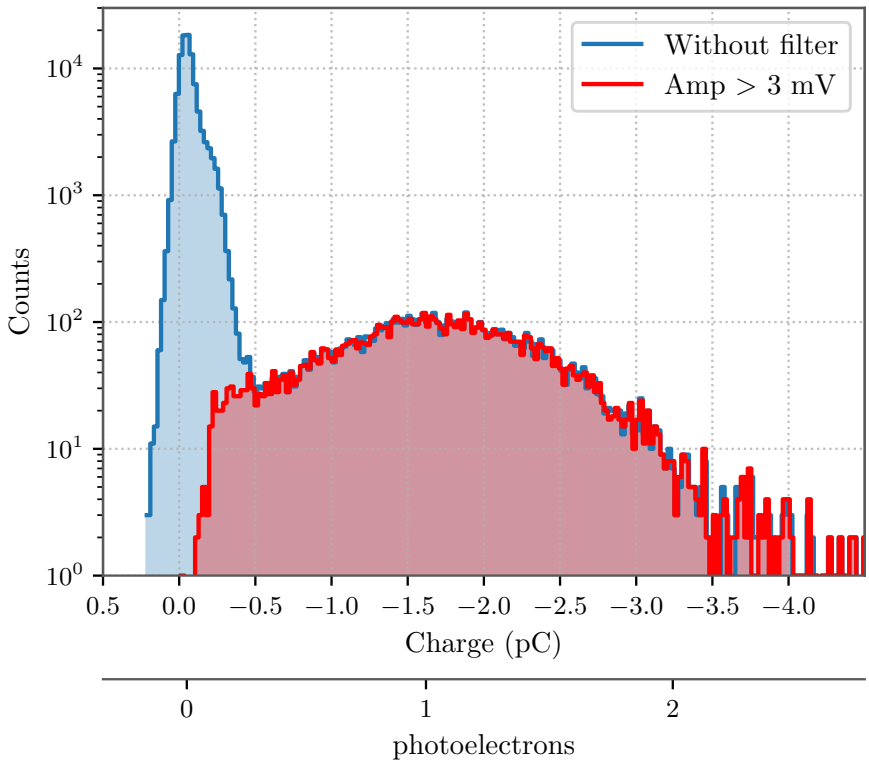

Figure 4.3: Plot of the charge histogram with and without amplitude filter.

By cutting out the background forming the pedestal, the signal to noise ratio of the peak increases in the transit time histogram.

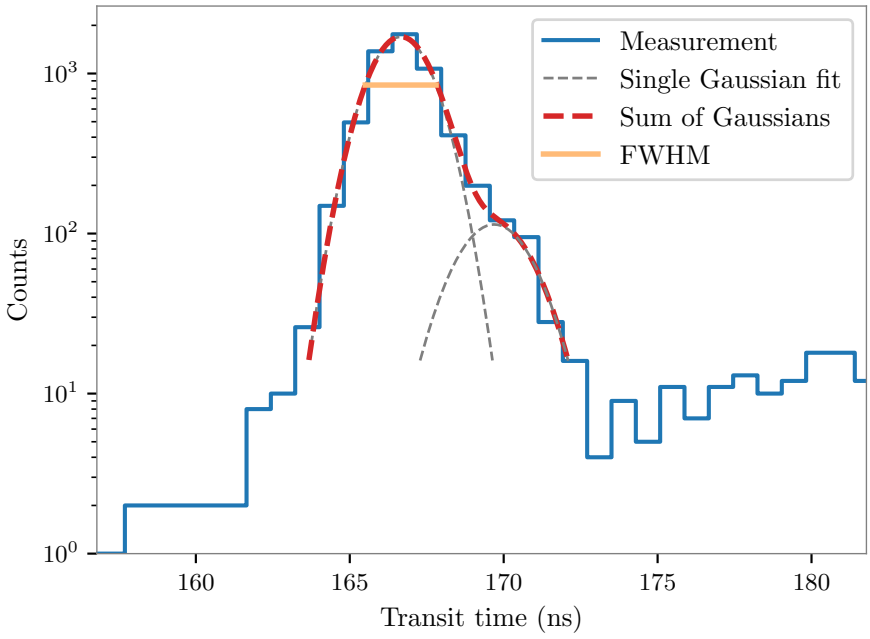

Figure 4.4: Transit time distribution fitted by two Gaussians.

Besides the main peak at roughly 166 ns, there is a smaller peak about 3 ns later with an amplitude of a factor 10 smaller, as shown in figure 4.4. This peak is the result of the inhomogeneity of the electric field between the photocathode and the first dynode, resulting in photons, which hit the outer rim of the photocathode, to arrive slightly delayed [43].

To determine the properties of the main peak, a combined fit of two Gaussians was used to take the slightly delayed pulses into account. The resulting parameters of the main Gaussian were used to determine the mean transit time and also the transit time spread (TTS). The TTS is defined as the full width at half maximum (FWHM) of the Gaussian. Using the standard deviation of the Gaussian σ_{Gauss}, the TTS can be calculated by

$$\text{TTS} = 2 \cdot \sqrt{2 \cdot \ln 2} \cdot \sigma_{\text{Gauss}}. \tag{4.1}$$

4.3 Measurement results

Using the methods described before, the transit time and the gain behaviour, depending on the strength of the magnetic field, were measured. In the following section, the results of Lukas Kuballa will be reproduced first. Afterwards, a full scan of the effect of the magnetic field, depending on the orientation, will be done and the influence of the strength of the field investigated.

The magnetic field strength is set by the programs in appendix A.1.3 and is adjusted until the total deviation between desired field and the strength measured by the magnetometer is less than 0.5 µT. Together with the inhomogeneity of the field for a distance of less than 5 cm to the magnetometer and the uncertainty of the magnetometer discussed in sections 3.3.4 and 3.2.2, the total uncertainty of the strength of the field is estimated to be $\sim 1\,\mu\text{T}$. This uncertainty is applicable to all stated magnetic field strength values.

4.3.1 Reproducibility of previous magnetic field measurements of the PMT of the mDOM

To check whether Lukas Kuballas results are reproducible, his setup had to be transferred onto the Helmholtz coils. As stated in section 2.5.2, the strength of the field had a vertical component of $(43.9 \pm 1.3)\,\mu\text{T}$ and a horizontal component of $(18.4 \pm 0.7)\,\mu\text{T}$.

The PMT was placed with the first dynode bent upwards and the symmetry axis aligned with the x-axis of the cube. The artificial field was adjusted to match the field of Lukas Kuballas measurements. 0° rotation was defined as the field being aligned with the rotational axis of the PMT. Subsequently, the artificial field was rotated using a spherical coordinates in steps of 5°

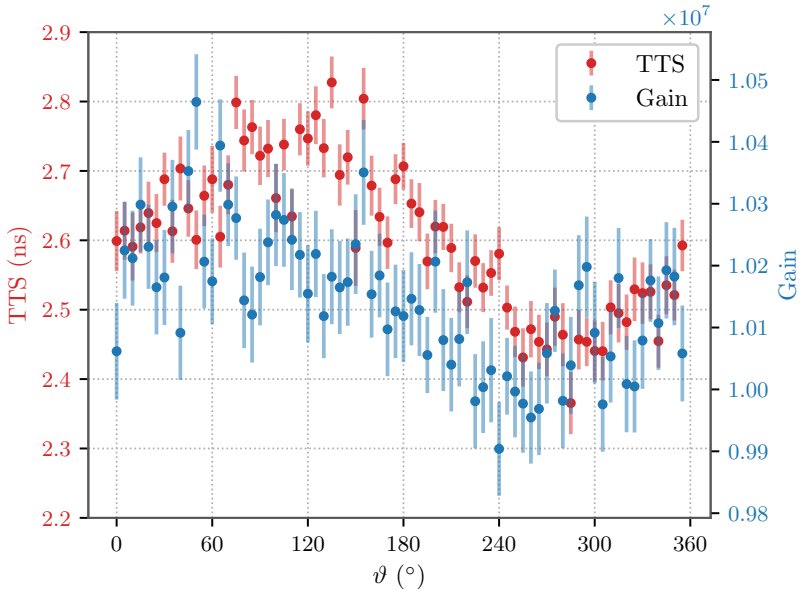

Figure 4.5: TTS and gain for the rotation of the magnetic field in the horizontal plane.

The resulting plot 4.5 shows a behaviour very similar to the behaviour found by Lukas Kuballa, shown in figure 2.25. The TTS rises and falls, following a form best described by a sinus and only differs in accuracy and amplitude. While the total gain used in this thesis was set to $1 \cdot 10^7$, using a high voltage of 1350 V, a total gain of $\approx 1 \cdot 10^6$ was used before in [36]. As discussed in section 2.3.2 a higher gain increases the signal to noise ratio.

The total deviation due to the magnetic field is approximately $\pm 9\,\%$ for the TTS and about $\pm 3\,\%$ for the gain. Comparing this to Lukas Kuballas results of $\approx \pm 3\,\%$ for the TTS shows that the deviation is stronger, probably due to the difference in total gain and high voltage. The behaviour of the gain is harder to compare. The data, with the first dynode bent upwards illustrated in 2.25, is showing fluctuations with no visible behaviour. A comparison to the first results presented in 2.23, where the orientation of the first dynode was not taken into account, shows that the data also seems to follow a sinus, even though inverted, probably due to the different first dynode orientation.

4.3.2 Gain and transit time dependence on the magnetic field direction

Next, the influence of the magnetic field at the South Pole was tested but this time, a full scan was made. Full scan means rotating the field of the coils in a way that the full $4\,\pi$ of all possible orientations is covered. To do this a sphere was diverted into 192 sections of equally sized areas with ϑ and φ in spherical coordinates to scan through a full sphere. The strength of the rotated field was set to $54.7\,\mu\mathrm{T}$, according to the strength of the field at IceCube. The coordinate system used is illustrated in figure 4.6. $\vartheta = \phi = 0°$ corresponds to the field pointing along the x-axis, $\vartheta = 0°$ and $\varphi = 90°$ corresponds to the field pointing along the y-axis and $\vartheta = 90°$ corresponds to the field pointing along the z-axis, analogue to a spherical coordinates transformation. The PMT was aligned with the x-axis/$\vartheta = \varphi = 0°$ and rotated until the first dynode was bent upwards.

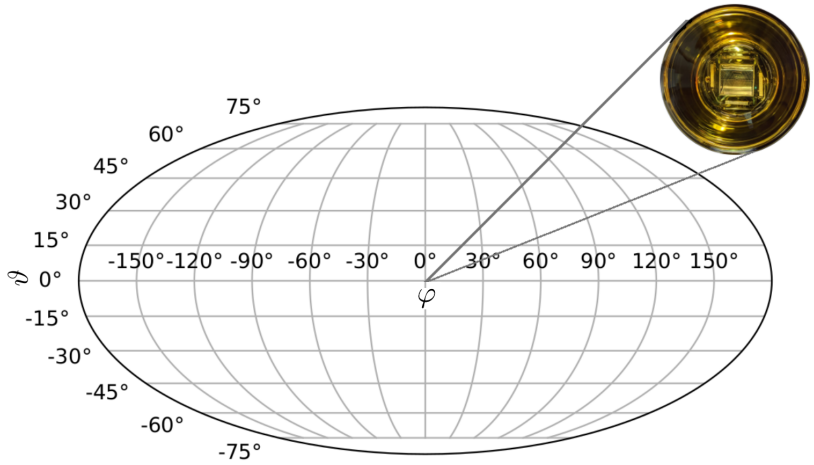

Figure 4.6: Coordinates of the *healpy*-plots shown in this section. The field is orientated along the PMT axis and at $\vartheta = \varphi = 0°$, pointing directly into the inner side of the photocathode. The first dynode is bend upwards.

In the following the transit time and TTS of both, the main and the secondary peak, as well as the gain will be evaluated.

Transit time

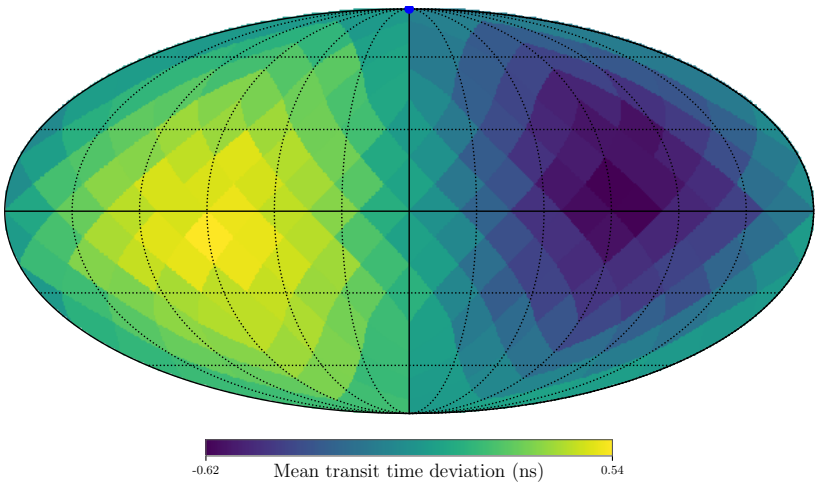

Figure 4.7: The deviation of the mean transit time for different magnetic field orientations.

In figure 4.7, the transit time deviation of the main peak time is plotted. As expected, the transit time varies with the magnetic field, due to the Lorentz force affecting the mean path length of the electrons and varies by about -0.62 ns and 0.54 ns. Two clear poles are formed at the position, where the field is vertically orientated to the PMT axis and perpendicular to the bending directions of the dynodes.

Transit time spread

The widths of the peaks, the TTS, were also computed and are illustrated in figure 4.8.

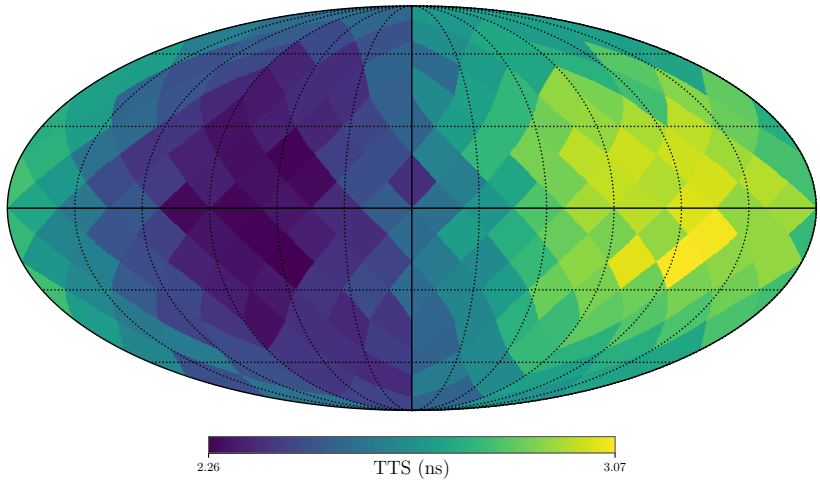

Figure 4.8: The TTS of the main peak for different magnetic field orientations.

The TTS shows the same dipole behaviour as the transit time but decreases with the increase of the transit time itself. Again, this change in the TTS is explained by the Lorentz force, which will affect different paths of the electrons differently and might sharpen or widen the signal peak ranging from 2.26 ns to 3.07 ns. The rotation of the field along the φ-axis while leaving $\vartheta = 0$ crosses the centre parts of the dipole, leading to the sinus form of figure 4.5

Secondary transit time peak

The secondary peak shows a varying height compared to the main peak. As mentioned before, the main reason for the peak is the inhomogeneous electric field of the photocathode. How many electrons are emitted in these zones should be mostly depend on the number of photons hitting the areas in question. Due to photons not being affected by the magnetic field, no clear correlation was expected to be found and was confirmed, as seen in figure 4.9.

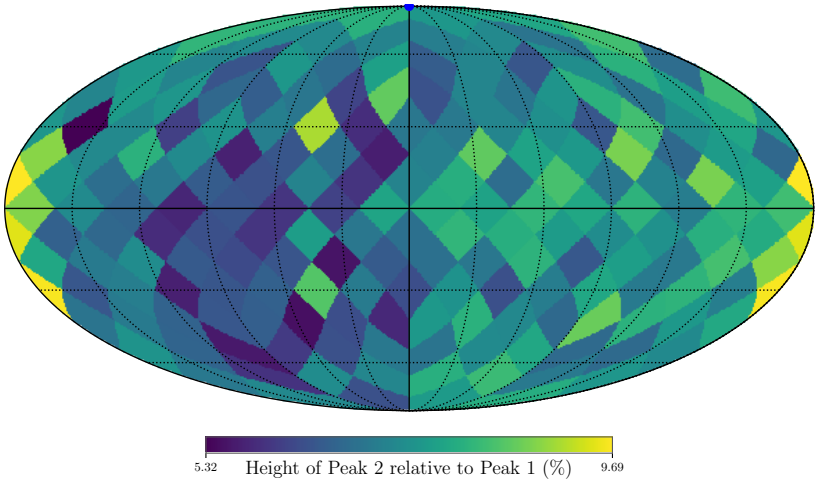

Figure 4.9: The height of the second peak, relative to the main peak, for different magnetic field orientations.

The width of the secondary peak is expected to be influenced by the magnetic field in the same way the width of the mean peak was influenced. As shown in figure 4.10, the TTS lies between 2.03 and 5.23 ns but the dipole behaviour is barely visible.

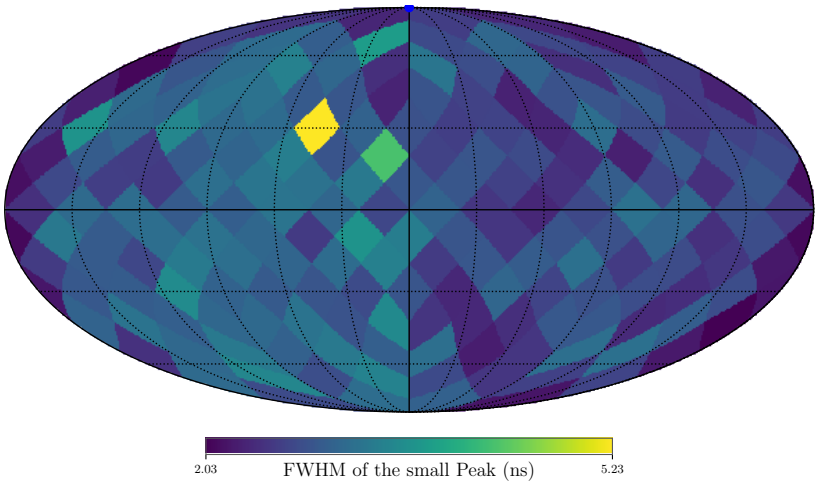

Figure 4.10: The transit time for the second peak for different magnetic field orientations.

Most likely, the background plays a higher role for the secondary peak and fit errors are more likely to occur. A slight dipole can be observed, comparing the left and right halves of the plot.

The time difference of the secondary Peak compared to the first shows the already known dipole behaviour 4.11

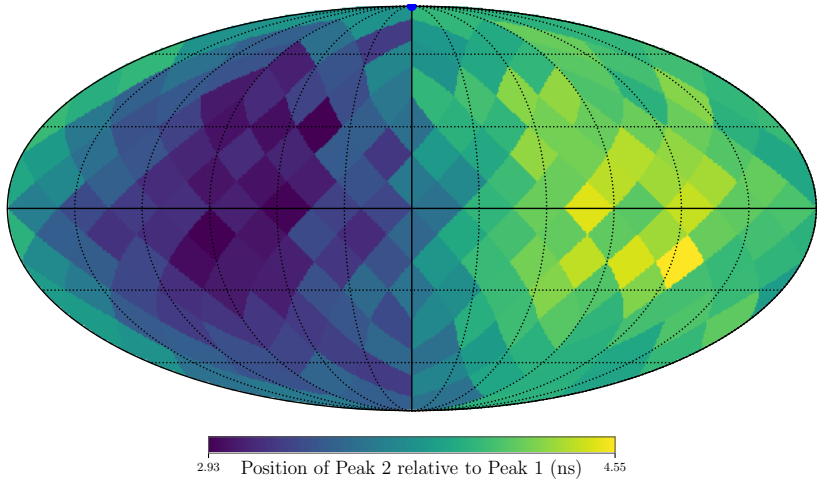

Figure 4.11: The relative time difference of the second peak to the main peak for different magnetic field orientations.

Electrons emitted in the outer rim of the photocathode and thus in the inhomogeneity areas of the electric field, show a varying transit time difference from 2.93 ns to 4.55 ns to the main peak.

Gain

Additionally, the gain was investigated and is plotted in figure 4.12. The dipoles discovered before can be found again, even though less distinct and slightly shifted. The gain deviation varies between -9% and $5\,\%$ and is affected by the magnetic field, due to electron losses during the cascade process, when electrons hit surfaces other than the anodes.

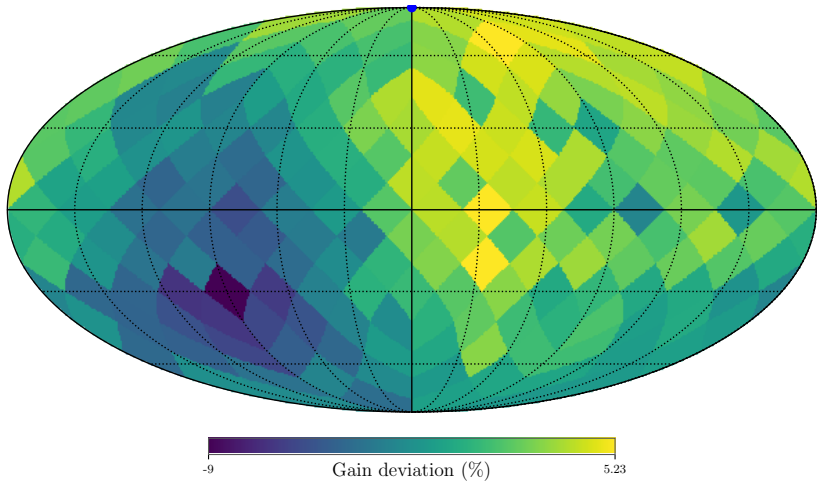

Figure 4.12: Gain of the PMT for different magnetic field orientations.

4.3.3 Influence of the field strength on the gain and TTS

At last, a short test of how the strength of the field effects the TTS and gain was done. To do this, the orientation of the field was set to the turning point of the poles ($\vartheta = 0°$, $\varphi = 90°$) corresponding to the y-axis (see figure 4.6) and the strength was increased from -52 µT (minima of the pole/sinus) to 52 µT (maxima of the pole/sinus).

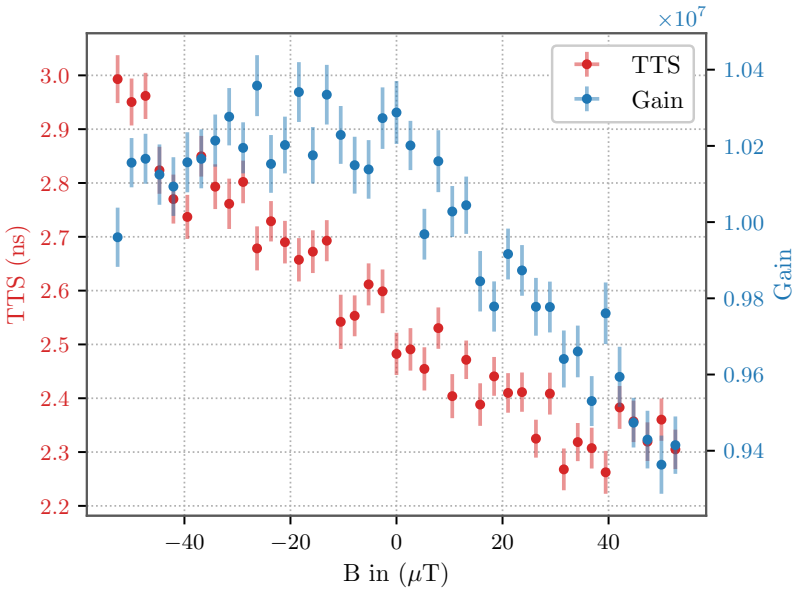

Figure 4.13: Measurement of the total gain and TTS with an increasing B-field, perpendicular to both: The bending direction of the first anode and the symmetry axis of the PMT.

As shown in figure 4.13, the gain and TTS decreases with an increasing field strength. While the TTS decreases almost linearly, the gain rises at first before it starts to decrease. This behaviour of the gain can also be found by comparing figure 4.12 with 4.8 The poles of the gain are slightly shifted to the poles of the TTS. Therefore it is expected that the field orientation resulting in the maximal gain does not match the field orientation resulting in the highest TTS. Additionally, the gain can maximally rise to $g = g_{\max}$ as discussed in section 2.3.2. Therefore it can be expected, that the gain does not exceed a certain level in difference to the TTS.

4.3.4 Discussion of the measurements

The physics background of the changes in transition time, TTS and gain due to the Lorentz force, is the fairly simple and was introduced in section 2.3.4. Nevertheless, due to the complexity of the dynode system and the amount of different scenarios, of electrons being emitted at various positions and getting deflected by different magnetic fields, a full quantitative explanation of parameter changes can not be given in the scope of this thesis. To still look into the origin of the changes of the parameters a short analysis is given in this section.

To simplify this analysis, only the most basic cases will be taken into account and only the influence of the Lorentz force on the first photoelectron will be discussed. In this considerations, a photoelectron is emitted at the centre of the photocathode, gets

accelerated towards the first dynode in a straight line, as shown in figure 4.14, and is only deflected by the magnetic field resulting in different hit positions and path lengths.

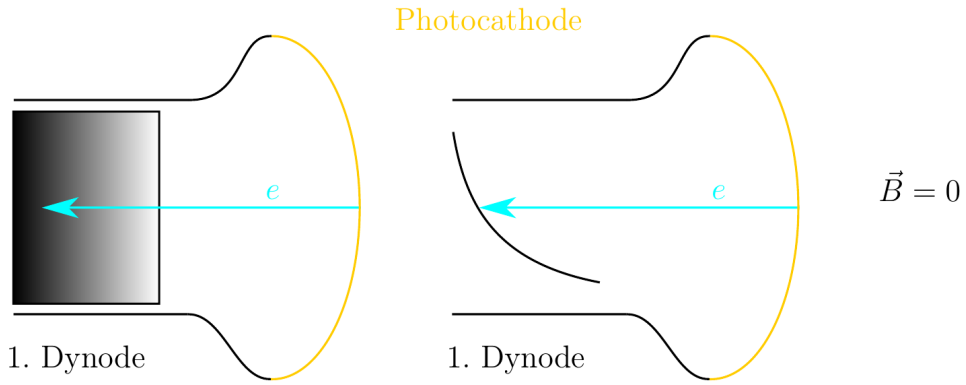

Figure 4.14: Simplified schematic of an electron travelling in a straight line towards the first dynode with no magnetic field. **Left:** Front view of the first dynode. **Right:** Side view of the first dynode

The magnetic field can be divided into six different orientations relative to the first dynode. In correlation to the previous measurement, this 6 cases are the magnetic fields pointing along the axis of the coordinate system in positive and negative direction, where the PMT was orientated along the x-axis of the setup with the first dynode bent upwards.

Magnetic field perpendicular to the symmetry axis of the PMT

Cases 1 to 4 can be divided into two different groups, which are illustrated in figure 4.15.

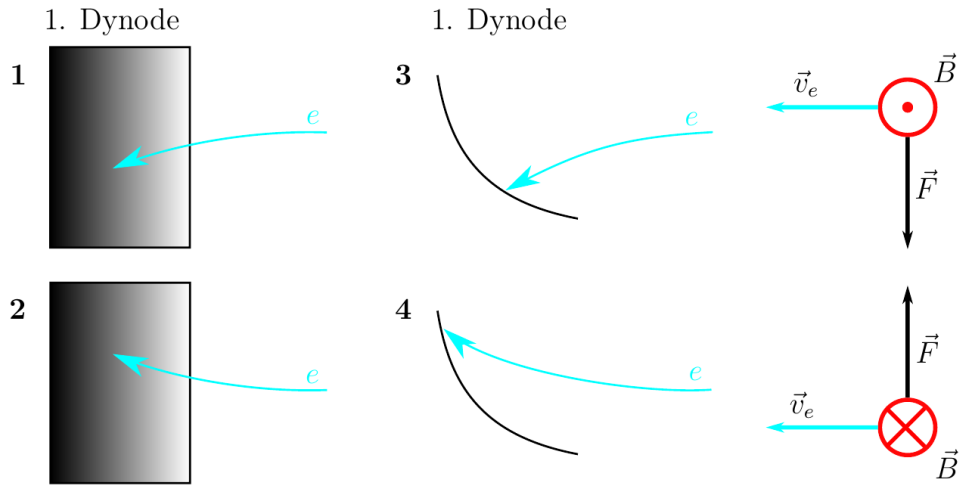

Figure 4.15: Simplified schematic of the an electron travelling towards the first dynode, while being deflected by a magnetic field. **First row, cases 1 and 3:** magnetic field orientated into the plane. **Second row, cases 2 and 4:** magnetic field orientated out of the plane. **First column, cases 1 and 2**: Magnetic field orientated along the bending direction of the first dynode. **Second Column, cases 3 and 4:** Magnetic field orientated perpendicular to the bending direction of the first dynode.

In case 1 and 2 the magnetic field is orientated along the bending direction of the first dynode, in case 3 and 4 the field is perpendicular to the bending direction of the first

dynode. The resulting Lorentz force is perpendicular to both, the magnetic field and the direction of the electrons movement. Case 1 ($B = B_z$) and 2 ($B = -B_z$) create the same path deviation but mirrored. In case 3 ($B = B_y$) and 4 ($B = -B_y$) the path length of the electron before hitting the first dynode differes, depending on the polarisation of the magnetic field.

The transit time in case 1 and 2 are not expected to differ from each other and only very little from the parameters with no artificial field. In case 3 and 4 the situation is different. The path length and therefore the transit time of the electron decreases, when the electron is deflected towards the first dynode (case 4) and increases, when the electron is deflected away from the first dynode (case 3). This matches the observed transit time changes and position of the poles of the measurements.

Small changes in the magnetic field, the speed or emitting position of the electron, cause small variations on the position of the electron hitting the dynode and changes the path length to the dynode resulting in the TTS. Small path changes have far greater impact on case 4 compared to case 3. The more parallel the electron path is to the dynode, the greater are the path length changes for small variations in the direction of the electron. The TTS is therefore smaller for higher transit times, and higher for smaller transit times.

Magnetic field orientated parallel to the symmetry axis of the PMT

In cases 5 and 6 the field is orientated along the x-axis of the setup, parallel to the symmetry axis of the PMT, $B = B_x$ and $B = -B_x$. The photo electron gets accelerated towards the first dynode, following the symmetry axis of the PMT. In these cases the direction of the electron is parallel to the magnetic field, resulting in no acceleration by the Lorentz force and therefore no deviation of the PMT parameters from the case without magnetic field.

It can be expected that the deflection of the electron changes the number of electrons hitting each dynode. To explain the behaviour of the gain, a detailed analyses of the geometry of the dynode structure of the PMT is necessary, which exceeds the range of this thesis.

Order of the variations in transit time

A short qualitative analysis can be made, by calculating a very simplified deflection of an electron by a magnetic field of a strength of $B = 52.4\,\mu\mathrm{T}$. The simplifications include the following points:

- The electron gets emitted with a start velocity of $\vec{v} = 0$ from the centre of the cathode and travels in a straight line towards the first dynode, neglecting the curvature of the electron path due to the shape and position of the dynode.
- Due to the angle between the undeflected and new path of the electron being very small, the deflected electron path can be assumed to be parallel to the original path. This means, that the magnetic field can be approximated to be always perpendicular to the direction of the electron. The cross product of the Lorentz force $\vec{F} = q \cdot \vec{B} \times \vec{v}$ can therefore be approximated by $\vec{F} = |q \cdot B \cdot v|$, which is sufficiently accurate for the small changes in the direction of the electron induced by the Lorentz force.

- Between the cathode and first dynode is a potential difference of $U = 3 \cdot 1350/13 \approx 311\,\mathrm{V}$ over an approximated distance of $d = 40\,\mathrm{mm}$.
- The dynode is approximately flat over the small distances induced by the deflection, but can be seen as tilted by an angle α against the path of the electron depending on the electron hit position.

The flight time of the electron between the cathode and the dynode is described by [44]

$$\frac{\pi}{4}\sqrt{\frac{2m}{e \cdot U}} \cdot d \approx 6.01 \cdot 10^{-9}\,\mathrm{s} \tag{4.2}$$

where $e \approx 1.6 \cdot 10^{-19}\,\mathrm{C}$ is the electron charge and $m \approx 9.1 \cdot 10^{-31}\,\mathrm{kg}$ is the electron mass. The average velocity of the electron is calculated with $v = \frac{d}{t} \approx 6.66 \cdot 10^{6}\,\frac{\mathrm{m}}{\mathrm{s}}$ and the average resulting Lorentz force is $F = e \cdot v \cdot B \approx 5.5 \cdot 10^{-17}\,\mathrm{N}$. This force results in an average acceleration of $a = F/m \approx 6.1 \cdot 10^{13}\,\frac{\mathrm{m}}{\mathrm{s}^2}$. During its flight the electron is deflected by the Lorentz force over a distance of $s = \frac{1}{2}a \cdot t^2 \approx 1.1\,\mathrm{mm}$ perpendicular to its original movement direction.

This 1.1 mm leads to a deviation of the total traveling distances before reaching the dynode depending on the angle of the dynode towards the symmetry axis of the PMT illustrated in figure 4.16.

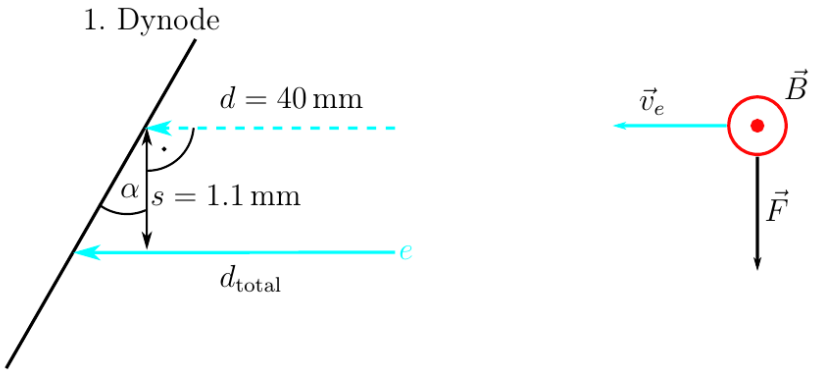

Figure 4.16: The magnetic field is orientated out of the plane and deflects an electron from its original path to the first dynode (dotted line). Here the dynode is tilted by $\alpha = 30°$. The electron gets deflected by 1.1 mm from its undeflected path resulting in a new path length of d_{total}.

If the angle of the dynode to the electron path without deflection is 90° or $\alpha = 0°$, the total distance covered by the electron roughly the same as without a field and the flight time should not change. This changes for different dynode angles and whether the dynode is orientated towards (case 3) or away from the deflected electron (case 4). A dynode with an angle of 30° orientated away from the electrons path results in $d_{\mathrm{total}} \approx 40.64\,\mathrm{mm}$ while the dynode orientated in the other direction results in $d_{\mathrm{total}} \approx 39.36\,\mathrm{mm}$. By applying d_{total} to equation 4.2 the new flight time can be calculated. This is shown for 30° and 60° in table 4.1

Table 4.1: Approximated path length and flight time changes depending on the angle of the dynodes tilt.

Dynode angle (°)	d_{total} (mm) case 3	d_{total} (mm) case 4	t (ns) case 3	t (ns) case 4
0 with no field	40	40	6.01	6.01
0	40	40	6.01	6.01
30	40.64	39.36	6.10	5.91
60	41.91	38.09	6.29	5.72

The flight length changes result in different flight times. These times agree with the assumptions of the discussion that depending on the bending direction of the dynode the transit time increases and decreases. The results of these simplified calculations agree with the previous quantitative discussion and the measurements. The travel time changes of the electron depending on the bending direction of the first dynode are of the same order of magnitude as the measured mean transit time changes of about 0.6 ns, illustrated in figure 4.5. Additionally varying the angle of the dynode shows, that small changes in the position have a higher impact on the TTS for higher dynode angles, matching the previous considerations.

5 Summary and outlook

The aim of this thesis was the construction of a setup for the generation of homogeneous, stable fields strong enough to match the field at the South Pole in arbitrary directions. The generated fields were used, to investigate the effect of magnetic fields on the Hamamatsu PMT R12199-02 installed in the mDOM, which is currently in testing at the University of Münster to be part of IceCube Upgrade.

As first step, the field of square Helmholtz coils was calculated and analysed regarding the size of the volume with less than 1 % inhomogeneity and the strength of the field. Furthermore, the heat production of copper wires of various radii for different currents was examined. The parameters used meeting the given requirements are listed in table 3.8.

The construction of the coils faced several difficulties and construction complications. Straightening copper wires with a radius of 1 mm turned out to be problematic as well as keeping a tight wire layout in the cavities of the frame. Additionally, scratches and fissures in the coating of the wires resulted in short circuits rendering the coils unusable. After applying additional precautions and improving the rolling process, the coils were sufficiently exact with no identifiable weak points or critical flaws. Automation was implemented for the hardware as far as possible, to minimise computation and measuring times and to allow easy access to any person using the coils in the future.

To characterise the magnetic field of the laboratory and the artificial magnetic field of the coils, as well as the used hardware, several tests were performed. The magnetometers were cross-calibrated and showed a similar magnetic field strength with deviations of $\approx 1\,\mu\mathrm{T}$.

The expected linear behaviour between the steering voltage of the power supplies and the B-field was checked, by increasing the current in each coil separately and measuring the strength of the magnetic field in the centre of the coils. While overall the field behaved as predicted, some aberration were visible for smaller orders of magnitude, smaller than $1\,\mu\mathrm{T}$ of the field, most likely having their origin in the hardware of the magnetometers.

The stability of the field over time was analysed. The measurements showed a small drift right after starting the coils, but this drift was within the resolution of the magnetometer and vanished after an hour.

To review the homogeneity of the magnetic field, the field was measured with and without artificial field for different positions in the cube. Even though the inhomogeneity increased closer to the centre as predicted by the theory, the measured inhomogeneity of the field was in the same order of magnitude and smaller than $\approx 1\%$ over a range of 20 cm from the centre.

First measurements on the influence of magnetic fields on the Hamamatsu R12199-02 of the mDOM were done. The measured signals were evaluated regarding their charge and mean transit time and plotted in corresponding histograms. The charge histogram was subsequently used to calculate the gain, while the transit time peak was investigated regarding its relative position (the transit time) and width (the transit time spread (TTS)).

To reproduce the previous measurements on the PMT done by Lukas Kuballa, his setup was transferred to the coil system. The PMT was placed horizontally in the cube centre with the first dynode bent upwards and a field with a vertical component of $(43.9 \pm 1.3)\,\mu\mathrm{T}$ and a horizontal component of $(18.4 \pm 0.7)\,\mu\mathrm{T}$ was generated. This field was rotated in 5° steps in the horizontal plane and the gain and TTS were measured.

While both, the measured TTS of Lukas Kuballa and the measurement done in this thesis showed a sinus-like behaviour, the gain measurement yielded different results. The relative deviation of the gain was comparably high but followed a sinus, similar to the TTS in the new measurements, not visible in in the previous measurements. These differences most likely have their origin in differences in the hardware and the applied high voltage. While in the previous work a total gain of 10^6 was used, a gain of 10^7 was used in the measurements in this thesis to increase the signal to noise ratio. While the maximum deviations from the mean were $\approx \pm 6\,\%$ for the TTS and $\approx \pm 3\,\%$ for the gain in his data, the new measurements yielded a slightly higher deviation of $\approx \pm 8\,\%$ for the TTS and a similar $\approx \pm 3\,\%$ for the gain.

Measurements on how gain and transit time behave for conditions similar to the real experiment at the South Pole (a field orientated in arbitrary directions with a strength of $54.7\,\mu\mathrm{T}$) were done, by orientating the field in 192 spherical coordinate steps in every direction.

The transit time has two clear poles when the magnetic field is perpendicular to the rotational axis of the PMT and the bending orientation of the first dynode and shows variations from $-0.62\,\mathrm{ns}$ to $0.54\,\mathrm{ns}$. The TTS ranges from $2.26\,\mathrm{ns}$ to $3.07\,\mathrm{ns}$ and behaves contrary to the transit time itself, rising with a decreasing transit time. The gain showed a similar dipole behaviour as the TTS and showed deviations of $-9\,\%$ to $5.2\,\%$ but less distinct and slightly shifted, compared to the dipole of the transit time. Due to the inhomogeneous electric field of the photocathode, the second, a factor 10 smaller, peak is visible after the first main peak of the transit time. While the height of the peak varied between $\approx 5.3\,\%$ and $9.7\,\%$ relative to the height of the main peak and the transit time ranged between $2\,\mathrm{ns}$ and $5.2\,\mathrm{ns}$, no distinct structures were visible. The position of the second peak relative to the first peak showed the already known dipole behaviour, falling between $2.9\,\mathrm{ns}$ and $4.6\,\mathrm{ns}$.

In conclusion, the setup is working up to the expectations and the first measurements were successfully completed.

Even though the setup is running smoothly, there are still parts that can be improved. The cables leading to the coils have to be switched whenever the field has to be re-polarised, because the power supplies are not able to generate negative currents. Additionally, the inhomogeneity of the background fields in the laboratory is quite high. A different laboratory with a more homogeneous field would be preferable as soon as the whole mDOM is going to be analysed. Lastly, the magnetometer showed erratic magnetic field changes, which could not be entirely explained but are neglectable compared to the uncertainty of the background field. In future measurements, a high precision magnetometer should be introduced into the setup.

While the general underlying concept and the order of magnitude were analysed and matched the measurements, a full simulation of the the influence of magnetic fields on PMT parameters would be excellent.

The shifting transit time and a higher TTS will negatively affect the time resolution,

which should be as high as possible for a successfully neutrino reconstruction of an excellent quality. Because no shielding is planned for the PMTs of the mDOM, the deviations of the PMT parameters can only be to be corrected numerically. The orientation PMTs of the mDOM inside of the ice of the South Pole will be known as well as the local field of each mDOM. The changes of the transit time regarding the field orientation open the possibility to develop a correction function to compensate for aberrations caused by the magnetic field. To implement such a function, the effect of the magnetic fields has to be precisely know. This thesis lies the foundation for such work and the constructed setup offers the ability to modulate the magnetic field of the Earth in any needed way necessary. As soon as the full mDOM is completed, the mDOM itself can be studied.

A Appendix

A.1 Code documentation

In the following sections the three programs used for operating the coil cube are documented.

A.1.1 B-FieldCharacterisation.py

This program offers various functions used to characterise the field of the coils.

Used packages:

- *time*
- *numpy*
- *sys*
- *Phidget22.Devices.Magnetometer*
- *matplotlib.pyplot*

Global variables:

- *numberofmags* = 1
  If two magnetometers are used *numberofmags* has to be set to "2".
- *Mag1*
  Instance of the first *Phidget* magnetometer.
- *Mag2*
  Instance of the second *Phidget* magnetometer.

Functions:

Initiate_Modules()
Description: Initialising the magnetometers and voltage channels.
Parameters:

- none

Returns:

- *e*: exception
  Catched errors while initialising.

Get_Field(*Mag*)
Description: Basic function to measure the magnetic field once and return the magnetic field in µT.
Parameters:

- Mag:
  Instance of the used magnetometer

Returns:

- *MagneticField*·100: numpy.array
  Magnetic field in μT.

Measure(*filename*)
Description: Function to measure, print out and write the current magnetic field to a file every second.
Parameters:
- *filename*: str
  Name of the .txt file the data is saved in.

Returns:
- none

Measure_Time(*filename,t*)
Description: Function to measure and write the current magnetic field to a file every 0.1 seconds for a set time interval.
Parameters:
- *filename*: str
  Name of the .txt file the data is saved in.
- *t*: int
  Total length of the measurement in s.

Returns:
- none

Measure_Steps(*filename*)
Description: Function to measure and write the current magnetic field to a file after each keyboard input.
Parameters:
- *filename*: str
  Name of the .txt file the data is saved in.

Returns:
- none

Measure_Steps_Average_With_Errors(*filename, average*)
Description: Function to measure and write the current magnetic field to a file after each keyboard input, while averaging over a given number of points and calculating the standard deviation.
Parameters:
- *filename*: str
  Name of the .txt file the data is saved in.
- *average*: int
  Number of points taken before calculating the average.

Returns:
- none

Simple_Plot(*filename, n, uncertainties=False*)
Description: Simple plot for quick tests.
Parameters:

- *filename*: str
  Name of the .txt file the data is saved in.
- n: int
  Column ($1 = B_x, 2 = B_y, 3 = B_z$) of the data chosen for the plot.
- *uncertainties = False*: bool
  "*True*" if the file contains uncertainties, which should be plotted.

Returns:

- none

Main()
Description: Main body of the measurements with examples.
Parameters:

- none

Returns:

- none

A.1.2 Calibration.py

Calibration routines for the Helmholtz coil cube. Each coil gets powered up independently while measuring the field in the centre of the coils. The resulting 9 data sets are then linearly fitted and the 9 functions used to calculate 3 functions for any magnetic fields depending on the steering voltages.

Used packages:

- *time*
- *numpy*
- *sys*
- *Phidget22.Devices.Magnetometer*
- *Phidget22.Devices.VoltageOutput*
- *Phidget22.Devices.VoltageRatioInput*
- *matplotlib.pyplot*
- *sympy*

Global variables:

- *Mag*
  Instance of the *Phidget* magnetometer
- *VOut0,VOut1,VOut2*
  Channels of the steering Voltage of the power supplies.
- *Temp*
  Instance of the *Phidget* temperature sensor.
- *mxx,mxy,mxz,myx,myy,myz,mzx,mzy,mzz,bx,by,bz*: float
  Variables of the linear calibration fit of the form $y = m \cdot x + b$. As example, mxy is the influence of the x coil on the y component of the field. bx is the offset $B_{0,x}$ of the x component of the field.

Functions:

Initiate_Modules()
Description: Initialising the magnetometers and voltage channels.
Parameters:
- none

Returns:
- *e*: exception
  Catched errors while initialising.

Close()
Description: Function to close all *Phidget* devices.
Parameters:
- none

Returns:
- none

Get_Temp_Celsius()
Description: Function to measure and return the temperature in °C.
Parameters:
- none

Returns:
- *temp_ celsius*: float
  Temperature in °C. 0 is returned when no sensor is used.

Get_Field(*Mag*)
Description: Basic function to measure the magnetic field once and return the magnetic field in µT.
Parameters:
- Mag:
  Instance of the used magnetometer

Returns:
- *MagneticField*·100: numpy.array
  Magnetic field in µT.

Get_Field_Average(a)
Description: Function to measure the average magnetic field in µT and return the mean average field and its standard deviation.
Parameters:
- *a*: int
  Number of points taken per measurement.

Returns:
- *B*: numpy.array
  Average magnetic field
- *sigma*: numpy.array
  1-sigma standard deviation of the field.

Get_Fields(*V, VOut, filename, a)*
Description: Function to increase the steering voltage of the given voltage steering channel

by 0.02 V and measure the average magnetic field in µT. Subsequently writing the data to a file.

- V: float
  Steering voltage value to be set to.

- *VOut*:
  Identification of the given steering voltage channel.

- *filename*: str
  Name of the .txt file the data is saved in.
- a: int
  Number of points taken per measurement.

Returns:

- none

fit(*name, i*)
Description: Function to apply a linear fit $y = m \cdot x + b$ on the data gathered by GetFields(), which returns the fit values of "m" and "b". Additionally, a basic plot is done.
Parameters:

- *name*: str
  File name of the data to be fitted.
- i: int
  Column ($1 = B_x, 2 = B_y, 3 = B_z$) of the data chosen for the fit.

Returns:

- m: float
  m of the linear fit $y = m \cdot x + b$.

- b: float
  b of the linear fit $y = m \cdot x + b$.

Get_Functions(*namex,namey,namez*)
Description: Function to apply the fit function to all components of the field.
Parameters:

- *namex*: str
  Name of the first input file for the fit.
- *namey*: str
  Name of the second input file for the fit.
- *namez*: str
  Name of the third input file for the fit.

Returns:

- none

Save_As_Arrays()
Description: Function to save the fit parameters in "Data\Calibration" in the corresponding arrays "mx", "my" and "mz"
Parameters:

- none

Returns:
- none

Solve_Functions(*filename*)
Description: Function to combine the 9 fit functions to a 3 function system and reshape the system regarding the B-field components. The earlier gets written in a file called "filename" + "_equations.txt" the later in "filename + "_result.txt".
Parameters:
- *filename*: str
  Name of the .txt file the data is saved in.

Returns:
- none

main()
Description: Main body of the measurements with examples.
Parameters:
- none

Returns:
- none

A.1.3 B-FieldMeasurement.py

Collection of functions to set and adjust the generated magnetic field. First the cables are checked, whether they have to be switched for a given starting field. Afterwards, the functions systems of the magnetic fields depending on the steering voltages are calculated from the calibration file. Subsequently new fields can get set and are adjusted until the deviation from the measured field to the desired field is less than 0.5 µT

Used packages:
- *time*
- *numpy*
- *sys*
- *Phidget22.Devices.Magnetometer*
- *Phidget22.Devices.VoltageOutput*
- *Phidget22.Devices.VoltageRatioInput*
- *matplotlib.pyplot*
- *scipy*
- *pylab*
- *sympy*
- *datetime*

Global variables:
- *Mag*
  Instance of the *Phidget* magnetometer
- *VOut0, VOut1, VOut2*
  Channels of the steering voltage of the power supplies.

- *Temp*
  Instance of the *Phidget* temperature sensor.
- $mxx, mxy, mxz, myx, myy, myz, mzx, mzy, mzz, bx, by, bz$: float
  variables of the calibration fit.

Functions:

Initiate_Modules()
Description: Initialising the magnetometers and voltage channels.
Parameters:
- none

Returns:
- *e*: exception
  Catched errors while initialising.

Close()
Description: Function to close all *Phidget* devices.
Parameters:
- none

Returns:
- none

Get_Temp_Celsius()
Description: Function to measure and return the temperature in °C.
Parameters:
- none

Returns:
- *temp_ celsius*: float
  Temperature in °C. 0 is returned when no sensor is used.

Get_Field(*Mag*)
Description: Basic function to measure the magnetic field once and return the magnetic field in µT.
Parameters:
- Mag:
  Instance of the used magnetometer

Returns:
- *MagneticField*·100: numpy.array
  Magnetic field in µT.

Get_Field_Average(*a*)
Description: Function to measure the average magnetic field in µT and return the mean average field and its standard deviation.
Parameters:
- *a*: int
  Number of points taken per measurement.

Returns:

- *B*: numpy.array
  Average magnetic field
- *sigma*: numpy.array
  1-sigma standard deviation of the field.

Solve_Functions()
Description: Function to combine the 9 fit functions to a 3 function system and reshape the system regarding the B-field components. The earlier gets written in a file called "filename" + "_equations.txt" the later in "filename" + "_result.txt".
Parameters:
- none

Returns:
- none

Compute_V(*B_s*)
Description: Function to calculate the necessary voltage by using the calibration functions to generate any magnetic field and update *V_x, V_y, V_z* accordingly.
Parameters:
- *B_s*: numpy.array
  Desired magnetic field.

Returns:
- none

Adjust_Voltage(*B_s, B*)
Description: Function to eliminate possible discrepancys after the setting of the calculated field using the calibrations. The effective difference between the desired field and the current are used to calculate and update the value of the steering voltages *V_x, V_y, V_z*.
Parameters:
- *B_s*: numpy.array
  Desired magnetic field.
- *B*: numpy.array
  Current magnetic field.

Returns:
- none

Adjust_Voltage2(*B_s, B, B_0, p*)
Description: Alternative function for the adjustment of the field. The ratio between the desired and current field are used to calculate and update the value of the steering voltages *V_x, V_y, V_z* for one given coil.
Parameters:
- *B_s*: numpy.array
  Desired magnetic field.
- *B*: numpy.array
  Current magnetic field.
- *B_0*: numpy.array
  Magnetic field at the start of the measurement.

- *p*: str
  Identification of the coil in question: "x","y","z".

Returns:

- none

Set_Magnetic_Field(*V, VOut*)

Description: Function to set the steering voltage of the given channel to certain value, as long as that value does not exceed a critical value of 1.65 V.

- *V*: float
  Steering voltage value to be set to.

- *VOut*:
  Identification of the given steering voltage channel.

Returns:

- none

Cables(*B_s, B_0*)

Description: Function to check whether all cables are correctly connected for the first desired magnetic field.

Parameters:

- *B_s*: numpy.array
  Desired magnetic field.
- *B_0*: numpy.array
  Magnetic field at the start of the measurement.

Returns:

- none

New_Field(*B_s, condx, condy, condz, CritTemp=20*)

Description: Function to set a new field. "*Condx*", "*condy*" and "*condz*" are either "True" or "False" whether the cables were already switched after the first measurement or not. The program terminates when a temperature increase of 20 °C is exceeded. First all cables are controlled, then the voltage turned up according to the calibration. Subsequently the field gets adjusted, while checking if cables need to be switched. This process gets repeated until the difference between the desired magnetic field and the field measured by the magnetic field sensor is smaller than 0.5 µT.

Parameters:

- *B_s*: numpy.array
  Desired magnetic field.
- *condx*: bool
  Cable condition for the "x"-coil, "True" after start, "False" when the cables were switched.
- *condy*: bool
  Cable condition for the "*y*"-coil, "True" after start, "False" when the cables were switched.
- *condz*: bool
  Cable condition for the "*z*"-coil, "True" after start, "False" when the cables were switched.

- *CritTemp=20*: float
  Critical temperature rise accepted before stopping the measurement, 20 as default.

Returns:

- none

Main()

Description: Main body of the measurements with examples.

Parameters:

- none

Returns:

- none

A.2 Results of the second magnetometer

Figures A.1 to A.3 show the calibration plots of the second magnetometer, used as reference and cross checking device. The data was generated, by turning up every coil subsequently and measuring the field in the centre. For further explanation, see section 3.3.1.

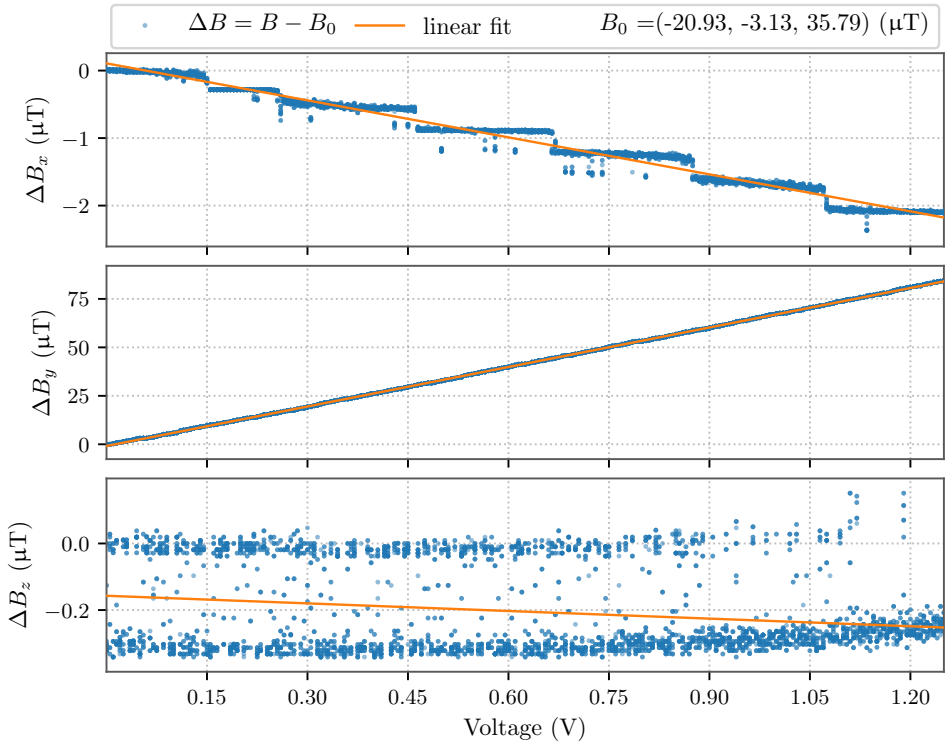

Figure A.1: Powering up the x-coil while measuring the field in the centre of the cube, with the second magnetometer rotated by 90° in the y-x-plane.

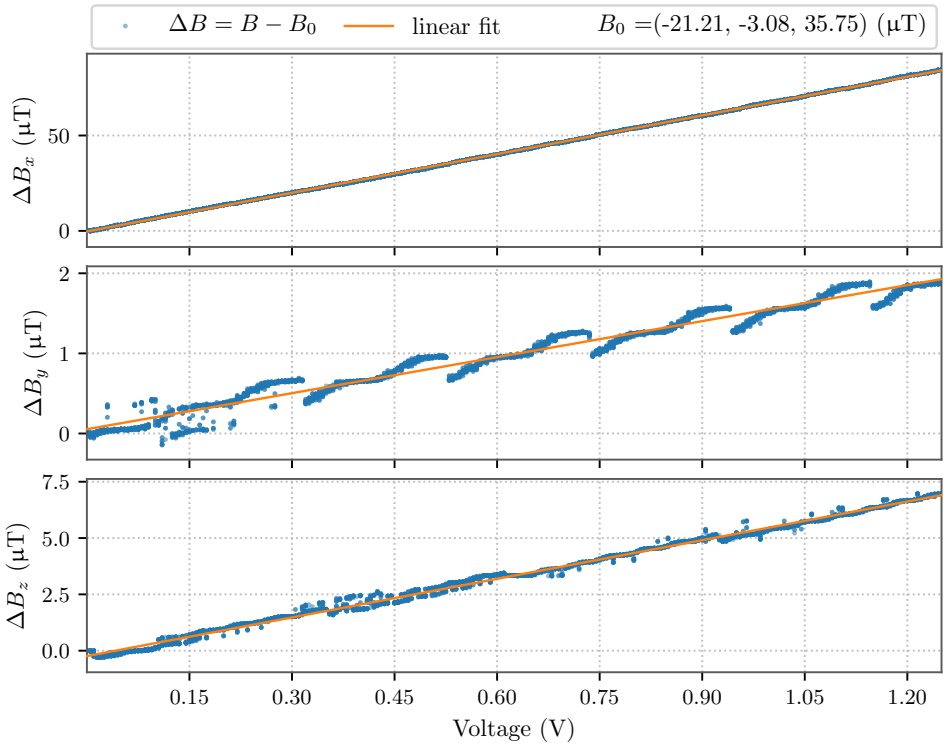

Figure A.2: Powering up the y-coil while measuring the field in the centre of the cube, with the second magnetometer rotated by 90° in the y-x-plane.

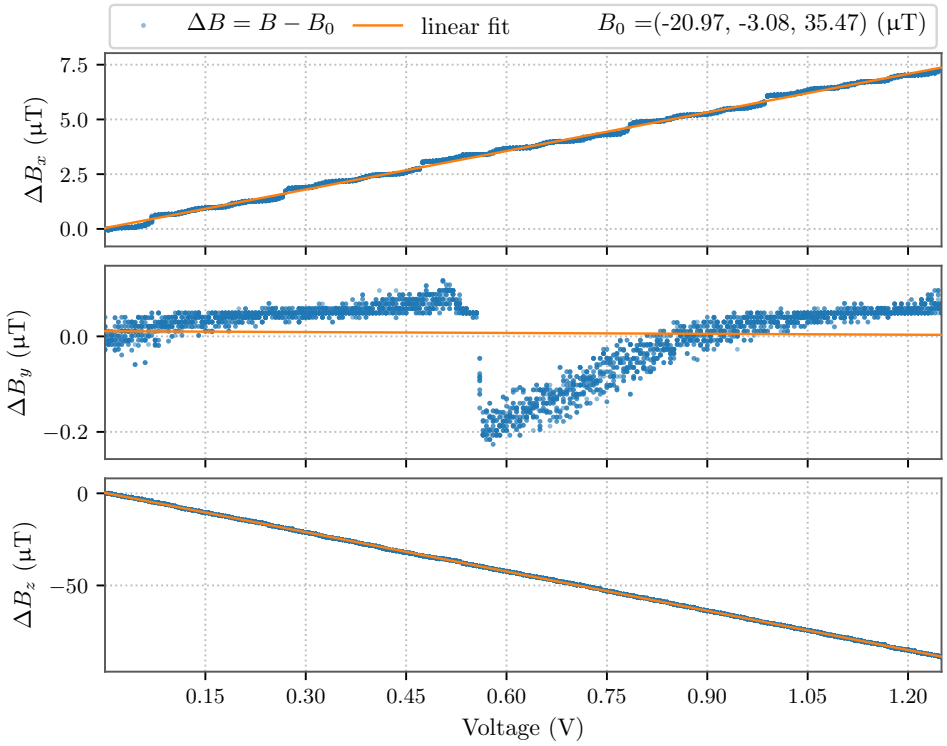

Figure A.3: Powering up the z-coil while measuring the field in the centre of the cube, with the second magnetometer rotated by 90° in the y-x-plane.

Figures A.5 to A.6 show the stability tests of the magnetic field measured by the second magnetometer used as reference and cross checking device. The data was generated by measuring the field at the centre of the coils over 10 minutes, with and without artificial fields. For further explanation see section 3.3.1.

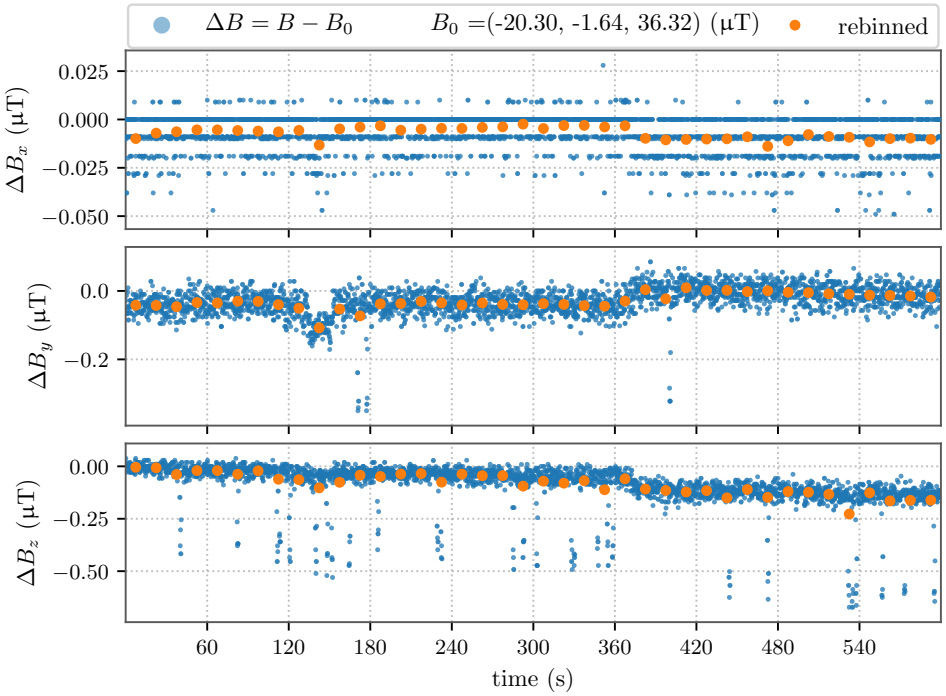

Figure A.4: Behaviour of the background magnetic field in the laboratory over 10 minutes, measured with the second magnetometer.

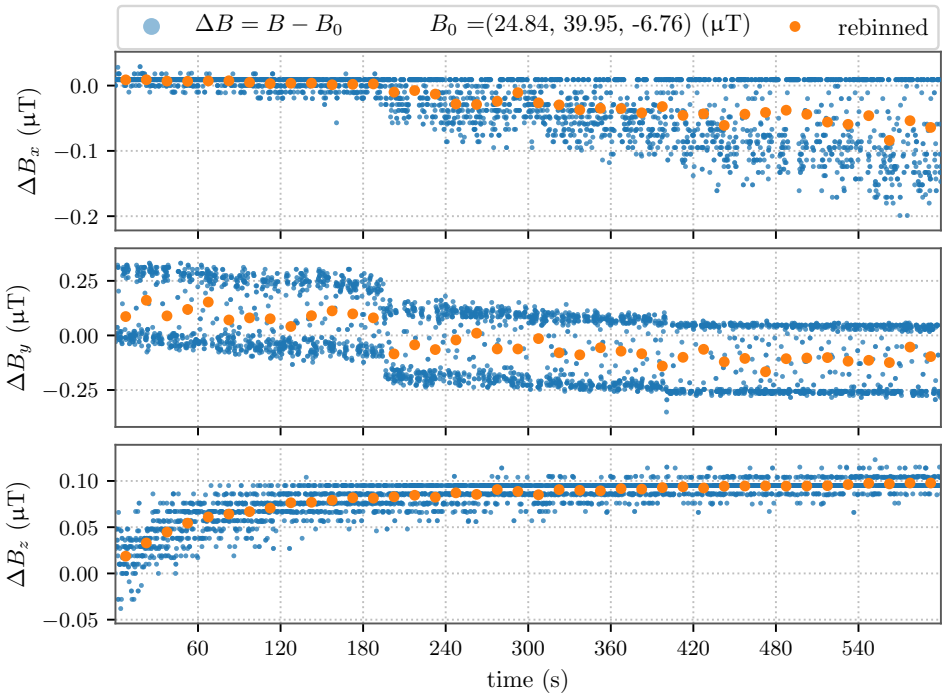

Figure A.5: Behaviour of the total magnetic field, measured with the second magnetometer.

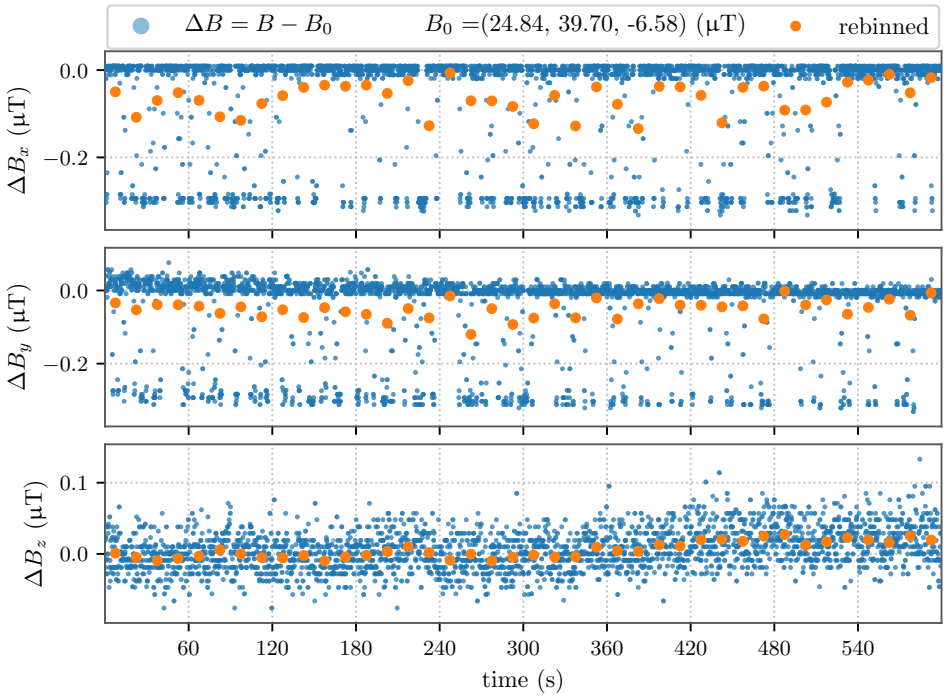

Figure A.6: Behaviour of the total magnetic field after a waiting time of ≈ 30 minutes, measured with the second magnetometer.

Bibliography

[1] T. K. Gaisser, R. Engel, E. Resconi, Cosmic Rays and Particle Physics, Cambridge University Press, 2016.

[2] J. Blümer, J. Engler, Atmospheric cosmic ray detectors: Datasheet from landolt-börnstein - Group I elementary particles, nuclei and atoms · volume 21b2: Detectors for particles and radiation. part 2: Systems and applications", springer-Verlag Berlin Heidelberg, 2011. doi:10.1007/978-3-642-14142-3_2.
URL:https://materials.springer.com/lb/docs/sm_lbs_978-3-642-14142-3_2

[3] The pierre auger cosmic ray observatory, Nuclear Instruments and Methods in Physics Research Section A: Accelerators, Spectrometers, Detectors and Associated Equipment 798 (2015) 172 – 213. doi:https://doi.org/10.1016/j.nima.2015.06.058.
URL:http://www.sciencedirect.com/science/article/pii/S0168900215008086

[4] Multi-messenger astrophysics, available at https://astro.desy.de/theory/multi_messenger_astrophysics/index_eng.html; last called on 10.01.2020.

[5] A. Franceschini, G. Rodighiero, The extragalactic background light revisited and the cosmic photon-photon opacity, Astron. Astrophys. 603 (2017). arXiv:1705.10256, doi:10.1051/0004-6361/201629684.

[6] N. MissMJ, et al., available at https://commons.wikimedia.org/wiki/File:Standard_Model_of_Elementary_Particles_modified_version.svg; last called on 10.01.2020. (2014).

[7] Christian Spiering, Towards high-energy neutrino astronomy, The European Physical Journal H 37 (3) (2012) 515–565. doi:https://doi.org/10.1140/epjh/e2012-30014-2.

[8] K. Olive, Review of particle physics, Chinese Physics C 40 (10) (Oct 2016). doi:10.1088/1674-1137/40/10/100001.

[9] J. A. Formaggio, G. P. Zeller, From ev to eev: Neutrino cross sections across energy scales, Rev. Mod. Phys. 84 (2012) 1307–1341. doi:10.1103/RevModPhys.84.1307.
URL:https://link.aps.org/doi/10.1103/RevModPhys.84.1307

[10] L. Classen, The mDOM - a multi-PMT digital optical module for the IceCube-Gen2 neutrino telescope, PhD Thesis, Friedrich-Alexander-Universität Erlangen-Nürnberg (2017).
URL:https://www.uni-muenster.de/imperia/md/content/physik_kp/agkappes/abschlussarbeiten/doktorarbeiten/1702-phd_lclassen.pdf

[11] M. Unland, Studies on dark rates induced by radioactive decays of the multi-PMT digital optical module for future IceCube extensions, Master Thesis, Westfälische Wilhelms-Universität Münster (2017).
URL:https://www.uni-muenster.de/imperia/md/content/physik_kp/agkappes/abschlussarbeiten/masterarbeiten/1712-ma_munland.pdf

[12] J. V. Jelley, Cerenkov radiation and its applications, British Journal of Applied Physics 6 (7) (1955) 227–232. doi:10.1088/0508-3443/6/7/301.

[13] I. Frank, I. Tamm, Coherent visible radiation of fast electrons passing through matter, in: Selected Papers, Springer Berlin Heidelberg, 1991, pp. 29–35. doi:10.1007/978-3-642-74626-0_2.

[14] I. M. Alden L. Coke, The Detection of Neutrinos in IceCube, available at https://masterclass.icecube.wisc.edu/en/learn/detecting-neutrinos; last called on 10.01.2020.

[15] M. G. Aartsen, et al., The IceCube Neutrino Observatory: Instrumentation and Online Systems, JINST 12 (03) (2017) P03012. arXiv:1612.05093, doi:10.1088/1748-0221/12/03/P03012.

[16] R. Abbasi, Y. Abdou, T. Abu-Zayyad, M. Ackermann, J. Adams, J. Aguilar, M. Ahlers, M. Allen, D. Altmann, K. Andeen, et al., The design and performance of icecube deepcore, Astroparticle Physics 35 (10) (2012) 615–624. doi:10.1016/j.astropartphys.2012.01.004.
URL:http://dx.doi.org/10.1016/j.astropartphys.2012.01.004

[17] A. Ishihara, The icecube upgrade – design and science goals (2019). arXiv:arxiv:1908.09441.

[18] M. G. Aartsen, et al., Icecube-gen2: A vision for the future of neutrino astronomy in antarctica, arXiv:1412.5106 (2014). arXiv:1412.5106.

[19] Mumetal, Mu Metal specifications, available at http://mumetal.co.uk/?p=100#more-100; last called on 10.01.2020. (2009).

[20] T. Wright, A. Wright, The Photomultiplier Handbook, Oxford University Press, 2017.

[21] M. Suyama, K. Nakamura, Recent Progress of Photocathodes for PMTs, Proceedings of science, 2009.
URL:https://pos.sissa.it/090/013/pdf

[22] S.-O. Flyckt, C. Marmonier, Photomultiplier tubes - principicles and applications, Photonis, 2002.

[23] E. H. Bellamy, et al., Absolute calibration and monitoring of a spectrometric channel using a photomultiplier, Nuclear Instruments and Methods in Physics Research A 339 (1994) 468–476. doi:10.1016/0168-9002(94)90183-X.

[24] U. of Waikato, Earth's magnetic field , available at https://www.sciencelearn.org.nz/images/1820-earth-s-magnetic-field; last called on 10.01.2020. (2017).

[25] J. Matzka, A. Chulliat, M. Mandea, C. C. Finlay, E. Qamili, Geomagnetic observations for main field studies: From ground to space, Space Science Reviews 155 (1) (2010) 29–64. doi:10.1007/s11214-010-9693-4.
URL:https://doi.org/10.1007/s11214-010-9693-4

[26] P. H. Roberts, G. A. Glatzmaier, Geodynamo theory and simulations, Rev. Mod. Phys. 72 (2000) 1081–1123. doi:10.1103/RevModPhys.72.1081.
URL:https://link.aps.org/doi/10.1103/RevModPhys.72.1081

[27] NMR down to Earth, Nature 439 (7078) (2006). doi:https://doi.org/10.1038/439799a.

[28] B. S. Singer, et al., Synchronizing volcanic, sedimentary, and ice core records of earth's last magnetic polarity reversal, Science Advances 5 no. 8 (Aug 2019).

[29] N. N. G. D. Center, South Magnetic Pole Movement Based on Magnetic Field Models 1590 - 2010, available at https://www.ngdc.noaa.gov/geomag/maps/SouthPole1590_2010.pdf; last called on 10.01.2020. (2005).

[30] N. C. for Environmental Information (NCEI), Magnetic Field Estimated Values More

information, available at https://www.ngdc.noaa.gov/geomag/calculators/magcalc.shtml#igrfwmm; last called on 10.01.2020.

[31] B. G. Survey, The earth's magnetic field: An overview, available at http://www.geomag.bgs.ac.uk/education/earthmag.html; last called on 10.01.2020. (2015).

[32] R. Nave, Helmholtz Coils, available at http://hyperphysics.phy-astr.gsu.edu/hbase/magnetic/helmholtz.html; last called on 10.01.2020.

[33] A. Restrepo, E. Franco, C. Pinedo, Study and analysis of magnetic field homogeneity of square and circular helmholtz coil pairs: A taylor series approximation, Proceedings of the 6th Andean Region International Conference, Andescon 2012 (Nov 2012). doi:10.1109/Andescon.2012.27.

[34] Hamamatsu, Large photocathode area photomultiplier tubes, available at https://www.hamamatsu.com/resources/pdf/etd/LARGE_AREA_PMT_TPMH1376E.pdf; last called on 10.01.2020.

[35] S. Aiello, E. Leonora, A. Grimaldi, G. Leotta, D. Lo Presti, N. Randazzo, D. Sciliberto, V. Sipala, Influence of the earth's magnetic field on large area photomultipliers, IEEE Transactions on Nuclear Science 59 (4) (2012) 1259–1267. doi:10.1109/TNS.2012.2189245.

[36] L. Kuballa, Untersuchungen zur Ausgabelinearität von Photomultipliern des Typs Hamamatsu R12199-02 sowie des Einflusses des Erdmagnetfelds auf die Photomultiplier-Eigenschaften, Bachelor Thesis, Westfälische Wilhelms-Universität Münster (2017).
URL:https://www.uni-muenster.de/imperia/md/content/physik_kp/agkappes/abschlussarbeiten/bachelorarbeiten/1710-ba_lkuballa.pdf

[37] E. Huber, M. Urban, Helmholtzspulen zur Kalibrierung von Magnetfeldsensoren, Tech. rep., 90; LK 01; Wissenschaftliche Berichte, FZKA-5643 (November 95) (1995). doi:10.5445/IR/270038307.

[38] Kanya, Gesamtkatalog, available at https://www.kanya.com/fileadmin/kanya/downloads/de/Gesamtkatalog_KANYA_CH_DE_eVersion_.pdf; last called on 10.01.2020.

[39] Phidgets, Precision Temperature Sensor, available at https://www.phidgets.com/?tier=3&catid=14&pcid=12&prodid=95; last called on 10.01.2020. (2007).

[40] Phidgets, PhidgetSpatial 3/3/3 Basic, available at https://www.phidgets.com/?tier=3&catid=10&pcid=8&prodid=1025; last called on 10.01.2020. (2018).

[41] Phidgets, 1042 User Guide, available at https://www.phidgets.com/docs/1042_User_Guide#Magnetometer; last called on 10.01.2020. (2019).

[42] Delta Elektronika, Sm 700 - series, available at https://www.delta-elektronika.nl/upload/MAN_SM700.pdf; last called on 10.01.2020. (2014).

[43] F. Kaether, C. Langbrandtner, Transit time and charge correlations of single photoelectron events in r7081 photomultiplier tubes, Journal of Instrumentation 7 (09) (2012) P09002–P09002. doi:10.1088/1748-0221/7/09/p09002.

[44] P. B. Coates, The origins of afterpulses in photomultipliers, Journal of Physics D: Applied Physics 6 (10) (1973) 1159–1166. doi:10.1088/0022-3727/6/10/301.
URL:https://doi.org/10.1088%2F0022-3727%2F6%2F10%2F301

Acknowledgements

Ich danke:

Prof. Dr. Alexander Kappes für die Möglichkeit meine Arbeit in seiner, mir ans Herz gewachsenen Arbeitsgruppe zu schreiben und meinen Teil zum IceCube und zur weiteren Erforschung der Neutrinoastronomie beizutragen,

Dr. Volker Hannen für die Bereitschaft sich als Zweitkorrektor durch meine Arbeit zu kämpfen,

Lew Classen und Antonio Unland Elorrieta für reichlich Unterstützung, wann immer ich verzweifelt war, und dem Korrekturlesen meiner Arbeit,

der ganzen Arbeitsgruppe von Prof. Kappes für die Beantwortung von Unmengen von Fragen, schönen Abenden und einer entspannten Arbeitsatmosphäre,

Hans-Werner Ortjohann für die Hilfe beim Umsetzten meiner Konstruktion,

der feinmechanischen Werkstatt und der Elektronikwerkstatt für ihre Unterstützung,

Phillip Brand und Tabea Eder, die noch etliche Fehler gefunden haben,

Markus Dittmer für die Hilfe bei den, gefühlt endlos vielen Wicklungen der Spulen,

meinem Vater Peer Ueberholz, der die schwere Aufgabe hatte, meine Arbeit als Erster zu lesen,

meiner Schwester Lea Ueberholz, die bestimmt noch 200 Kommas setzten musste,

und meiner Mutter Beate Ueberholz für ihre vielen Hilfen, um mir im Stress der Masterarbeitsendzeit alles andere möglichst leicht zu machen.